Design Methodology for an Inflatable Membrane Aerofoil Using Numerical Shape Optimisation

by

Bradley Bezuidenhout

Thesis presented in partial fulfilment of the requirements for the degree of Master of Engineering (Mechanical) in the Faculty of Engineering at Stellenbosch University

Supervisor: Prof. G. Venter
Co-supervisor: Dr. M.P. Venter

March 2020

Declaration

By submitting this thesis electronically, I declare that the entirety of the work contained therein is my own, original work, that I am the sole author thereof (save to the extent explicitly otherwise stated), that reproduction and publication thereof by Stellenbosch University will not infringe any third party rights and that I have not previously in its entirety or in part submitted it for obtaining any qualification.

Date: .....

Abstract

Design Methodology for an Inflatable Membrane Aerofoil Using Numerical Shape Optimisation

B. Bezuidenhout

Department of Mechanical and Mechatronic Engineering,
University of Stellenbosch,
Private Bag X1, Matieland 7602, South Africa.

Thesis: MEng (Mech)

March 2020

The use of inflatable wings for unmanned aerial vehicles over their fixed-winged counterparts has many advantages such as the wing's ability to be folded up when deflated, this saves storage space. However, there are challenges associated with predicting the profile of the inflatable wing, which makes achieving a desirable aerofoil profile non-trivial. This research aimed to formulate a design methodology which would determine the uninflated geometry for an inflatable aerofoil profile, accurately fitting that of a target, prescribed aerofoil profile. The uninflated geometry can then be used to construct a physical model. The methodology involved performing numerical shape optimisation on finite element models. Once the methodology had been established, its robustness was tested by utilising numerical models with differing numbers of inflation cavities, altering the thickness of the target aerofoil profile as well as increasing its complexity. For each case, the methodology successfully satisfied its aim, producing accurate fits between the inflated numerical model and the target aerofoil profile. When fitting a fifteen cavity numerical model to a NACA 0030 aerofoil, an R^2 fit of 0.990 was achieved. When validated, the inflated shape of the numerical model proved to predict that of its corresponding physical model accurately. For an eight cavity model, the fit between the physical and numerical model produced an R^2 value of 0.988. Future work should focus on a more comprehensive material model that will allow for a larger load-bearing capacity of the inflated structure.

Uittreksel

Ontwerpmetodologie vir 'n Opblaasbare Membraanlugvlerkprofiel met Gebruik van Numeriese Vormoptimalisering

B. Bezuidenhout

Departement Meganiese en Megatroniese Ingenieurswese,
Universiteit van Stellenbosch,
Privaatsak X1, Matieland 7602, Suid Afrika.

Tesis: MIng (Meg)

March 2020

Die gebruik van opblaasvlerke vir onbemande lugvaartuie bo-oor die regstreeks gevleuelde weergawes het veelvulgide voordele. Daar is vele kompleksiteit in akkurate profiel voorspelling van opblaasvlerke, wat veroorsaak dat die bereiking van 'n gewenste lugvliefprofiel ontriviaal is. Die doel van die navorsing is gemik om die formulering van 'n ontwerpmetodologie wat die afgeblaasde meetkunde van 'n opblaasbare-aëroolieprofiel sou bepaal. Die afgeblaasde meetkunde kan dan gebruik word om 'n fisiese model te konstrueer. Die betrokke metodologie maak gebruik van numeriese vorm optimalisering op eind element modelle. Nadat die metodologie vasgestel is, was die robuustheid daarvan getoets deur die gebruik van numeriesemodelle van verskeie kompleksiteite, deur die dikte van die teiken lugvliegprofiel te verander en die kompleksiteit te verhoog. Vir elke getoetsde geval, het die metodologie sy doelwit bereik deur 'n akkurate pas tussen die opgeblaasde numeriesemodel en die teiken aëroolieprofiel. By die montering van 'n numeriese model van die vyftien holtes op 'n NACA 0030 aërool, word die R^2 pas van 0.990 behaal. Na validasie, het die opgeblaasde vorm van die numeriesemodel met akkuraatheid die vorm van die fisiesemodel bepaal. Vir 'n model met agt holtes is die pas tussen die fisiese en numeriese model geproduseer teen R^2 waarde van 0.988. Toekomstige navorsing moet gebruik maak van 'n meer ingewikkelde model, wat sal toelaat vir 'n beter draëvermoë van die opgeblaasde struktuur.

Acknowledgements

I would like to express my sincere gratitude to Professor Gerhard Venter for his experience and knowledge while under his supervision throughout the past few years. Doctor Martin Venter for his accessibility and expertise. Doctor David Ellis for his willingness to unconditionally provide assistance. My friends for moulding me into the person I am today. Tamaryn Asbury for providing balance in my life and my family for their constant and unwavering support.

Contents

List of Figures

List of Tables

Chapter 1

Introduction

1.1 Background

The concept of inflatable wings entails applying an internal pressure to a membrane to stiffen the structure and enables it to support a load during flight. An instance of an inflatable-winged plane can be seen as far back as the 1950s with the Goodyear Model GA-468 Inflatoplane, shown in Figure 1.1. The Inflatoplane, with a wingspan of 6.7 m, was developed by the military as a rescue plane. It could be dropped behind enemy lines to rescue downed pilots (Brown *et al.*, 2001).

Figure 1.1: The Goodyear Model GA-468 Inflatoplane in flight (Cleveland-Magazine, 2015)

More recently, the focus for inflatable wings has shifted to unmanned aerial vehicles (UAVs), such as the I2000. The I2000 was a UAV with a wingspan of 1.5 m that was created and flight-tested by researchers at NASA (Murray *et al.*, 2002). The skeleton of the wing was made of inflatable tubes, surrounded by crushable foam to provide the aerofoil profile. The wings were able to go from deflated to fully inflated in 700 ms which was tested in an air launch sequence, as seen in Figure 1.2.

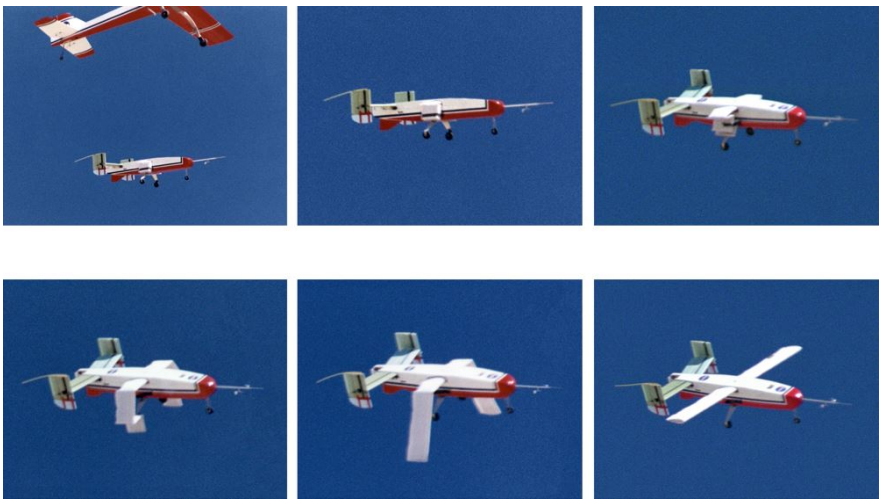

Figure 1.2: The air launch sequence and wing inflation for the I2000 UAV (Murray *et al.*, 2002)

The air-launch sequence of the I2000 showcases one of the many advantages of inflatable wings, with it having the ability to be folded up when deflated and then rapidly inflated. This allows space to be saved when transporting the plane as the space is not taken up by the wings. The inflatable wings are also more impact-resistant compared to fixed wings. For example, if the wing were to hit a tree it would be able to deform upon impact and then return to its original position. This was verified with impact tests performed by Cadogan *et al.* (2006). If the inflatable wing was punctured during the impact it could then be replaced at a reduced cost compared to a fixed-wing (Simpson, 2008).

Another advantage of inflatable wings is for the potential of the aircraft to be lighter than a fixed-winged aircraft. This bearing in mind the different inflation mechanism configurations. However, this advantage comes at a reduced load-bearing capacity of the wing. These advantages have enabled inflatable-winged UAVs to be used in aerospace applications where minimising weight and storage space is a key factor. They also have the potential to be used in agricultural applications for flying over fields, to gather data on the condition of the crops. The UAV can be landed in areas where there is no clear landing strip and there is a probability of it crashing into a bush or tree.

In the past, authors have explored the possibility of altering inflatable wing's shape during flight as a means of in-flight directional control. A paper by Cadogan *et al.* (2004) explored multiple wing shape altering methods ranging from mechanical actuation to pressure controlled actuation. The pressure controlled actuation boasts great potential in its ability to actuate the wing without the need for a mechanical actuator that, if placed on the wing surface, could hinder the aerodynamic performance. This is therefore an additional

potential advantage if correctly incorporated.

There are, however, difficulties associated with inflatables, one of them being that once an inflation pressure is applied to the membrane, the membrane deforms. The amount of deformation the membrane undergoes is unknown due to complexities associated with inflated membranes. This makes accurately predicting the inflated shape of an inflatable wing non-trivial. Achieving an aerofoil profile that accurately fits that of a target aerofoil profile is important, as deviations from the intended profile could alter its intended aerodynamic performance.

1.2 Aim and Objectives

The work proposed in this research aims to formulate a design methodology to determine the uninflated geometry for an inflatable aerofoil profile, accurately fitting that of a prescribed target aerofoil profile. This will be done through the use of numerical shape optimisation where a numerical model will be used to simulate the physical model in terms of its inflated shape. The project objectives are defined as follows:

1. Formulate a finite element (FE) model of single cavity inflatable bags and simulate the inflated shapes.
2. Validate the inflated shapes of the single cavity inflatable bag FE models through physical tests.
3. Increase the complexity of the FE models and perform shape optimisation on them.
4. Validate the inflated shape of the more complex FE models through physical tests.
5. Test the robustness of the shape optimization.
6. Build confidence in the FE model through stiffness validation.

1.3 Project Scope

It is important to note that this research focuses on the design methodology of fitting the inflated shape of an inflatable wing to a prescribed aerofoil shape, and not finding the optimal inflatable wing design. Therefore, certain aspects of the inflatable wing were omitted from the scope of the research, these consist of:

- A detailed study on an ideal membrane material to be used, instead the material used was chosen due its availability and its benefits in the design process, such as the constructibility of the models.
- Aerodynamic testing, however, aerodynamic performance aspects of inflatable wings from previous literature were considered.
- Choosing the optimal wing dimensions, as the methodology focuses on fitting the model to a target aerofoil profile. Therefore, the wing dimensions specific to each case can be prescribed by the designer.

Chapter 2

Literature Review

2.1 Inflatable Membrane Structures

Air-inflated structures consisting of air beams, where the pressurised space is not occupied, have been used in the past for many different engineering applications. One of these applications is using multiple inflatable beams connected to one another in order to form an aerofoil shape (Johansen, 2011; Rowe, 2007; Santhanakrishnan and Jacob, 2005). Gaining an understanding of simple inflatable beams is paramount, as they make up the foundation of inflatable wings.

Inflatable beams are membranes that, by themselves, have no stiffness. However, when an internal pressure is applied to the membrane, it becomes pre-tensioned and is stiffened. The stiffness of the beam is dependant on three factors: the internal pressure, the dimensions of the beam and the membrane material properties. The classic equations for hoop and longitudinal stresses acting on the walls of a cylindrical thin-walled pressure vessel can be used to determine the pre-tensioned state of the bag. The hoop stress equation can be seen in Equation 2.1:

$$\sigma = \frac{Pr}{t}, \tag{2.1}$$

where σ is the hoop stress, P is the internal pressure, t is the membrane thickness and r is the radius of the wall. The longitudinal stress occurring under the same conditions would be half the hoop stress's value (Wang and Li, 2017).

Membranes are generally very thin and due to their small thickness they have very little to no bending stiffness. Therefore, when a compressive stress is present in the membrane, it is diminished through a local instability in the

form of out-of-plane buckling. This local buckling is referred to as wrinkling. These wrinkles lie perpendicular to the applied compressive stress (Bletzinger, 2008).

An FE model of a 126 mm diameter and 1.32 m long beam under a three-point bending load was created by Barsotti and Ligaro (2011). The contact points were simply supported at the ends by constraining a single node at the corners of the ends of the bag. The deformed state of the symmetric FE model can be seen in Figure 2.1. The elements experiencing a compressive stress are shown in red, thus hinting at where the wrinkles would occur.

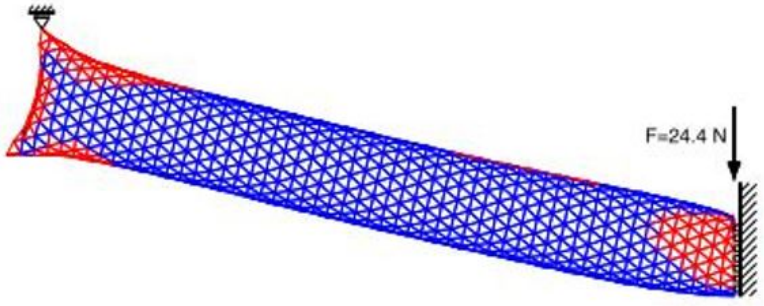

Figure 2.1: Elements in an FE model during a three-point bending test in a wrinkled state, shown in red (Barsotti and Ligaro, 2011)

Other examples of inflatable beams being modelled through analytical or FE models were published by Veldman (2005), Zhu *et al.* (2008) and Thomas *et al.* (2016). The first two studies performed cantilever tests on their models, whereas the third study tested three different test configurations for three-point bending tests. All of these models were each validated through physical testing with the operating pressures above 100 kPa.The tests were carried out by applying a load to the beam and then measuring the deflection.

The force vs. displacement curves for the experiments performed in Barsotti and Ligaro (2011), Veldman (2005) and Zhu *et al.* (2008) all showed similar trends. Initially, the relationships were linear and as the displacement increased and the wrinkles appeared, the relationship became non-linear as the beam lost its stiffness. The aforementioned models were all modelled using a constant pressure applied to the membrane. However, this pressure modelling method did not take into account the change in volume of the structure due to deformation, that would in turn cause a change in the pressure.

In research by Cavallaro *et al.* (2007), four-point bending tests were performed on numerical models of uncoated, plain-woven fabric inflatable tubes. These tests were performed using ABAQUS' explicit solver in order to explore the contributions of strain energy and pressure-volume work (PV-work) on the

bending behaviour of the tubes. The governing energy balance equation for the four-point bending tests is expressed in Equation 2.2:

$$\Delta E_{int} = \Delta E_{strain} + \Delta E_{kinetic} + \Delta \int PV + \Delta E_{dis}, \tag{2.2}$$

where:

$$\Delta E_{int} = \int F_{react} d\delta_{load\_pt} = W_{ext}. \tag{2.3}$$

In Equation 2.2, ΔE_{int} represents the change in internal energy of the tube which is equal to the external work (W_{ext}) done on the beam during the test. This value can be calculated by integrating the force vs. displacement (F_{react} vs. δ_{load_pt}) graph for the four-point bending test, as shown in Equation 2.3. The other energy components that make up ΔE_{int} are: the fabric strain energy (E_{strain}), the kinetic energy of the system mass ($E_{kinetic}$), the work done by compressing the air (PV) and the viscous dissipation energy due to damping (E_{dis}).

Multiple four-point bending simulations were performed on a model with a linear elastic Young's modulus at differing pressures. The strain energy, PV-work and the external work values were plotted against each other at the respective pressures, forming the graph seen in Figure 2.2. The kinetic energy and the viscous dissipation energy were omitted from the plot, due to the negligible effect they had in this instance.

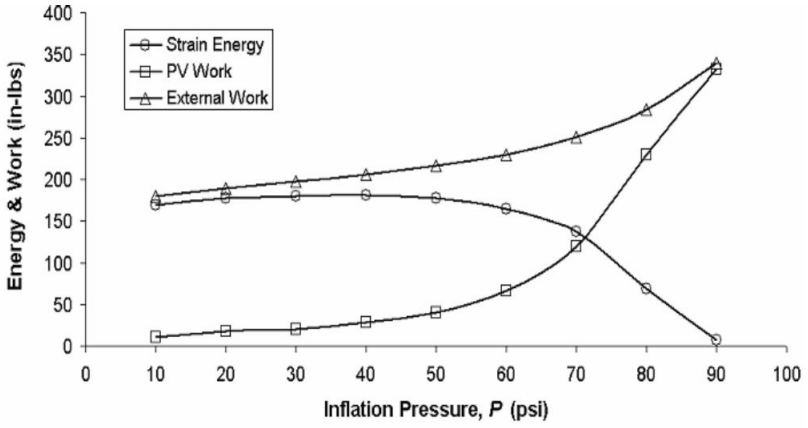

Figure 2.2: Energy & work vs. pressure graph for an inflatable tube during a four-point bending test (Cavallaro *et al.*, 2007)

From the results, it was found that at pressures below 30 psi (∼206 kPa), the PV-work contributed to less than 10 % of the external work and the strain energy contributed to more than 90 %. However, as the pressure increased, the contribution of the strain energy to the external work reduced to nearly nothing. Therefore, this showed that at higher pressures the PV-work dictated the bending behaviour and the effect of the material properties were minimal. However, at lower pressures, the material properties dictated the behaviour.

A set of tests involving numerical models inflated using an airbag model were performed by Venter (2011). Unlike the pressure load model, airbag models entail filling a closed volume with an air mass. This air mass behaves according to the ideal gas laws; therefore, when the air mass inside the bag is kept constant and the volume changes, the pressure inside the bag changes respectively. An additional update of the stiffness matrix is also performed after every iteration when making use of an airbag model. This stabilises an almost completely flexible structure (Schweizerhof, 2005).

The aforementioned tests were performed on dunnage bags and simulated using LS-DYNA's explicit solver. Dunnage bags are generally used in shipping scenarios where they are placed in the gap between two objects and then inflated to keep the objects in place during transportation.

In order to validate the numerical model, different sets of tests were performed and the results compared to that of the physical tests. The one set of tests entailed placing the dunnage bag in between rigid planes and then inflating it, see Figure 2.3. The bag dimensions, the pressure and the distance between the planes varied for the different tests.

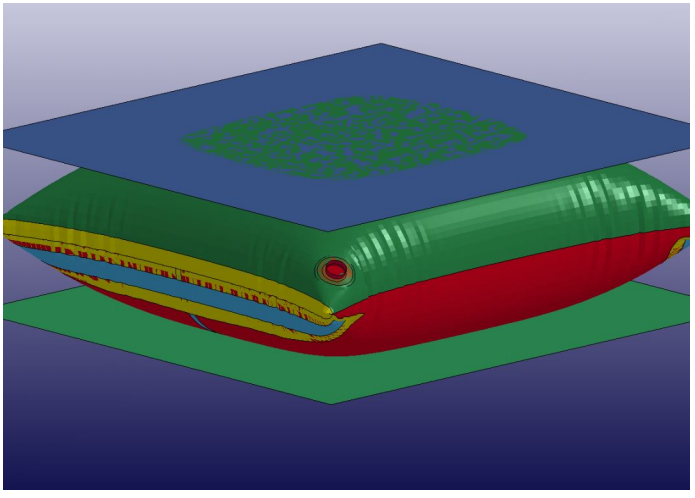

Figure 2.3: Numerical model of an inflated dunnage bag in between two rigid supports (Venter, 2011)

The contact forces for both the numerical and the physical tests were compared and the average error between the two was found to be 6 %, with a standard deviation of 8 %. These results verified that the model could give strong trend information for a simulated loading.

2.2 Aerofoil Profiles

In the aerospace community, wings are used extensively with their shapes and sizes varying widely. In order to describe these shapes and sizes, standard aerofoil nomenclature is used. An asymmetric aerofoil profile labelled with its respective nomenclature can be seen in Figure 2.4. The leading and trailing edges of a wing are the front and rear of the aerofoil profile respectively, where the distance between the two edges is called the chord. The span of a wing refers to the length of the wing from the one tip to the other.

The ratio of the span to chord length is often used, as the ratio plays a role in many facets of the performance of the wing; whether it be in terms of load bearing capacity or aerodynamic performance. This ratio is called the aspect ratio. Another important ratio to consider is the taper ratio, which is the ratio of the chord length at the tip to the chord length at the root of the wing. If the chord lengths remain the same size then the ratio is unity.

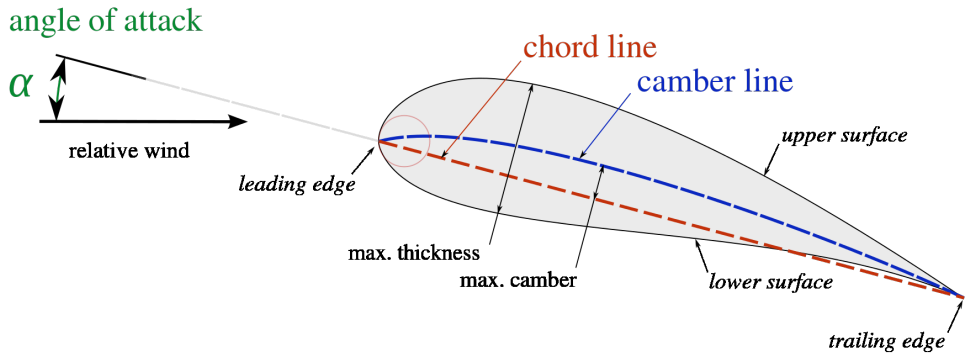

Figure 2.4: A side view of an asymmetric aerofoil labelled with its respective nomenclature (Cleynen, 2011)

The line that is situated in the middle of the top and bottom surface is called the camber line. The largest distance that occurs between the top and bottom surface is called the thickness. The thickness is a parameter that is used when selecting a National Advisory Committee for Aeronautics (NACA) aerofoil. For a symmetric four-digit NACA aerofoil the shape is expressed by "NACA

$00xx$" with xx replaced by the percentage of the thickness to the chord. The corresponding aerofoil profile's top half can be plotted with Equation 2.4:

$$y = 5t[0.2969\sqrt{x} - 0.1260x - 0.3516x^2 + 0.2843x^3 - 0.1015x^4], \tag{2.4}$$

where y is half the thickness at a given x value, t is the maximum thickness as a fraction of the chord and x is the position along the chord, ranging from 0 to 1.

For an asymmetric aerofoil's thickness, more specifically a cambered four-digit NACA aerofoil, the same equation as the symmetric profile is used. However, the difference is that the camber line is not straight along the chord line. The new asymmetric camber line is expressed by the m and p in the "NACA $mpxx$" description. The m and p represent the maximum camber height $(m/100)$ and the position along the chord of the maximum camber height $(p/10)$ respectively. The equation for the height of the camber line, y_c, at its corresponding chord position, x, can be seen in Equation 2.5:

$$y_c = \begin{cases} \frac{m}{p^2}\left(2px - x^2\right), & 0 \leq x \leq p, \\ \frac{m}{(1-p^2)}\left((1-2p) + 2px - x^2\right), & p \leq x \leq 1. \end{cases} \tag{2.5}$$

The lift and drag forces acting on an aerofoil are the forces perpendicular and parallel respectively to the direction of flow. Each of the forces consist of pressure and skin friction components. Altering the angle the chord line makes relative to the direction of flow, known as the angle of attack (α), the lift and drag acting on the aerofoil is either increased or decreased depending on the orientation of the specific aerofoil.

The drag and lift forces depend on the fluid density (ρ), the upstream velocity (V), and the size, shape and orientation of the body, and it is thus not practical to list these forces for a variety of situations. Therefore, it is more convenient to work with drag and lift characteristics of the body in the form of dimensionless values. The coefficient of lift and drag (C_L and C_D respectively) are dimensionless values that characterise the lift and drag of a body. This relationship can be seen in Equation 2.6:

$$C_{L,D} = \frac{F_{L,D}}{\frac{1}{2}\rho V^2 A}. \tag{2.6}$$

The ratio of the C_L to the C_D is often plotted against the angle of attack for a specific aerofoil at a specific Reynold's number. This plot generally increases

with the angle of attack until the aerofoil stalls and the ratio starts decreasing. This stalling of the aerofoil is due to a phenomenon called flow separation. This phenomenon is when the fluid separates from a body and forms a separated region between the body and the fluid stream, that contains backflows and recirculated fluid. When flow separation occurs on the top surface of a wing it increases the drag and drastically reduces the lift produced, thus causing the stall. Therefore, the aerofoil profile should be carefully selected to reduce the degree of flow separation (Cengel and Cimbala, 2014).

2.3 Inflatable Aerofoils

Previously, Simpson (2008) explored numerous material configurations for inflatable wings, consisting of: an unsupported film (for example polyethylene), a restraint and bladder combination (consisting of vectran as the restraint and polyurethane as the bladder), and finally, a coated fabric (for example polyurethane coated nylon).

(a) Unsupported film (b) Restraint and bladder (c) Coated fabric

Figure 2.5: Different material layups used for inflatable wings (Simpson, 2008)

The restraint and bladder configurations, as well as the coated fabric configurations, are able to support a larger inflation pressure, compared to the unsupported film; and thus, provides the inflatable object with a larger stiffness. A problem with these two layups is that physical samples are difficult and time-consuming to construct. This is the case for the restraint and bladder configuration because for each physical model the bladder and restraint need to be constructed separately.

The coated fabric option could also potentially pose a problem due to the large thickness relative to the unsupported film. This might make sealing methods (such as heat sealing) problematic, due to the large amount of material required to be heated as well as the difference in melting points for the fabric and the material coating it.

Many of the inflatable wings constructed in the past were made using multiple inflation cavities separated by the spars of the wing. The restraint components of an inflatable wing using a restraint and bladder configuration can be seen in Figure 2.6. For the other two configurations, the same structure has also been used.

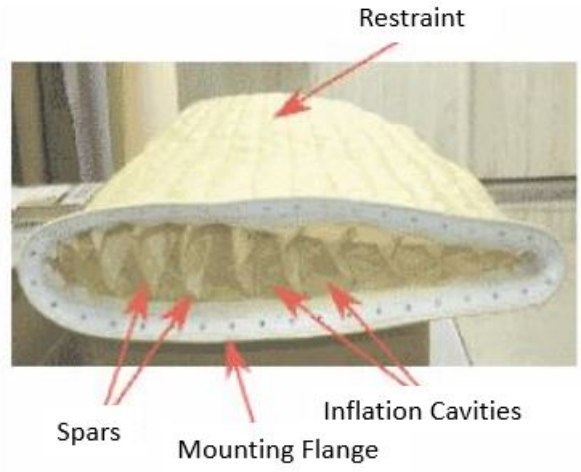

Figure 2.6: Internal structure of the restraint for a restraint and bladder inflatable wing configuration (Rowe, 2007)

Two different trailing edge configurations for inflatable wings have been used in the past, see Figure 2.7. The first consists of the trailing edge consisting of the inflation cavities of the aerofoil (Rowe, 2007). This is a simpler design, however, it creates a blunt trailing edge possibly hindering aerodynamic performance. The second configuration consists of a rigid structure attached near the trailing edge in order to produce a sharper tip (Haight *et al.*, 2006). This sharper edge allows the profile to fit that of the ideal profile better than the blunt edge. However, the complexity of the wing's construction is increased.

(a) Trailing edge without rigid structure (Simpson, 2008)

(b) Trailing edge with rigid structure (adapted from Simpson (2008))

Figure 2.7: Two different trailing edge configurations used for inflatable wings

For inflatable aerofoils with multiple inflation cavities, thicker aerofoil profiles were used even though the thinner aerofoils are more desirable for good aerodynamic performance. This is due to the fact that thicker wings are easier to manufacture and there is less of a trailing edge reduction, thus maintaining the aerofoil profile better (Simpson, 2008).

In aerofoil theory, it can be seen that the larger the relative thickness of the aerofoil, the better the stalling characteristic. However, for aerofoils with a relative thickness of more than 30 %, the drag force increases substantially (Li, 2017). For the case of wings of UAVs on the micro or mesoscale with low

chord lengths, the Reynolds number remains relatively low (between 1.5×10^4 and 5×10^5). This can be seen in Figure 2.8, showing a plot of the Reynolds number vs. Mach number for a wide range of flying objects.

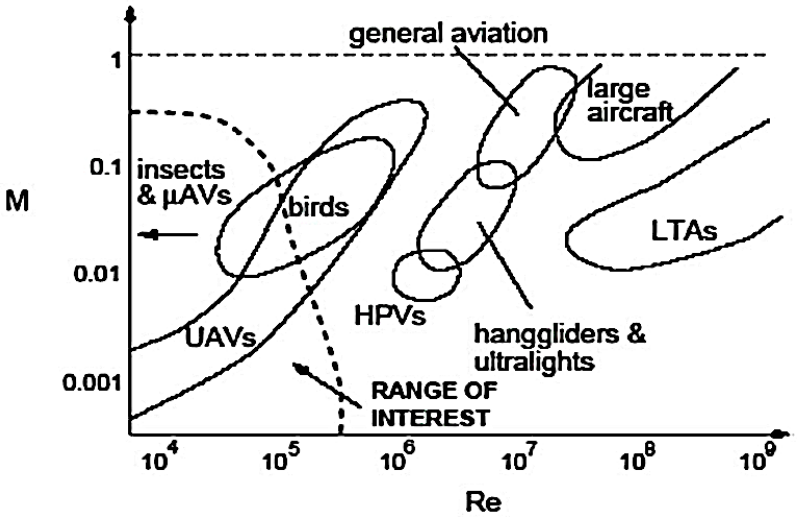

Figure 2.8: Reynolds number vs. Mach number for a wide range of flying objects (Lissaman, 1983)

In order to keep the inflated aerofoil shape close to the ideal aerofoil shape, skins were attached to the wing by Haight *et al.* (2006) to reduce the bumpy profile of the aerofoil. However, Santhanakrishnan and Jacob (2005) shows that the bumpy profile improves the aerofoil performance, as the surface roughness from the bumpy profile trips the laminar flow into turbulent flow over the wing. This turbulent boundary layer was found to be more resistant to flow separation and therefore the flow rejoins downstream producing a smaller pressure drag compared to the ideal aerofoil profile. This is confirmed in Figure 2.9 which visualises the streamlines of the flow over an ideal and bumpy aerofoil at $\mathrm{Re} = 5\times10^4$ and $\alpha = 4°$. This improvement in the aerodynamic performance of the bumpy aerofoil, as opposed to the its smooth counterpart. in the low Re region can be seen in Figure 2.10.

For the wing shown in Figure 2.6, an FE model was also created by Rowe (2007). The bladder of the wing was omitted from the model and only the restraint was modelled in ANSYS as shell elements. The wing was created with the aerofoil geometry as the target inflated shape. Four different internal pressures were separately applied to the elements of the wing as an outward pressure loading. Two different explicit load cases were applied to the wing, the first was a cantilever bending test with a vertical force applied to a node at the position corresponding to the position of the force in the physical model.

Multiple simulations were run using the lowest pressure in order to find the optimal configuration.

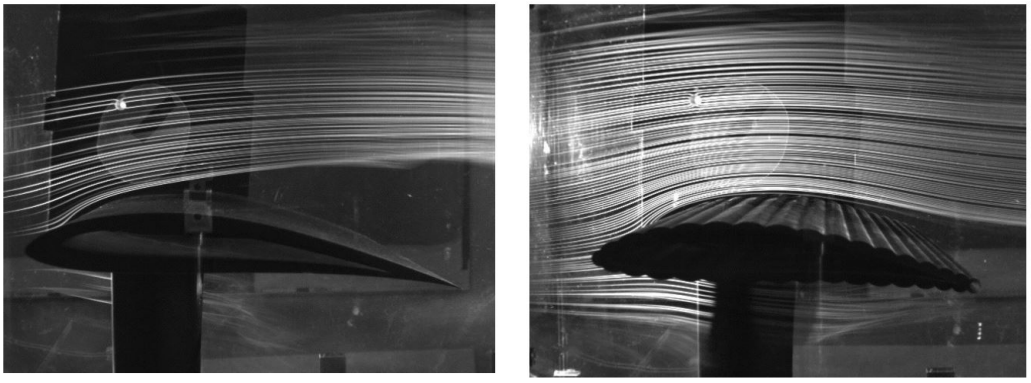

(a) Ideal aerofoil (b) Bumpy aerofoil

Figure 2.9: Figures comparing the flow separation occurring between an ideal and bumpy aerofoil at Re = 5×10^4 and $\alpha = 4°$ (Santhanakrishnan and Jacob, 2005)

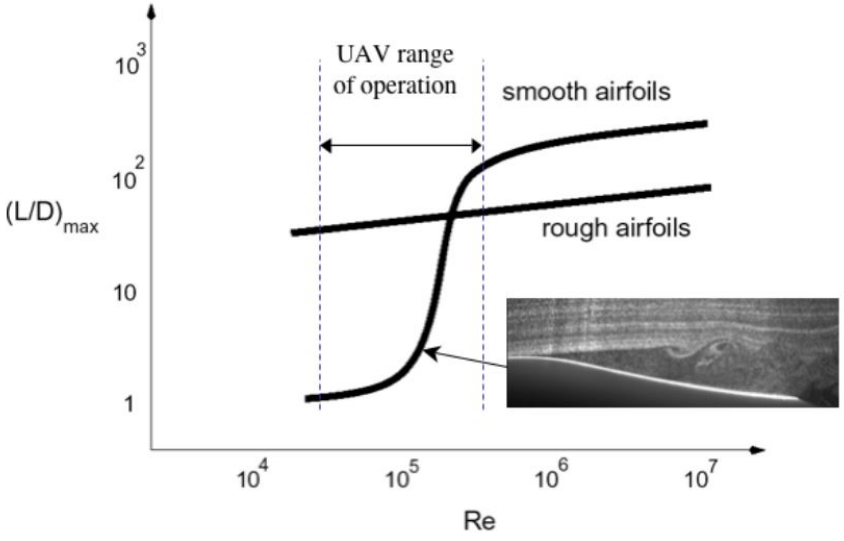

Figure 2.10: C_L/C_D vs. Re number for smooth and bumpy aerofoil (Santhanakrishnan and Jacob, 2005)

Initially, the simulation did not converge as it was thought that the difference between the Young's modulus and shear modulus of the material was too large. The difference between the two moduli was decreased and different sizes for the two moduli were tested. It was found that the shear modulus had very little effect on the stiffness of the wing.

For all of the wing simulations at the lowest pressure, the numerical and the physical models initially correlated well and then diverged as the point load value increased, with the numerical model being stiffer than that of the physical model. The numerical results for the wing at the second-lowest pressure were nearly equivalent to the physical results. However, the numerical results for the lowest and second-lowest pressures were also nearly equivalent. Therefore, this indicated that the bending stiffness of the wing did not increase with an increase of pressure as the physical model did. No results were obtained for the wing inflated to the highest two pressures as they both failed to converge.

The second load case consisted of a wing twist case where, just like the bending test, the wing root was fixed in all degrees of freedom (DOF). Two equal but opposite vertical loads were applied to the nodes at the leading and trailing ends of the wing tip. The angle of twist was computed using the calculated deflections of the leading and trailing edge points. Again, the two lowest pressures were tested and it was found that the numerical model was stiffer than the physical model. On average, the numerically determined angle of twist was only 16 % and 29 % of the experimental results for the lowest and second-lowest pressures respectively. However, unlike the bending tests, increasing the internal pressure seemed to increase the torsional stiffness of the wing.

2.4 Summary of Literature

The work presented in this chapter aimed to provide a background to the problem at hand. The previous work and concepts from the literature aided in the decision making process when formulating the design methodology.

A basic overview of the stiffness for inflatables is encapsulated in the hoop stress in Equation 2.1. This also serves as a means for determining the pressure at which the membrane material will yield due to over-inflation. In the tests performed in the previous literature, which compared the stiffness of bending beams under load, it was found that the onset of wrinkling dictated the stiffness of the beam. Therefore, if the wrinkling is not properly captured then the results could vary from the physical. A testing method therefore needed to be chosen that would not be dependant on the accuracy of the wrinkle prediction (discussed further in Section 3.2).

For the numerical modelling of inflatables, the inflation model used proved to make a significant difference to the results. Traditional pressure loads applied to the elements did not seem to do well in the stiffness prediction of the model, especially seen in the FE model of the wing by Rowe (2007). However, when using an airbag model for the inflation, more accurate stiffness results were acquired, as seen in the tests done by Venter (2011).

Finally, for the inflatable wing, the unsupported material configuration was chosen over the other two due to the simplicity of the configuration's construction. For this same reason, the trailing edge configuration made up of the inflation cavities was chosen. The UAV's are intended to operate in the low Re number range as seen in Figure 2.8. Therefore, the bumpy aerofoil profile was chosen due to its ability to trip the downstream flow into turbulence and thus, decrease the flow separation.

Chapter 3

Methods and Materials

3.1 Membrane Material

As discussed in Section 2.3, three different membrane configurations were considered; however, the configuration chosen for this research was an unsupported film, in the form of low-density polyethylene (LDPE). It was chosen as multiple designs needed to be constructed and there was an abundance of the material available. However, this choice compromised the maximum inflation pressure of the bag and thus the stiffness of the inflated bag.

3.1.1 Low-Density Polyethylene

The mechanical properties of the LDPE were initially unknown and therefore testing was required to determine them. Uni-axial tensile tests were performed on the LDPE film, according to the ASTM D882–12 standard, in order to determine the stress vs. strain behaviour of the material. Due to the manufacturing process of the film, where the material undergoes large permanent deformations from its isotropic state when it is drawn through a die, the film has orthotropic material properties. Therefore, ten samples were tested for each of the two principle directions.

The stress vs. strain data from the tensile testing of the two principle directions can be seen in Figure 3.1. The averages of the two data sets are represented by solid lines, where a 99 % confidence interval of the data is plotted as a shaded area. The plot shows that in the linear region of the two curves, they are very similar; however, as plasticity sets in, around 5 MPa, the curves start to deviate. This confirms the assumption of the orthotropic material properties.

The Poisson's ratio for the film was not tested, instead a Poisson's ratio was chosen based on literature by Nitta and Yam (2012). This is due to the lack of equipment needed to perform the tests. The elongation rate during the testing

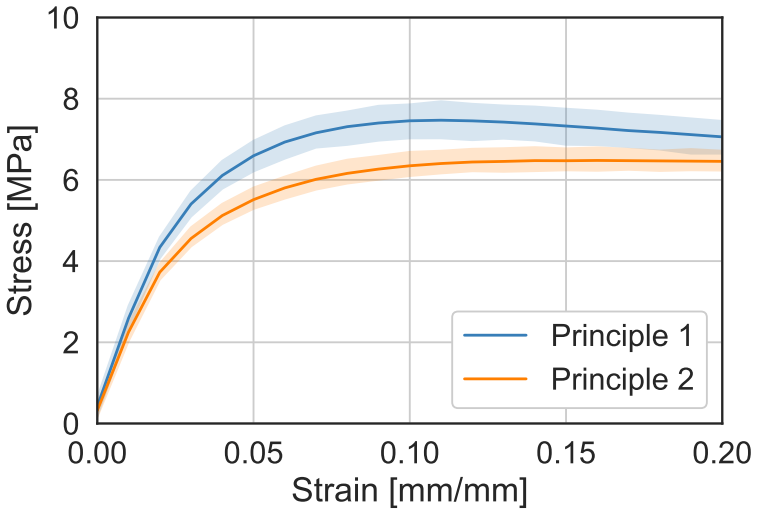

Figure 3.1: Tensile test results of the LDPE film in the two principle directions

was at 20 mm/min, and it was found that as the sample elongated, so changed the Poisson's ratio. From these tests, the Poisson's ratio was found to vary between 0.3 and 0.5.

3.1.2 Manufacturing

Before a complex inflatable structure consisting of multiple, different sized inflation cavities is constructed a simpler model first had to be used. This entailed initially using a single cavity model. Once it had been found that the numerical model represents the physical model well, then the model's complexity could be increased.

The single cavity bags were constructed using a single sheet of polyethylene, heat welded together. The first weld is made along the length of the bag, creating the diameter of the bag. The ends of the bag were then simply welded together with a flat weld, a visualisation of the bag construction can be seen in Figure 3.2. The black lines represent the polyethylene film, where the red lines and circles represent the welds parallel and perpendicular to the view respectively.

As the geometries of the model change with an increase in complexity, making use of heat welds to seal the membrane will continue to be used. However, with an increase in geometry complexity, the positioning of these welds will change. These changes will be addressed when the change is encountered.

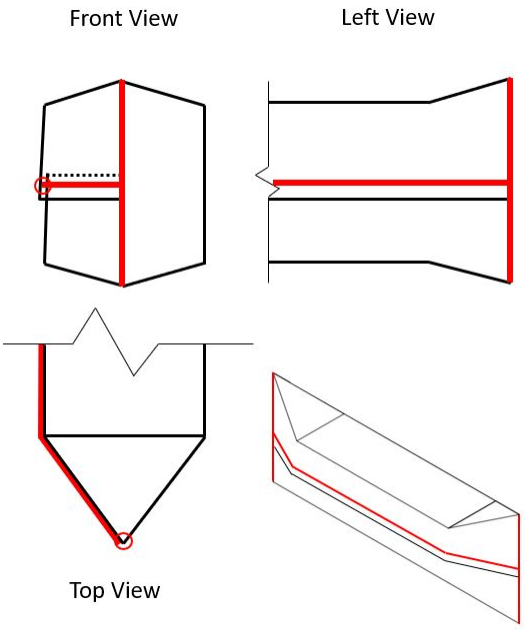

Figure 3.2: A visualisation of the construction of a single cavity bag using a single sheet of LDPE, heat welded together

3.2 Experimental Techniques

This research was reliant on the use of numerical models for the numerical shape optimisation to acquire the aerofoil profile; however, tests were performed on physical models for the validation of the numerical models. These tests were performed to validate the model's inflated shape as well as its inflated stiffness under load. Break downs on the methods used and the reasons why they were used are encompassed in this section.

3.2.1 3D Scanning

In order to validate the inflated shape of the numerical models, the geometry of the physical models needed to be captured. This was done by making use of the HP 3D Structured Light Scanner which has a maximum resolution of 0.05 mm (Hewlett-Packard, 2016). This 3D scanner works by projecting a black and white pattern onto an object and then capturing the patterns on the object using high-resolution cameras. The scanning setup, seen in Figure 3.3, made use of two cameras mounted on sliders on either side of the projector. The angle between each camera and its respective slider was adjustable. A single camera could have been used, however, the use of two cameras increased the accuracy of the scans (Hewlett-Packard, 2016).

Figure 3.3: The 3D scanning setup used throughout the research, with two cameras positioned on either side of the projector

Once the object geometry had been scanned, the geometry was exported as a Standard Tessellation Language (STL) file. The geometry of the STL object consisted of an unstructured triangular mesh which could be extracted using the Python package, `numpy-stl`.

3.2.2 Four-Point Bending

The testing method used to validate the stiffness of the single cavity inflatable bags was the four-point bending test. This method was also used to deform the model, in order to compare the single cavity bags' shape under deformation. The four-point bending tests were used as the presence of wrinkles in the membrane did not diminish the structural integrity of the model as much as cantilever tests. This is important, as accurately capturing the behaviour of the wrinkles is non-trivial and the structural stiffness is dependant on the wrinkling behaviour, as discussed in Section 2.1.

Displacement control was also used to mitigate accelerated failure in the models as force control has the chance for large increases in corresponding displacement, due to global buckling of the membrane. Therefore, this would not accurately capture the stiffness of the models. The displacement control method used consisted of using a tensile testing machine and a 1 kN load cell to gather the respective force data. A four-point bending test rig that attached to the tensile testing machine was created for this purpose.

The isometric and dimensioned front view of the four-point bending test rig assembly, in its test configuration, can be seen in Figures 3.4a and 3.4b respectively. Additionally, the drawings used to construct the different parts of the four-point bending rig can be found in Appendix A.

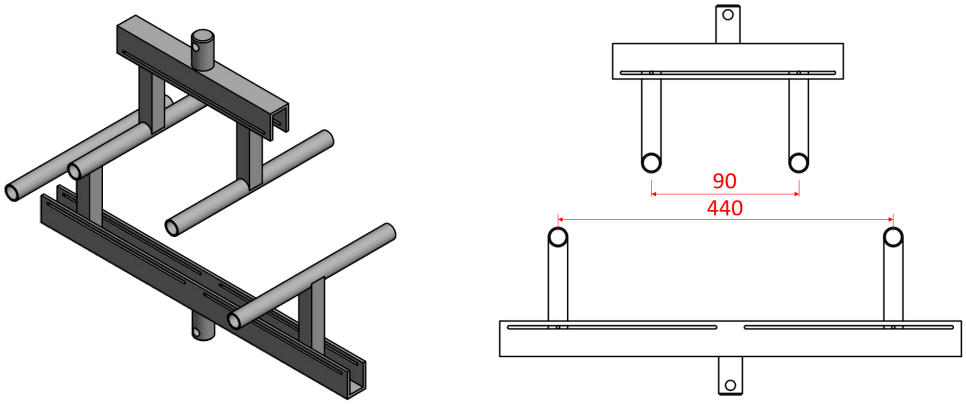

(a) Isometric view of four-point bending test rig assembly

(b) Front view of four-point bending test rig with dimensions

Figure 3.4: Four-point bending test rig constructed for stiffness testing of inflatable tubes

3.3 Considerations for Non-Linear Finite Element Analysis

Multiple FE models were created and simulated for this research, whether it be for the prediction of the inflated shape of a membrane or for determining the stiffness of a model through four-point bending tests. Due to the nature of the membrane inflation and the four-point bending tests being time dependant, dynamic FE analyses were used for both aforementioned cases. The equation governing the force equilibrium for a linear dynamic response can be seen in Equation 3.1:

$$[\mathbf{M}][\ddot{\mathbf{x}}] + [\mathbf{C}][\dot{\mathbf{x}}] + [\mathbf{K}][\mathbf{x}] = [\mathbf{r}]. \tag{3.1}$$

In Equation 3.1, the matrices $\mathbf{M}$, $\mathbf{C}$ and $\mathbf{K}$ represent the mass, damping and stiffness matrices respectively with $\mathbf{x}$ representing the displacement vector and the $\mathbf{r}$ force vector. The configuration for the static analysis is the same as the dynamic, barring the time dependant terms $\ddot{\mathbf{x}}$ and $\dot{\mathbf{x}}$ (nodal accelerations and velocities respectively).

For non-linear dynamic FE analysis, the same equation observed in Equation 3.1 is used. However, instead of the matrices and the force vector staying constant, one or more become dependant on $\mathbf{x}$ or a derivative thereof. Therefore, for each iteration the new matrix or vector needs to be calculated prior to solving the equations, increasing the computation time. There are a number of non-linearities that can be encountered in FE analysis. However, only the non-linearities that are present in the FE analyses in this research shall be discussed in this section.

In the simulations performed, there were two instances where contact was used: the contact between the supports and the inflated membrane during the four-point bending test simulations; as well as the self-contact of the membrane when it undergoes wrinkling. When contact is used in the simulation, the computational costs involved are increased. This is because, for every time step, an algorithm searches for potential penetration of slave nodes through a master segment. If penetration is found, then a force proportional to the penetration depth and the contact stiffness is applied in order to eliminate the penetration. This concept is illustrated in Figure 3.5.

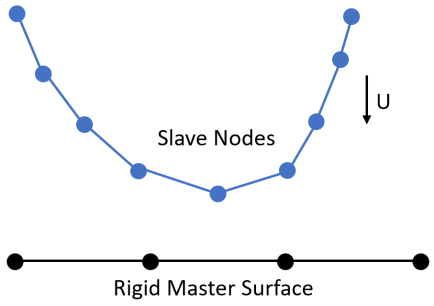

(a) Slave nodes displacing towards master surface prior to penetration

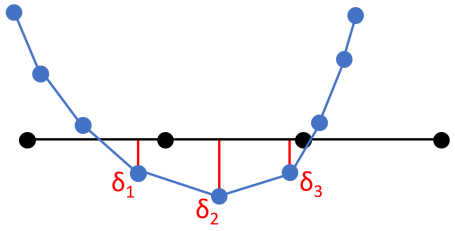

(b) Penetration of the slave nodes through the master surface

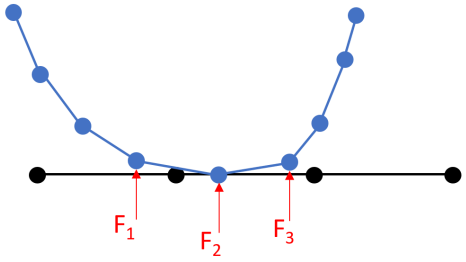

(c) Forces applied to the slave nodes proportional to the contact stiffness and the penetration distance

Figure 3.5: An illustration of how a contact algorithm works in FE analysis

Another type of non-linearity encountered in the models was geometric non-linearity. This is attributed to the displacement dependent loading with regards to the pressure inside the membranes and the large element rotations/displacements occurring in the simulations.

In order to accurately model the change in stiffness of the inflated membrane while under load, an airbag model was used. This entailed modelling the air in the bag as an ideal gas with a fixed mass whereby a change in volume (bag undergoing deformation) would cause a change in the internal pressure. Therefore, for each time step, the new volume needed to be determined for the membrane before its pressure could be determined. This is a highly non-linear process as the membrane's pressure is displacement dependant, thus significantly contributing to the overall computation time.

The simulation of the inflation of the membrane initially consists of the deflated shape being flat and rectangular and then once it is inflated the bag takes a more cylindrical shape. The elements on the edge of the bag therefore undergo large deformations as they flatten out during the inflation. No large stresses are imposed on the edge elements straightening out during the inflation, due to the lack of bending stiffness in the membrane.

A source of instability in the simulation could occur if there is too large of a displacement in a single iteration, as the accuracy of the solution decreases with large deformations. As the iterations continue the accuracy and stability will continue to decrease whereby the instability could ultimately lead to a lack of convergence of the solution. In order to mitigate this, smaller time steps could be used (for smaller increments) or the bag could be inflated gradually, instead of a rapid inflation.

3.4 Implicit vs. Explicit Solvers

In order to solve for the response of the dynamic simulations, either an implicit or explicit solver needed to be used. For implicit analysis, the solution for each time step is iteratively calculated in order to establish an energy equilibrium within a certain tolerance. This is done by solving for the $\mathbf{x}$ values in Equation 3.1, which can be computationally expensive when $\mathbf{K}$ is large, especially when there are non-linearities. Explicit analyses entails solving for the nodal accelerations at each time step, directly and cheaply, as the mass matrix is lumped (consists of only diagonals). Once the accelerations are calculated, central-differencing or a similar method is used to determine the velocities and displacements, and henceforth the strains.

The time steps for both solvers are also different. Implicit solvers are unconditionally stable and their time steps are generally orders of magnitude

larger than that of the explicit solvers (Livermore Software Technology Corporation, 2019). Explicit solvers are, however, only conditionally stable and their stability depends on their time steps being less than the Courant time step. This time step can be changed by altering a number of parameters and can, therefore, ultimately speed up simulation times (to be discussed further in Section 3.6).

An explicit solver was chosen to compute the response for the dynamic simulations. This was chosen over an implicit solver due to the explicit solver's ability to potentially speed up simulation times. It has also been found that when using the Newton-Raphson method for the implicit integration during a slow inflation process, large non-physical oscillations can occur and cause a lack of convergence (Jetteur and Bruyneel, 2008). This is due to the buckling of the membrane which causes wrinkling and makes it difficult to reach an energy balance, as the buckling pattern is sensitive to change and with each different pattern, the forces change.

The software package chosen to carry out the simulations was LS-DYNA due to it having an explicit solver as well as it being extensively used for airbag inflation. A feature in LS-DYNA, dynamic relaxation, is also used to improve the accuracy and stability of the simulations during the initial inflation stage.

3.5 Dynamic Relaxation

The solutions to most non-linear dynamic problems are path-dependent, thus results obtained in the presence of dynamic oscillations may not be accurate and they may diverge from reality. A method used in order to amend this is dynamic relaxation, which is an explicit method that consists of introducing an artificial mass dependent damping and inertia to the system. This improves the convergence to a steady-state solution by attenuating the oscillations in the steady-state response. The use of artificial inertia and damping during the transient part of the simulation will, however, not be physical. Therefore, using dynamic relaxation should be restricted to where the objective of the simulation is the final equilibrium position of the structure (Rodriguez, 2011).

Due to its explicit nature, dynamic relaxation is especially attractive in highly non-linear problems in FE analysis, as there is no need for solving large systems of equations. Although the number of iterations to obtain convergence may be quite large, the computation cost for each iteration is very low, making it a very efficient method for non-linear problems.

Due to the number of non-linearities present in the simulations as previously mentioned, using dynamic relaxation was an ideal solution. Additionally, the increased accuracy of the simulations at a small computational cost contributed to the selection. The fact that the transient part is not physical did not influence the simulations performed, as only the final state was required.

3.6 Mass Scaling

As previously mentioned, the Courant time step is the largest time step that an explicit solver can progress per iteration in order to maintain stability. The smaller the time steps, the longer the simulation runs. However, the goal of the FE simulations is to aid the design process; therefore, multiple simulations are required to be run in a relatively short time frame. A good compromise of run time and accuracy was required, and thus mass scaling was incorporated into the model.

The Courant time step is given by:

$$\Delta t = \frac{L_c}{C}, \tag{3.2}$$

with

$$L_c = \frac{(1+\beta)A_s}{max(L_1, L_2, L_3, (1-\beta)L_4)} \tag{3.3}$$

and

$$C = \sqrt{\frac{E}{\rho(1-\nu^2)}}. \tag{3.4}$$

The characteristic length for a shell element is shown in Equation 3.3 where $\beta = 0$ if it is a quad element and $\beta = 1$ if it is a triangular element. The different lengths of the element's side are represented as L_1–L_4, with A_s representing the area of the element.

Equation 3.4 represents the speed of sound through the element with E, ρ and ν being the Young's modulus, the density and the Poisson's ratio respectively. Therefore, according to Equation 3.2, by increasing the element size the time step is increased and so speeds up the simulation. However, since the bag's mesh size will have to be smaller than a certain size in order to maintain

a degree of accuracy, the constants in Equation 3.4 can be changed. The constants in Equation 3.4 will therefore be altered in order to speed up the simulation time.

Changing the Young's modulus and the Poisson's ratio of the material could potentially increase the step size. However, changing the mechanical properties of the material would influence the stiffness of the material and thus the simulation results. By increasing the density, and thus the mass, it has been found that simulation times have been reduced while not significantly changing the response of the system (Olovsson *et al.*, 2005). Mass scaling was therefore adopted in this research, bearing in mind that the increased mass would introduce larger inertia into the system.

3.7 Metamodelling

Metamodeling consists of fitting a mathematical model to the responses of simulations in order to create a model of the response vs. design variables. They are able to model the response accurately with relatively few design points. This saves time as optimisations can instead be performed on the metamodel. Additionally, the responses with the changes in variables can be visualised, thus aiding the designer. However, in order to achieve a high accuracy for the metamodel the correct mathematical model needs to be selected for the data. These mathematical models take different forms such as low-order polynomials, neural networks and others that shall not be discussed in this thesis but are discussed by Wang and Shan (2006).

3.7.1 Low-Order Polynomial Functions

The optimisations in this research were all performed using LS-OPT, unless otherwise specified. LS-OPT is an optimisation software that works well in conjunction with LS-DYNA and thus was the main reason for using it. However, a downside to using LS-OPT was that the use of metamodels, optimisers and point selection algorithms were limited to the ones available in the program. Therefore, the only metamodels, optimisers and point selection algorithms considered were the ones available in the program.

Polynomials, mostly in the form of linear and quadratic functions, are often used in metamodels to model problems that either have a linear trend or a slightly non-linear trend. An example of a metamodel with two design parameters can be seen in Figure 3.6. These metamodels are cheap, and easy to construct and interpret (Wang and Shan, 2006). Due to the low fit order of the model, it is less susceptible to noise and over-fitting compared to the higher-order models.

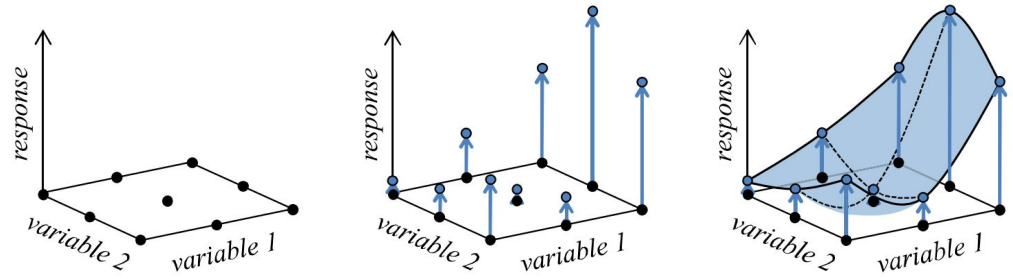

(a) Design of experiments (b) Function evaluations (c) Built metamodel

Figure 3.6: Process of building a metamodel (Ryberg, 2017)

Over-fitting occurs when the model is too complex and the noise of the data is captured. With over-fitting, the fits can be very accurate for a particular set of data, but fail to accurately fit additional data. An example of different model fits can be seen in Figure 3.7. However, the low order models have a downfall, as it is not able to accurately model highly non-linear relationships. This can cause the model to under-fit the data. The applications for low-order polynomial metamodels are therefore limited.

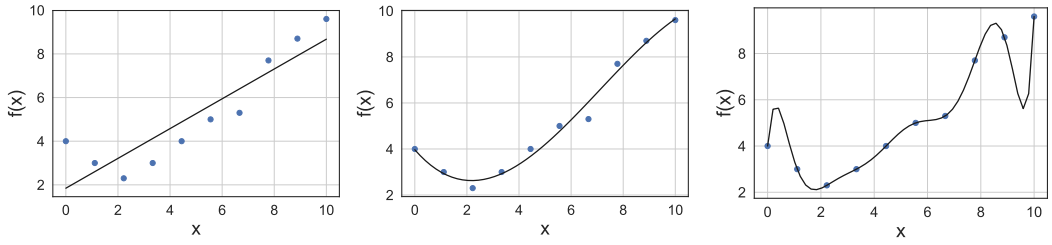

(a) Under-fitting (b) Good fit (c) Over-fitting

Figure 3.7: Comparison of different model fits

3.7.2 Radial Basis Function Neural Network

Neural networks model the relationship between a set of input variables and an outcome with hidden layers in between. These hidden layers are made up of small computing elements called neurons. A transfer function is then evaluated by the neuron from the biased and weighted input values and an output value is produced (Louis, 2001). The general structure of a neural network can be seen in Figure 3.8.

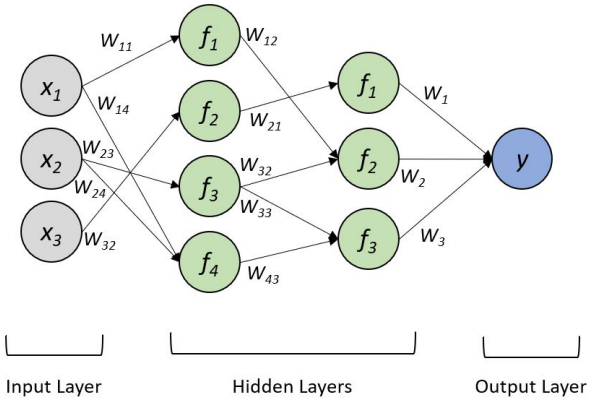

Figure 3.8: The general structure of a neural network with the weighted inputs to the neurons

The radial basis function (RBF) neural network is a common type of neural network which consists of only one hidden layer of radial units. Each of these units model a response function that is peaked at the center and then monotonically varies outwards. A RBF metamodel consists of a linear combination of radially symmetric functions to approximate highly non-linear responses (Ma *et al.*, 2008). The model can be expressed as:

$$y_{RBF}(x) = \sum_{i=1}^{n} w_i \phi(||x - x_i||), \tag{3.5}$$

where x and x_i are the vector of the input variables and the vector of input variables at the i^{th} sampling point respectively. A weighting function, w_i, is applied to the RBF, represented by ϕ. This is a function of the Euclidean norm which represents the radial distance. The RBFs can come in many forms; however, the two most commonly used are the Gaussian function and Hardy's multiquadratics (Ryberg, 2013). These two functions are represented in Equations 3.6 and 3.7 respectively:

$$\phi(r) = -exp\left(\frac{r}{c}\right), \tag{3.6}$$

$$\phi(r) = \sqrt{r^2 + c^2}, \tag{3.7}$$

where c is a shape parameter that controls the smoothness of the curves and r is the Euclidean distance.

A correctly weighted sum of sufficient radial functions will always be enough to model any set of training data, this is why RBFs are extremely good at

modelling highly non-linear data (Stander *et al.*, 2010). The formal proofs can be found in the form of Hartman *et al.* (1990) and Park and Sandberg (1993).

Therefore, RBFs are able to achieve the same metamodel accuracies as the feedforward neural network, another neural network commonly used in metamodelling (Terrence, 1999); however, it can be trained orders of magnitude faster.

3.8 Design of Experiments

Experimental design is the process of selecting design points in the design space that are to be used in the simulations. There are many different point selection algorithms available, such as the factorial, D-optimal, Latin Hypercube and distance-based. Each of these algorithms have their specific advantages. For the simulations performed here, a distance-based algorithm was used for every instance and therefore, a detailed breakdown will be provided. A description of the remaining algorithms will not be specified; however, more information on these algorithms can be found in Santner *et al.* (2003) and Pronzato and Müller (2012).

The distance-based algorithms are commonly used when there is no need to impose a strong bias on the spread of the sample points in the design space (Stander *et al.*, 2010). Instead, the points are uniformly scattered. This therefore allows the design space to be filled with sufficient points with a moderate number of experimental points, requiring fewer evaluations to create the metamodel. This uniform spread characteristic is particularly useful when utilised with a non-parametric model such as a neural network.

There are many different distance-based algorithms available such as the minimax and maximin distribution, to name two. The maximin distribution was the distance-based algorithm chosen as it was the only distance-based algorithm available in LS-OPT. It entails maximising the minimum distance between points in the design space. The minimax distribution is very similar; however, it minimises the maximum distance between design points. A comparison between these two distributions can be seen in Figure 3.9.

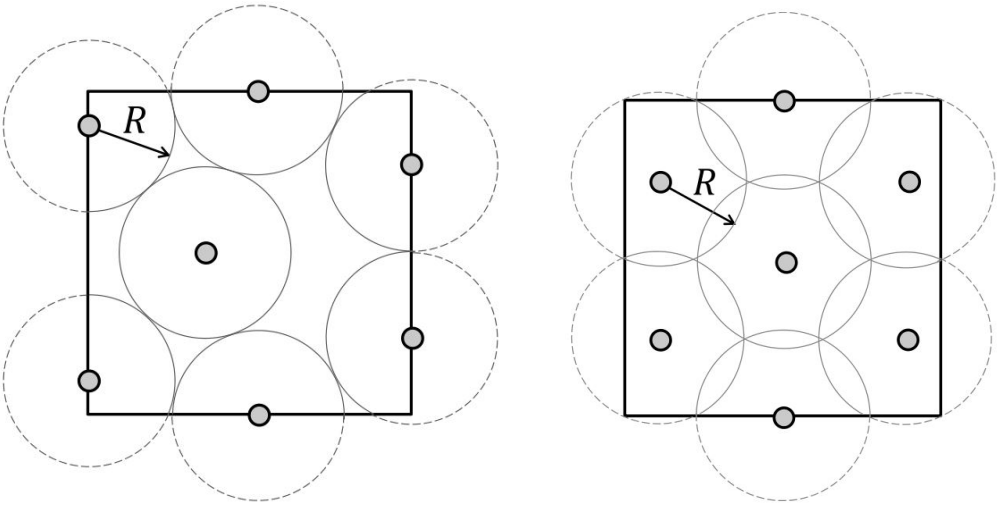

(a) A maximin distribution (b) A minimax distribution

Figure 3.9: Comparison between the maximin and minimax space-filling distributions (Ryberg, 2013), with R representing the radial distance

3.9 Optimisation Algorithms

Once the metamodel has been built, optimisations are then able to be performed on it. Just as the selection of the metamodel is important and case-specific, so is the selection of the optimiser used in conjunction with it.

3.9.1 Leapfrog Optimiser

The unconstrained leapfrog optimiser is a gradient-based method developed by Snyman (1982), in which no explicit line searches are performed. The optimiser attempts to minimise a n variable function by considering the dynamics of a mass particle in a n-dimensional force field, where the function value to be minimised is the potential energy of the particle at point $x(t)$ at time t.

The equations of motion of the particle that are subject to an initial position and velocity are calculated by approximating the associated trajectory using the "leapfrog" method, explained in more detail by Snyman (1983). Another aspect of the method entails reducing the kinetic energy of the particle as it moves uphill. The potential energy of the particle is also systematically reduced, allowing the particle to settle in a local minimum. This method was proven robust, as it is relatively insensitive to local inaccuracies and discontinuities, making it effective for minimising problems that produce noisy function values (Snyman, 2000).

The constrained leapfrog algorithm entails utilising the same formulation as the unconstrained algorithm but with a penalty function applied to it. This involves increasing the objective function value of the sample if the value falls outside the specified constraints. The application of the penalty function occurs in three phases:

- Phase 1 entails applying mild penalty factors to the active constraints and performing the optimisation. If no constraints are active upon convergence, optimisation can be terminated as the optimum is found. If any constraints are active then it proceeds to Phase 2.
- Phase 2 increases the penalty factor to penalise violations of the constraints more strictly and the optimisation is performed again.
- In order for Phase 3 to be initiated the number of active constraints has to be larger than the number of design variables. In this case, a compromised solution is determined, otherwise, if Phase 3 is not initiated the solution from Phase 2 is the optimal value.

3.9.2 Genetic Algorithm

Evolutionary algorithms are those that aim to mimic nature and have the characteristics of being extremely robust, have an increased chance of finding the global minimum (compared to local optimisers) and are able to deal with discrete optimisation problems very well (Venter, 2010). However, the computational cost of these algorithms is high compared to gradient-based methods. Genetic algorithms (GAs) are one of the more established evolutionary algorithms inspired by Darwin's principle of "survival of the fittest" (Holland, 1976).

The optimisation loop for the GA implemented in LS-OPT can be seen in the flow chart in Figure 3.10. The initialisation of the loop starts by generating an initial parent population of a set of individuals (design points). The individuals are made up of chromosomes (design vectors) which consists of a random set of genes (design variables). The population is then evaluated and ranked according to their fitness value (function value). Once all of the fitness values have been calculated, a selection operator is used in order to determine which individuals are to be used for mating, of which the higher ranked individuals have a larger probability of being selected.

Thereafter, crossover occurs which involves randomly selecting parents for mating with a probability to create children. These children share the genes from their parents, where the genes are passed down according to the method used. Once the genes had been crossed over, there is a probability of mutation of the

child's genes where, if mutated, then random changes will occur to the chromosome. Subsequently, the new child population will then undergo evaluation and the fitness values ranked.

In order for high fitness value individuals not to be lost during mating, elitism is applied which entails replacing the worst-ranked individuals in the child population with the best-ranked individuals from the parent generation. Choosing the number of elites should be done carefully, as too many can drive the search to a local minimum. Once elitism has been applied the child population becomes the parent population and the stopping criteria is checked. If it is met, the optimisation is terminated and the results are reported. If not, the optimisation loop starts again at the beginning of the genetic operators.

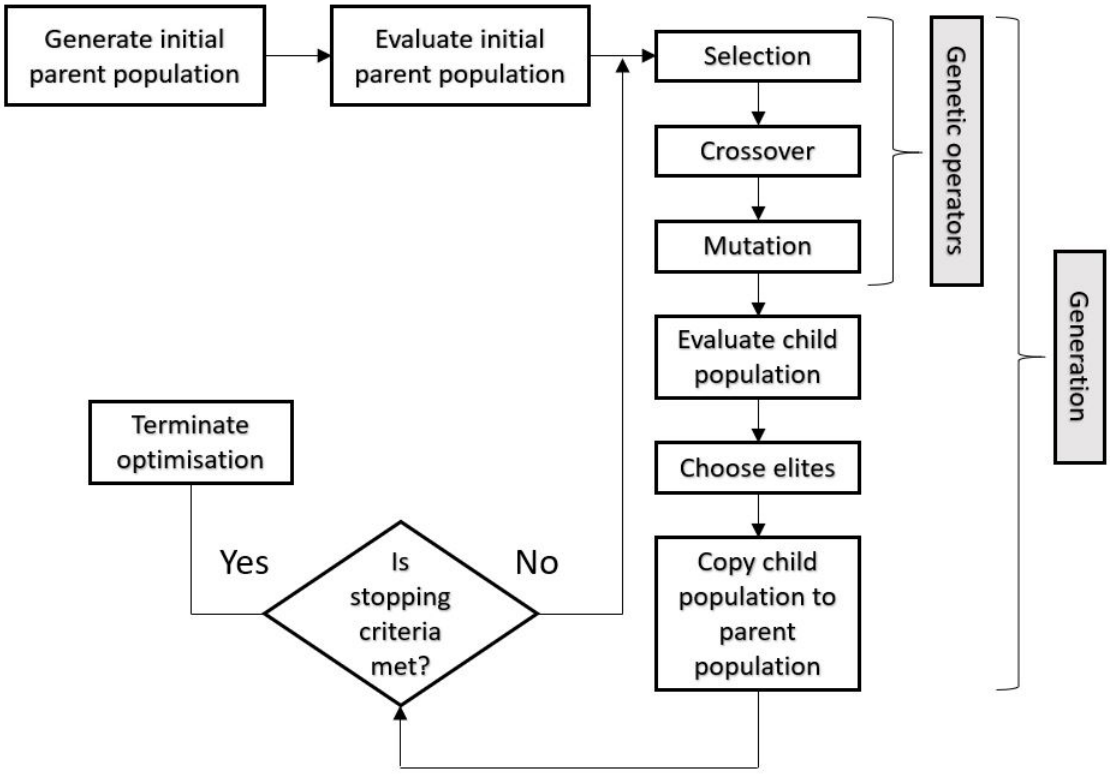

Figure 3.10: Optimisation loop of the genetic algorithm utilised in LS-OPT

3.10 Error Measures

In this research the error occurring between two sets of data was often measured, using different error measures depending on the situation. This section contains the error measures used in this research and a description of each of them.

3.10.1 Root Mean Squared Error

The first measure of error is the root mean square error (RMSE) that represents the standard deviation of the errors between two, equal sized data sets. The definition for the error measure can be found in Equation 3.8:

$$RMSE = \sqrt{\frac{\sum_{i=1}^{n}(y_i - \hat{y}_i)^2}{n}}, \tag{3.8}$$

where y_i and $\hat{y}_i$ are the actual and predicted responses respectively and n is the number of design points. One of the advantages of the RMSE is that the RMSE values for data sets of different sizes can be compared as the sum of squares in Equation 3.8 is averaged.

3.10.2 Hausdorff Distance

The second of the error measures is the Hausdorff distance which is the maximum distance of a set to the nearest point in the other set (Agarwal, 2007). For example, if comparing sets A and B then the Hausdorff distance would be:

$$\delta_H(A, B) = \underset{a \in A}{max}\{\underset{b \in B}{min}\{||a - b||\}\} \tag{3.9}$$

The fact that $\delta_H(A, B)$ does not equal $\delta_H(B, A)$ needs to be taken into account when calculating the Hausdorff distance. Both instances thus need to be calculated and the largest value used. Unlike the RMSE, the Hausdorff distance does not require the two data sets to be of the same size nor does it have to have only one unique y value for every x value. Even though the Hausdorff distance is more robust than the RMSE, the computational power demands are higher and therefore it should only be used when necessary. A visual representation of the Hausdorff distance between two sets can be seen in Figure 3.11.

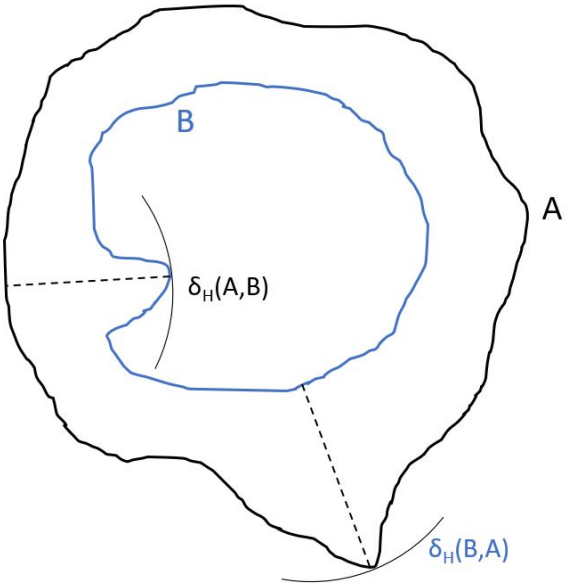

Figure 3.11: Visual representation of the Hausdorff distance from set A to B as well as from B to A represented as δ_H(A,B) and δ_H(B,A) respectively

3.10.3 Metamodel Validation

A popular validation technique for metamodels, which was used in this research, is cross-validation. The leave-out-one cross-validation consists of building multiple metamodels, but each time a different design point is omitted. The predicted value for each design point would therefore be its value on the metamodel built without that specific design point.

There are many different methods for measuring the accuracy of metamodels. However, only one measure, coefficient of determination (R^2), shall be used. The R^2 value is a measure of how well a model is able to capture the variability in a dataset for which $R^2 \in [0, 1]$, where 1 indicates a perfect fit. The coefficient of determination is defined as follows:

$$R^2 = \frac{\sum_{i=1}^{n}(\hat{y}_i - \bar{y})^2}{\sum_{i=1}^{n}(y_i - \bar{y})^2}, \tag{3.10}$$

where $\bar{y}$ is the mean actual value.

Chapter 4

Shape Validation of the Finite Element Model

4.1 Development of the Finite Element Model

In order to determine whether the inflated shape of a physical inflatable wing could be predicted using a numerical model, preliminary tests were performed on simplified models. These tests entailed constructing and inflating numerical models of single cavity inflatable bags. Their inflated geometries would then be compared to that of their corresponding physical models to validate the numerical model. Only the FE model for the shape validation of the single cavity bag will be detailed within, whereas adaptations to this model for different applications shall be detailed in Section 6.1.

4.1.1 Material and Element Properties

From literature and the tests performed on the LDPE in Subsection 3.1.1, material properties for the numerical model could be derived. These properties can be seen in Table 4.1.

Table 4.1: Material properties of the low density polyethylene film used in the FE model

Property	LDPE film
Material model	Linear elastic
Thickness	85 μm
Elastic modulus	0.24 GPa
Poisson's ratio	0.4
Density*	1.8×10^7 kg/m^3

*The concept of mass scaling, discussed in Section 3.6, is the reason for the high density of the LDPE film. This specific density was chosen as if it were increased more, then it would not further decrease the simulation times due to the element size being the constraining factor.

To simplify the FE model material, the strains occurring in the material would be restricted to the linear region by limiting the magnitude of the applied loads. Therefore, the stresses occurring in the material could not exceed 5 MPa. Since the stiffnesses of the LDPE in the two principle directions were very similar in the linear region, it was decided to make the material model a linear elastic isotropic model as opposed to a linear elastic orthotropic model.

Since the Poisson's ratio varies between 0.3 and 0.5, it was decided to test its influence on the inflated shape when performing the analysis. However, the value of 0.4 was given as a starting point for the iterative method. Due to the LDPE film being very thin and not being able to support a bending load, fully integrated membrane elements were chosen to represent the inflatable bag. The shear factor that scales the transverse shear stress was also changed to 0.83 as it suggested for isotropic materials by Hallquist (1986).

4.1.2 Bag Inflation

As discussed in Section 2.1, two different inflation models have been used in the past for FE models of inflatable structures, a pressure load applied to the elements and an airbag model, which applies an air mass to a closed volume and treats the air as an ideal gas. The airbag model has no advantage over the pressure model in terms of modelling the inflated shape of structures; however, it can model the stiffness of the inflated structure when deformed more accurately. The stiffness of the inflated model is not of immediate concern; however, being able to accurately predict the deformation of the inflated structure due

to a load could be useful if the model's applications were to be extended. For this reason, the airbag model was chosen.

In order for the airbag model to function correctly, it requires the structure to have a closed volume with the shell normals pointing outwards. Due to the model requiring a closed volume, a full model had to be used instead of a model that uses symmetry. The mass inside the bag is controlled by a mass flow rate vs. time curve, this curve can be seen in Figure 4.1. Instead of altering the load curve each time to change the internal pressure of the model, the scale factor of the ordinate (SFO) was parametrised.

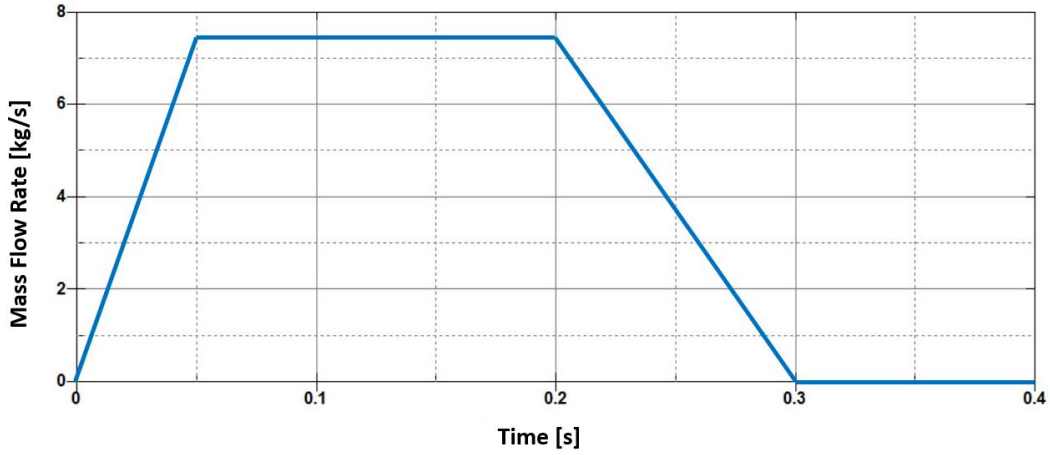

Figure 4.1: Load curve for the mass flow of air into the inflatable bag

4.1.3 Control

In order to maintain accurate and stable simulations, measures were taken by activating certain features. Dynamic Relaxation, as discussed in Section 3.5, was used in the transient phase of the simulation, in conjunction with a global damping of the system to attenuate the oscillations in the simulation. Due to the additional mass from the mass scaling, there was a large amount of inertia in the system which caused the transient phase to exhibit unrealistic responses. Therefore, the simulation was run until the kinetic energy in the system was zero and then those results were extracted.

4.2 Shape Validation

As discussed in Section 3.2, a 3D scanner was used to capture the geometry of the inflated structures to validate the inflated shape of the numerical models. For the shape validation of the single cavity bags, three different sized bags were tested. These bags were 50, 75 and 100 mm in diameter, each with a

length of 600 mm. The shape validation tests were performed by inflating both the physical and numerical models with no loads, besides the inflation, applied to them and their inflated shapes compared. For the inflation, all of the bags were inflated to the same internal pressure, 5.75 kPa. This pressure was chosen for each of the bags, as it was less than the maximum allowable inflation pressure before the material yields, calculated using Equation 2.1.

4.2.1 Physical Tests

The 3D scanner scans the object by projecting a black and white light onto it. However, for the case of clear polyethylene sheets, the light passes straight through it. The light is therefore not reflected and cannot be captured by the cameras. In order to amend this, a white penetrant developer was sprayed onto the bag which dried quickly and left behind a white powder residue. Since the solution evaporated in a few seconds, it was not in contact with the material long enough to soften the material. This white residue allowed the projected pattern to be reflected off the bag and the image captured with the camera.

Once the geometry of the bags were scanned and saved to an STL file, the bags' coordinates were extracted. The STL files are made up of triangular meshes, therefore three nodal points exist for each element. In order to reduce the number of points, each element's three nodal coordinates were averaged to a single coordinate in the center of the element.

4.2.2 Numerical Tests

Once the numerical simulation of the bag inflation had terminated, the nodal coordinates of the model at its final time step were extracted. The file that contained this data is the `nodout` file.

The inflated shape of the numerical model was symmetric about all three Cartesian planes; however, this was not the case for the physical model which was orientated in an arbitrary position. The physical model was rotated and translated about the x, y and z axes in order to align its geometry with the numerical models. The alignment was performed by means of rigid body transformations where the rotation matrices about the x, y and z axes can be found in Equations 4.1 to 4.3:

$$R_x = \begin{bmatrix} 1 & 0 & 0 \\ 0 & cos(A) & -sin(A) \\ 0 & sin(A) & cos(A) \end{bmatrix}, \tag{4.1}$$

$$R_y = \begin{bmatrix} cos(B) & 0 & sin(B) \\ 0 & 1 & 0 \\ -sin(B) & 0 & cos(B) \end{bmatrix}, \tag{4.2}$$

$$R_z = \begin{bmatrix} cos(C) & -sin(C) & 0 \\ sin(C) & cos(C) & 0 \\ 0 & 0 & 1 \end{bmatrix}, \tag{4.3}$$

where A, B and C are the angles of rotation about the x, y and z axes respectively.

The three rotation matrices were multiplied together in order to form a single rotation matrix, which was then used to multiply with an untransformed coordinate matrix to form a $3\times n$ transformed coordinate matrix. The rows of the transformed coordinate matrix consisted of the x, y and z coordinates respectively and n being the number of coordinates for the bag. Once the bag was rotated, the coordinates of the bag were translated about the three axes.

In order to visualise the shape of the inflatable bags, 2D plots were created for the points near each of the symmetry planes ($\leq$ 2.5 mm on either side of the symmetry plane). This created an outline of the bag shape near each of the symmetry planes. The nodal coordinates were initially transformed by eye. This was an iterative process which entailed manually transforming the coordinates of the physical point cloud to match the numerical model's point cloud for the best fit.

Once it was thought that the models were manually aligned as best as they could be, a metamodel based optimisation was performed in order to minimise the sum of the Hausdorff distances between the two point clouds for each of the symmetry plane plots. This optimisation used an RBF as the metamodel and an optimiser that used a GA initially to search for the global minimum and then switched to an LFOP to search for the local minimum. The optimisation entailed parametrising the rotation angles about the three axes as well as the translations along the three axes. The optimisation was performed until the difference between the successive Hausdorff distances was less than 0.01 mm.

4.2.3 Point Cloud Comparison

A mesh convergence study was performed on the numerical models in order to determine a suitable mesh size. The model chosen for the study was the 50 mm diameter bag as the mesh would affect its accuracy the most. The study entailed comparing the effect of the mesh size on the Hausdorff distance between the two point clouds with the physical model in its optimised orientation. The size of the model's elements were initially 10 mm and then halved in size until the sum of the Hausdorff distances of the three profiles converged. The results of the mesh convergence study can be seen in Figure 4.2 in the form of an element length vs. Hausdorff distance plot.

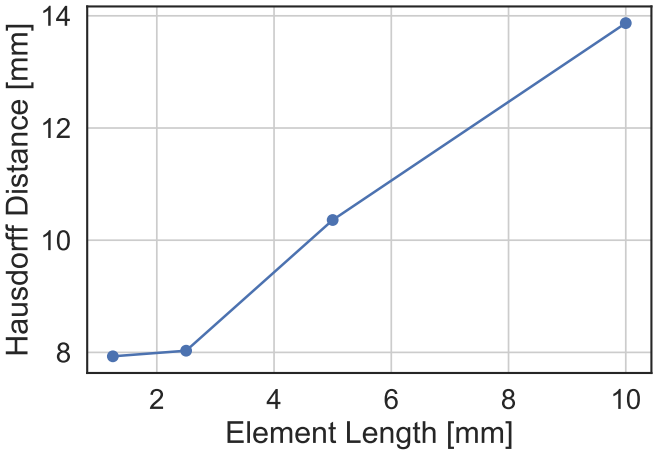

Figure 4.2: A plot displaying the element length vs. Hausdorff distance from the mesh convergence study

From the results of the mesh convergence study, an element size of 2.5 mm was chosen for the remainder of the models due to the small change in Hausdorff distance when decreasing the element size to 1.25 mm. By halving the element size to 1.25 mm, the number of elements quadrupled. Therefore, it would not have made the utilisation of such small elements feasible, due to the large increase in simulation times for a small accuracy gain.

Just as the influence of the mesh density on the model's inflated shape was tested, different Poisson's ratios were used to determine their effect on the inflated shape. The 50 mm diameter model was once again used and the three different Poisson's ratios tested: 0.3, 0.4 and 0.49 (0.5 was not tested as it caused an error in LS-DYNA). The results for the different Poisson's ratios using the 2.5 mm mesh can be seen in Table 4.2.

Table 4.2: The influence of the Poisson's ratio on the Hausdorff distance between the numerical and physical point clouds for a 50 mm model

Poisson's ratio	Hausdorff distance [mm]
0.3	8.07
0.4	8.03
0.49	8.04

Changing the Poisson's ratio had a small influence on the Hausdorff distances between the two data sets as seen in Table 4.2. However, the ratio of 0.4 did produce the smallest Hausdorff distance, even if it was only by a small difference, and therefore it was chosen for the remaining models. The inflated shape of the 75 mm bag using the finalised material properties and an element size of 2.5 mm can be seen in Figure 4.3.

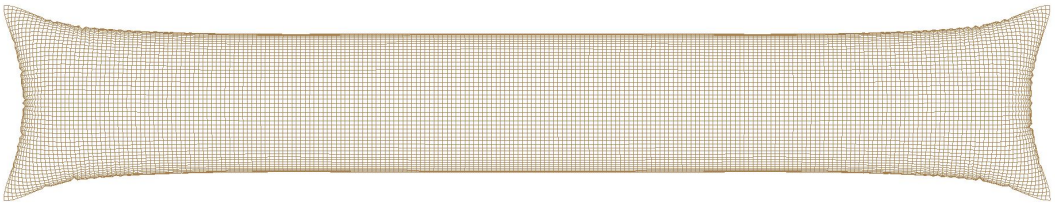

Figure 4.3: Inflated diameter 75 mm bag with 2.5 mm quad elements

A breakdown of the Hausdorff distances of the different symmetry plane plots for the different sized models can be found in Table 4.3. The plot of the points of the physical and numerical models lying near the three symmetry planes for the 75 mm diameter single cavity model can be found in Figure 4.4. The plots comparing the 50 and 100 mm diameter bags can be found in Appendix B.

Table 4.3: The Hausdorff distances between the physical and numerical point clouds for the different sized models, near their respective symmetry planes

Bag	Plane	Hausdorff [mm]
⌀50	xz	3.30
	yz	2.08
	xy	2.65
⌀75	xz	3.99
	yz	2.3
	xy	5.8
⌀100	xz	5.2
	yz	2.34
	xy	3.7

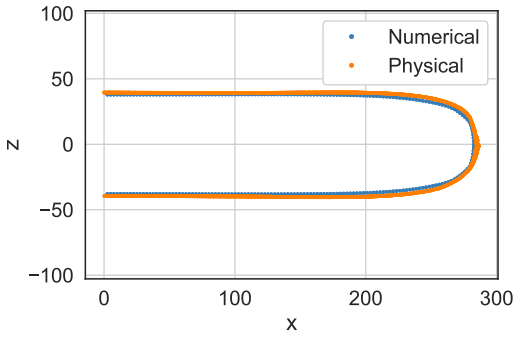

(a) On the xz plane

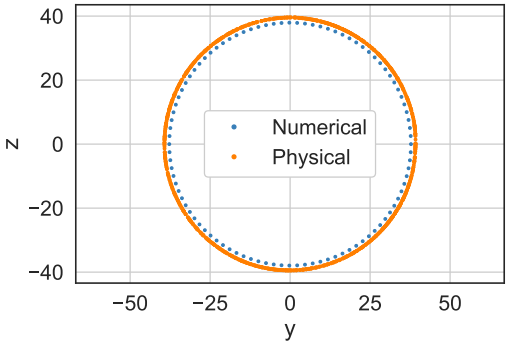

(b) On the yz plane

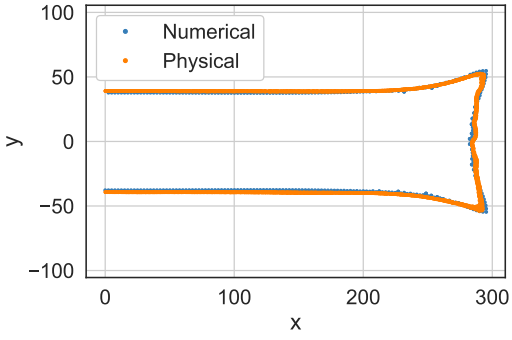

(c) On the xy plane

Figure 4.4: Symmetry plane plots comparing the shape of the numerical and physical model of a 75 mm inflated bag under no load

As seen in Table 4.3, as the model size increases, so does the Hausdorff distances. This was true except for the plots on the xy plane, as there was a large increase from the 50 to 75 mm bag and then it decreased again at the 100 mm bag. This large value for the 75 mm bag at first seems out of place; however, when looking at the graph in Figure 4.4c, the shapes of the curves are found to be very similar and if the numerical curve were shifted to the left the error would be smaller. Shifting the numerical model to the left, however, would increase the error in the xz plane. This is what was most probably done by the optimizer for the 100 mm bag and thus would explain the large difference between the errors for the 100 and 75 mm bags, compared to the 75 and 50 mm bags.

Even though the Hausdorff distances increased with the model size, the increase was not linearly proportional to the scaling of the model. This meant that the accuracy is not lost when using larger models and that they are able to produce results as accurate as the smaller models. Upon viewing the inflated profiles compared in Figure 4.4, for the 75 mm bag as well as the plots for the 50 and 100 mm bag, the physical models all seem to be slightly more inflated than the numerical model. This could be attributed to the numerical model being slightly more stiff than the physical model. Deviations in the models near the ends of the bag could also be attributed to the material properties being altered during heat welding.

4.3 Summary

The simulated inflated shapes of the numerical models proposed in this chapter produced accurate results when compared to the inflated profiles of the scanned physical models, inflated to the same pressure. The inflated profile of the numerical model on the yz plane produced the best fit for all of the different sized models. The small error of the fit of this profile is very positive, as the profile on this plane is the profile that will be used for the shape optimisation.

The Hausdorff distances between the profiles on the xy and xz plane produce results slightly larger than those on the yz plane. A potential reason for this could be due to the heat sealing of the ends of the bag. The heat sealing melts the material and in turn, could possibly change its mechanical properties. The small error of the fit of the yz profile is good, as the profile on this plane is the profile that will be used for the shape optimisation. Therefore, due to the small errors between the physical and the numerical model's inflated shape, the shape validation of the numerical model can be seen as successful.

Chapter 5

Shape Optimisation

5.1 Optimisation Problem

The methodology proposed in this research aims to solve an inverse problem. This inverse problem entails determining the uninflated shape for an inflatable aerofoil, which has an inflated profile that fits a target aerofoil profile. From the uninflated shape, the dimensions could be used to construct a physical model. Numerical shape optimisation was proposed as a solution to this dilemma due to the non-trivial complexities associated with predicting the inflated shape.

The numerical shape optimisation entailed constructing multiple FE models with a varying number of single cavity inflatable bags, connected to one another. The models were inflated and the profiles compared to that of a prescribed target aerofoil shape. To compare the target and numerical profiles, the chord length of the numerical model was set to the distance from the beginning of the first bag to the end of the last bag.

Another means of comparison that could have been used would entail the end of the last bag not lining up with the trailing edge of the target profile. This would allow a rigid trailing edge to be connected to the inflated model for the remainder of the aerofoil. However, it was previously established that the trailing edge would be made up of the inflation cavities. A comparison of these two chord lengths can be seen in Figure 5.1.

In order to change the inflated shape of the model, the shape of the pre-inflated model required changing. The initial pre-inflated shape of each model consisted of square prisms with parametrised lines on the corners of the squares along the span. These parametrised lines can be seen in Figure 5.2 for a model made up of three cavities in the form of thick black lines with the black dots representing the ends of the lines.

(a) Chord length of inflated numerical model equal to that of the target profile (adapted from Simpson (2008))

(b) Chord length of inflated numerica model less than that of the target profile (adapted from Simpson (2008))

Figure 5.1: Two different methods for comparing the chord lengths of the inflated numerical model and the target profile

These thick black lines' coordinates were parametrised in the x and z direction, as only the profile of the wings were matched. The aerofoil used as the target aerofoil was the NACA 0030, for the reasons mentioned in Section 2.3. A symmetric aerofoil was used as the lines on the top and bottom could use the same parameter, due to the NACA 0030 aerofoil profile being symmetric over the xy plane. This halved the number of parameters required which was beneficial in terms of computational cost for simulations with a larger number of cavities.

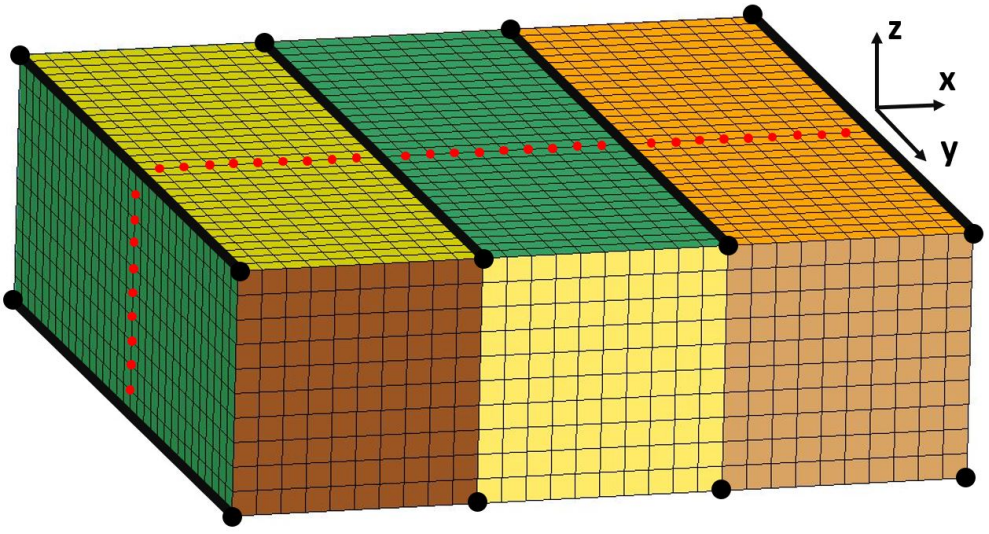

Figure 5.2: The pre-optimisation deflated shape of the numerical model of a three cavity inflatable wing

Once the cavities were inflated, a set of nodes half way down the span and around the entire surface of the wing was extracted, see red nodes in Figure 5.2. The profile of the inflated models near the root and tip were found to be affected due to the end effects. Therefore, the span of the model was created in order for the extracted nodes not to be affected by the end effects, but were also kept compact enough to limit the simulation times. The formulation of the optimisation problem can be formulated as follows:

$$
\begin{aligned}
\min \quad & f(\mathbf{x},\mathbf{z}) = \sqrt{\frac{\sum_{i=1}^{n}(z_i^* - \hat{z}_i^*)^2}{n}}, \\
\text{subject to} \quad & 0.5(3x_1 - x_2) + \varepsilon \leq x_1 \leq 0.5(x_1 + x_2) - \varepsilon, \\
& 0.5(x_{i-1} + x_i) + \varepsilon \leq x_i \leq 0.5(x_{i+1} + x_i) - \varepsilon, i = 2, \ldots, k-1, \\
& 0.5(x_{k-1} + x_k) + \varepsilon \leq x_k \leq 0.5(3x_k - x_{k-1}), \\
& \varepsilon \leq z_i \leq 0.5(t)(\max(x_k) - \min(x_1)), i = 1 \ldots k.
\end{aligned} \tag{5.1}
$$

The objective function, $f(\mathbf{x},\mathbf{z})$, represents the RMSE between the positive z nodal coordinates of the inflated numerical model and the NACA 0030 aerofoil profile at the corresponding x coordinates. These values are represented as $\mathbf{z}^*$ and $\hat{\mathbf{z}}^*$ respectively, and n the number of coordinates compared. In order to compare the two profiles, the numerical models' dimensions needed to be scaled so that $x \in [0,1]$ with the z coordinates scaled proportionally. A direct comparison of the numerical models' fits was possible due to the chord lengths scaled to the same range.

The reason for using the RMSE as the error measure was due to the sum of the squared error being divided by the number of points before it is square rooted. This averaging of the sum of squared error allows the errors of profiles consisting of an inconsistent number of nodes to be compared fairly.

In Equation 5.1, $\mathbf{x}$ and $\mathbf{z}$ represent the x and z vectors respectively of the nodal coordinates for the parametrised lines of the model in the uninflated shape. The number of parameters in these vectors are represented by k, and i representing an index in between 1 and the maximum. The values in $\mathbf{x}$ were constrained in such a way that the upper and lower bounds are an element's length less of half the distance between its initial adjacent points. For the values in $\mathbf{z}$, the maximum value was constrained to be half the thickness of the NACA 0030 aerofoil when scaled to the ideal aerofoil (t representing the aerofoil thickness), using the largest possible chord length. The minimum value was set at an element's length away from the symmetry plane.

The value for ε in Equation 5.1 represents the length of the elements in the model. This is portrayed in a visual representation of the parameter constraints that can be seen in Figure 5.3 for the three cavity model shown in Figure 5.2. The red dots and lines in the figure represent the parametrised lines along the y axis and the upper and lower bounds for each of the parameters respectively.

This optimisation formulation was used for the shape optimisation of three, eight and fifteen inflatable cavity wings. This was done to observe the quality of fit of the inflatable wings with varying the number of cavities. When increasing the number of cavities used for the model, the sizes of each of the cavities were

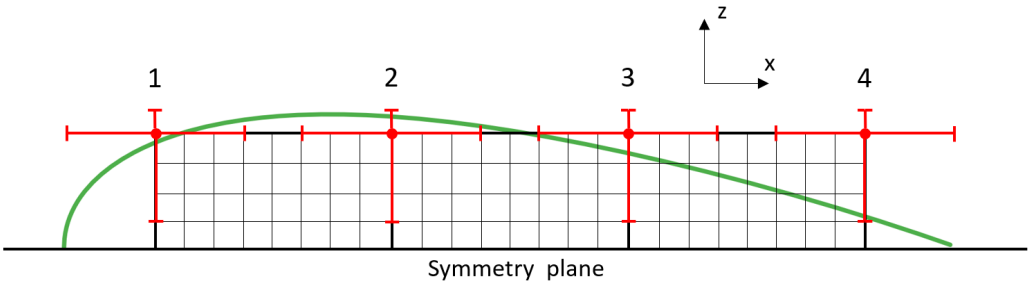

Figure 5.3: A visual representation of the parameter constraints of the pre-inflated three cavity model

kept constant. The chord length of the models therefore increased as the number of cavities increased. This was done to conserve the resolution of the cavities in the numerical model, in order to maintain the accuracy of the final shape.

An airbag inflation model was used to apply the inflation pressure to the model due to the airbag model's ability to more accurately simulate the inflated stiffness of the structure under deformation, as discussed in Chapter 2. Even though an accurate inflated stiffness is not required for shape prediction, if the use of the model were to be extended to deflection prediction under a loading, then it would be important.

Inflation pressures were applied to each of the cavities separately, with each one having a closed volume. Throughout the shape optimisation simulations, the air masses inside the cavities were kept constant with a mass that would pressurise the bags to a sufficient pressure (a pressure at least a 1 kPa above the ambient pressure) no matter the size. This was done as it was assumed that the inclusion of the mass parameters would increase the computational time without significantly improving the accuracy.

LS-PrePost was used for the construction of the numerical models and LS-DYNA was used to perform the FE analysis. The role of these programs in the numerical shape optimisation can be seen in the optimisation pipeline in Figure 5.4. Metamodel-based optimisation was used to take advantage of metamodelling's ability to reduce simulation times and achieve accurate results, provided the correct configuration was used. Domain reduction was also used and decreased the range of the parameters after every iteration in order to narrow the search for the minimum.

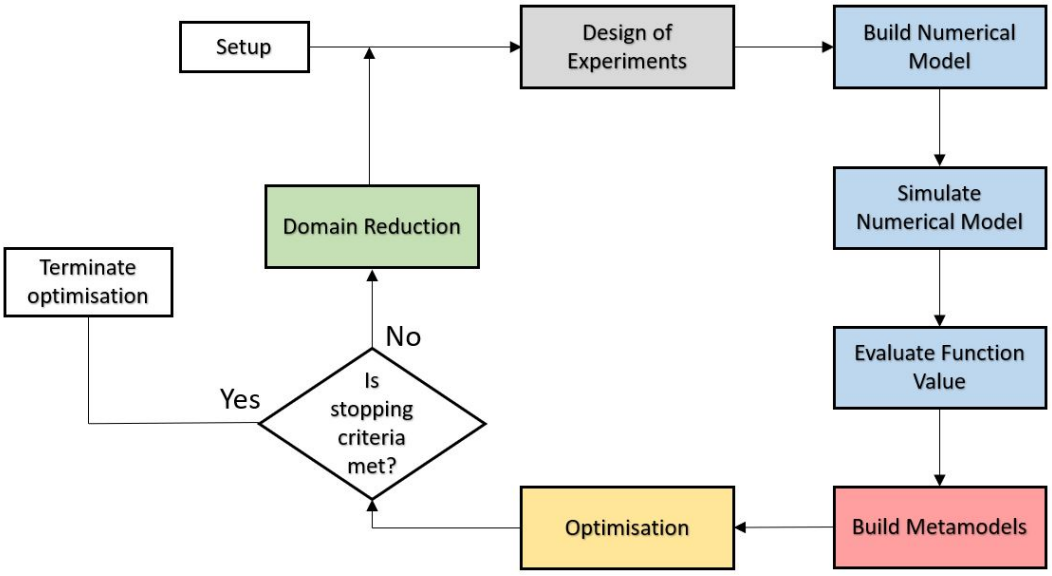

Figure 5.4: The optimisation pipeline for the shape optimisation performed on the three, eight and fifteen cavity wings

5.2 Finite Element Model Construction

The numerical model's shape is required to change in order to fit the target aerofoil profile; therefore, a new numerical model of the inflatable wing was created for every design point. This was done by executing a macro in LS-PrePost. This would create a model similar to that in Figure 5.2, but with the coordinates of the parametrised lines updated for each design point. The model was built every time instead of an initial model geometry being morphed so that the mesh would not deform; which could make the solution unstable and inaccurate.

The material properties for polyethylene found in Section 4.1 were once again used for the model. Two different fully integrated membrane elements were applied to the model. The outer elements had a thickness of 85 μm and the elements representing the spar had a thickness of 42.5 μm. The spars consisted of two equally sized parts placed in the same position therefore representing a single full-thickness spar. This was done in order for the airbag model to work correctly, as the element's normals were required to point outwards from the closed volume. With just a single part in between each cavity, the normals would point inwards for one of the cavities.

Once created, some of the parts' normals were not orientated in the correct direction and therefore, in the macro file, the orientation of the incorrectly aligned normals were reversed. The model was checked for duplicate nodes and the nodes merged in order to connect the adjacent parts. The node-set

for extraction post-simulation, seen in Figure 5.2, was created; along with the different part sets to be used for the definition of the airbag inflation of the cavities. At the end of the macro file, the model was saved to a temporary keyword file. This file contained the model data specific to each design point and would be used in the simulation of the model.

LS-OPT has the option of setting up a stage (blue shaded blocks in Figure 5.4) to utilise LS-PrePost directly. However, for this instance, it did not work in Microsoft Windows 10, as it created incomplete keyword files. The problem was thought to be that the model-building stage was terminated before the model was built, and not due to the deformity of the model. This was tested and the geometries that failed to build through LS-OPT built successfully when executing the macro directly through the LS-PrePost program.

To test whether the premature termination was the issue, the stage at which the numerical model was built was specified to execute a user-defined program instead of LS-PrePost. The user-defined program used was Python, which executed the macro file with LS-PrePost. This fixed the issue.

5.3 Model Simulation and Function Value Evaluation

As previously mentioned, the temporary keyword file contained the model data for each specific design point. The remaining data, that was kept constant throughout the design process, was stored in a main keyword file. The main keyword file contained the following information: the termination time, the global damping, the mass flow curves, the database output requests, the airbag model and the material and element properties. The main keyword file for a three inflation cavity wing can be found in Appendix C.

Upon completion of the numerical model's simulation, a binary `nodout` file was extracted to retrieve the nodal coordinates of the intended inflated profile at the final timestep. The binary file was outputted, as LS-DYNA only creates this data as binary files.

Unlike ASCII files, which are in a human-readable format, the format of binary files are only readable by the computer. Therefore, it was converted to an ASCII file before the data was extracted. In order to convert the binary file, an executable that is available with the LS-DYNA build, `l2a.exe`, was used. This executable was run through Python in the final stage ("Evaluate Function Value" in Figure 5.4). In the same Python script, the function value was computed once the file had been converted and the nodal coordinates extracted.

Multiple combinations of metamodels and optimisers were tested on the three cavity model in order to determine the best configuration. The results from these tests can be found in Appendix D. The configuration that was chosen for the remaining simulations consisted of an RBF metamodel, using an optimiser that used a GA to search for the global minimum then switched to an LFOP to search for the local minimum. The RBF used a Gaussian distribution and was constructed from the design points only from that iteration. This configuration was chosen, as it yielded the smallest objective function value, as well as producing consistently accurate metamodels.

The termination criteria for the optimisation was set so that it would terminate if the change in the objective function value between two successive iterations was less than 10^{-3}. The termination criteria imposed on the shape optimisation allowed the model to converge to a profile that resembles that of the target aerofoil profile. However, it could have slightly restricted the convergence of the model to its most optimal shape. For the purpose of this research, the converged answers will suffice. However, if a more accurate fit is required, the tolerance between each iteration's function value can be changed. The convergence plots for each model can be seen in Figure 5.5.

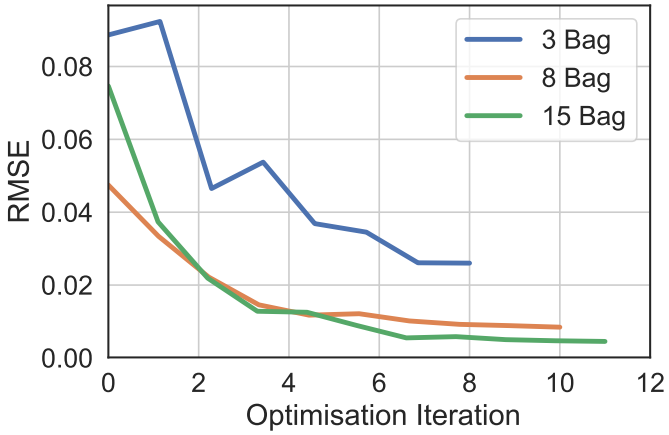

Figure 5.5: Convergence of the shape optimisation for the different sized models

The inflated, shape optimised numerical models for the three, eight and fifteen cavity models can be seen as sectioned views in Figure 5.6. The fits between these inflated numerical profiles and the target aerofoil profile can be better visualised in Figures 5.7 to 5.9. In these plots the inflated numerical model's profile is represented in blue, the target profile in orange and the error between the two profiles represented by a green dashed line. These plots were normalised so that $x \in [0, 1]$, where x represents a coordinate on the chord length. The fit between the two profiles is represented by the R^2 value

displayed above the graph and a plot of the residual error between the two profiles.

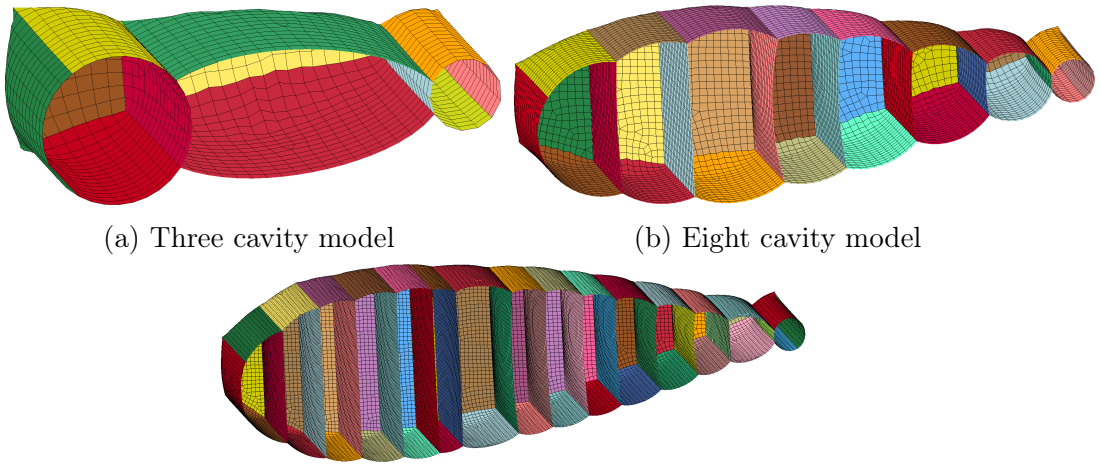

(a) Three cavity model

(b) Eight cavity model

(c) Fifteen cavity model

Figure 5.6: Sectioned views of the inflated, shape optimised numerical models for the three, eight and fifteen cavity models

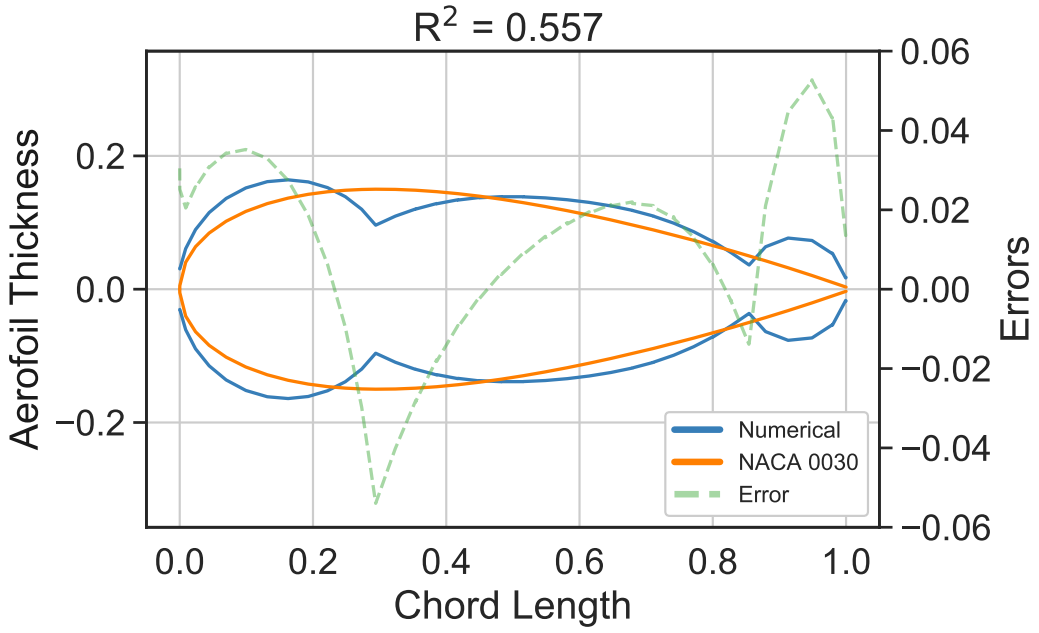

Figure 5.7: Comparison of the three cavity numerical model's inflated profile vs. NACA 0030 aerofoil profile

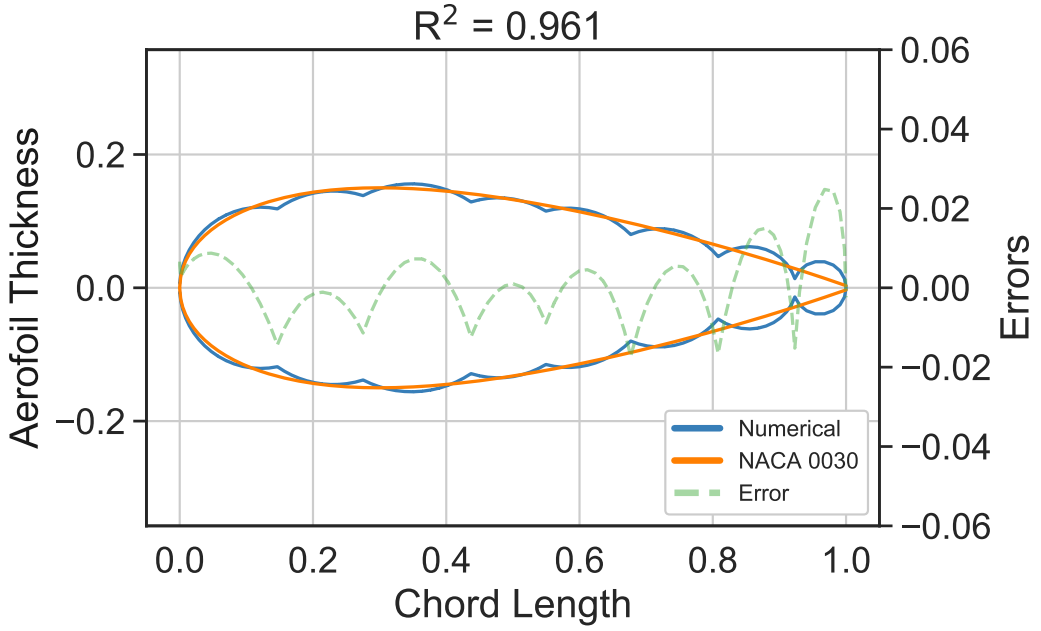

Figure 5.8: Comparison of the eight cavity numerical model's inflated profile vs. NACA 0030 aerofoil profile

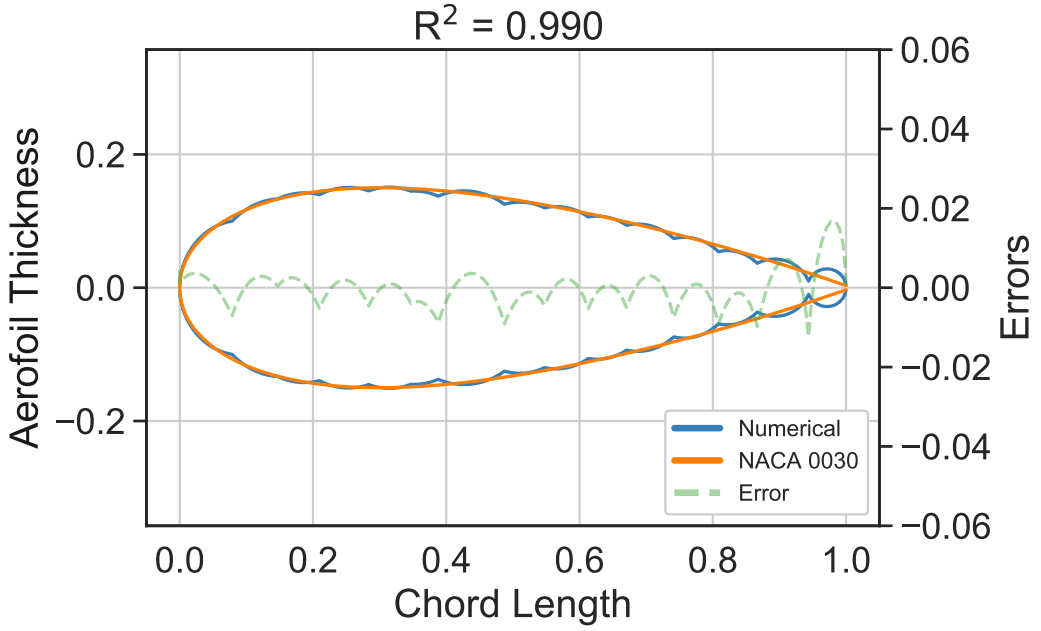

Figure 5.9: Comparison of the fifteen cavity numerical model's inflated profile vs. NACA 0030 aerofoil profile

As the number of cavities used for the models increased, so improved the fit of the numerical model to the target. This is evident upon referring to the

decreasing residuals and the increasing R^2 value. Upon viewing the difference between the R^2 values of the cavities, a larger difference was found between the first two compared to the last two. Therefore, the effect of improving the fit as the number of cavities increased seemed to have a diminishing return.

5.4 Pressure Matching

In order to determine whether the inflated profile can accurately represent its corresponding physical model, the two profiles had to be compared. This entailed constructing a physical model and capturing its geometry once the model had been inflated to a uniform pressure. However, since the inflation model consisted of applying an equal air mass to each of the cavities and each of the cavities differed in volume, the pressures inside the cavities were different. Therefore, another set of optimisations were performed to match all the cavities' pressures in the numerical models so that the profiles of the physical and numerical models could be compared.

From the numerical tests performed on the single cavity numerical models for the shape validation, it was found that when the bags were inflated to pressures higher and lower than the 5.75 kPa there was not a large difference between the inflated profiles. More specifically, it was not distinguishable to the eye. However, as the pressures neared the yield pressure the profile displacements began to be more evident. This was the same for when the pressure neared 1 kPa, where the bag was not sufficiently pressurised.

The pressure used for each of the different sized models was determined using the equation for the hoop stress acting on a thin-walled pressure vessel, Equation 2.1. The σ used, was the yield strength of the polyethylene divided by a safety factor of 1.5. The largest radius of the outer membrane of the model was used as r in the equation, as the material would yield there first. The largest radius of the cavity was calculated, with the circle through three points equation using the nodal coordinate points of the inflated shape optimised model. The formulation of the pressure matching optimisation problem is as follows:

$$\min \quad f(\mathbf{m}) = \sqrt{\frac{\sum_{i=1}^{n}(p_i - \hat{p}_i)^2}{n}}, \tag{5.2}$$

In Equation 5.2, $f(\mathbf{m})$ represents the RMSE of the pressures in the cavities for a model with n cavities. The vector $\mathbf{m}$ represents the vector containing mass scaling factors that control the amount of mass flow into the cavities.

The pressure in the cavities and the target pressure are represented as p and $\hat{p}$ respectively.

The geometry of the shape optimised model was used for each design point for the pressure matching optimisation. This was done as it was assumed that small pressure changes in the cavities would not cause a large change in the inflated profile. The termination criteria was set to terminate once the function value was within 100 Pa of the target pressure. This value was used as it was found that 100 Pa did not make a noticeable difference to the fit of the aerofoil profile.

The pressure matching optimisation results for the eight and fifteen cavity models both converged to within the constraints. Unlike the eight cavity model, the fifteen cavity model was sensitive to the upper and lower limits of the constraints, causing it to settle in local minimums. An iterative approach was therefore followed. This entailed narrowing the limits of the mass scaling factors for each cavity, depending on whether the pressure inside its corresponding cavity was above or below the target pressure.

The change in the pressure for the three cavity model had a large influence on the inflated profile. This is seen from the 103 % increase of the RMSE value from the shape optimised profile to the pressure matched profile. Therefore, in order to maintain a low error fit of the inflated profile to the ideal, a different optimisation formulation was created. This formulation entailed parametrising the x and z coordinates of the features parametrised in the shape optimisation as well as the mass scaling parameters. The optimisation formulation is seen in Equation 5.3:

$$
\begin{aligned}
\min \quad & f(\mathbf{x},\mathbf{z},\mathbf{m}) = \sqrt{\frac{\sum_{i=1}^{n}(z_i^* - \hat{z_i^*})^2}{n}}, \\
\text{subject to} \quad & -100 \text{ Pa} \leq g(\mathbf{x},\mathbf{z},\mathbf{m}) \leq 100 \text{ Pa}, \\
& 0.5(3x_1 - x_2) + \varepsilon \leq x_1 \leq 0.5(x_1 + x_2) - \varepsilon, \\
& 0.5(x_{i-1} + x_i) + \varepsilon \leq x_i \leq 0.5(x_{i+1} + x_i) - \varepsilon, i = 2, \ldots, k-1, \\
& 0.5(x_{k-1} + x_k) + \varepsilon \leq x_k \leq 0.5(3x_k - x_{k-1}), \\
& \varepsilon \leq z_i \leq 0.5(t)(\max(x_k) - \min(x_1)), i = 1 \ldots k.
\end{aligned}
\tag{5.3}
$$

The objective function of the optimisation, $f(\mathbf{x},\mathbf{z},\mathbf{m})$, was the RMSE value between the inflated profile of the numerical model and the ideal profile. The RMSE of the pressures, $g(\mathbf{x},\mathbf{z},\mathbf{m})$, was constrained in order for it to be within 100 Pa of the specified target pressure. The termination criteria for the optimisation was set to terminate the optimisation once the difference between

the successive optimised RMSE value was less than 10^{-3}.

The pressure matching optimisations were performed on all three models with the eight and fifteen cavity models making use of the formulation in Equation 5.2 and the three bag model making use of the formulation in Equation 5.3. The pressures for all three of the models converged to within 100 Pa where the R^2 fits between the numerical and target profile for the post-pressure matching optimisation models can be found in Table 5.1. The R^2 fits for the pre-pressure matched models were also included for a comparison.

Table 5.1: The R^2 fits between the three, eight and fifteen cavity models and the target aerofoil profile for both pre- and post-pressure matching

	Three	Eight	Fifteen
Pre-pressure matching	0.557	0.961	0.990
Post-pressure matching	0.557	0.969	0.988

The pressure matching optimisations for the three, eight and fifteen cavity models successfully altered the pressures inside the cavities to within 100 Pa of its target pressure. There was also not a significant change in the R^2 fit between the numerical model's inflated profile and the target profile for the models pre- and post-pressure matching. In future cases, these optimisations should therefore be utilised to acquire the air masses for the shape optimised geometry to take advantage of the airbag model's ability to accurately predict the model's inflated stiffness under load.

5.5 Physical Models of the Inflatable Aerofoils

The design methodology was formulated in such a way that the dimensions of the uninflated profile of an optimised inflatable wing could be measured onto a membrane film, cut out and heat welded together. The construction method would dictate the cut-out pattern used for the wing. In the case of this research, the wing construction consisted of each inflation cavity constructed from an individual sheet. An example of how the sheets for the three cavity physical model from Figure 5.2 were connected is shown in Figure 5.10. The black and red lines in Figure 5.10 represent the film sheets and the places on the sheets that were heat welded together. The red circles in the figure represent the heat welds perpendicular to the view.

The root and tip of the model could not be sealed as they were in the numerical model due to the complexity of the seal and the time required to achieve this.

Instead, each of the cavities' ends were extended separately with the extended sections not welded to another cavity. The extended sections were welded closed along the span as well as at the tip, which was welded into a flat line with the line orientated vertically. The ends were constructed this way so that the straight seal at the ends did not affect the inflated aerofoil profile. Just as the span of the numerical model was chosen so that it was long enough for the end effects not to influence the profile, the same was done for the physical model.

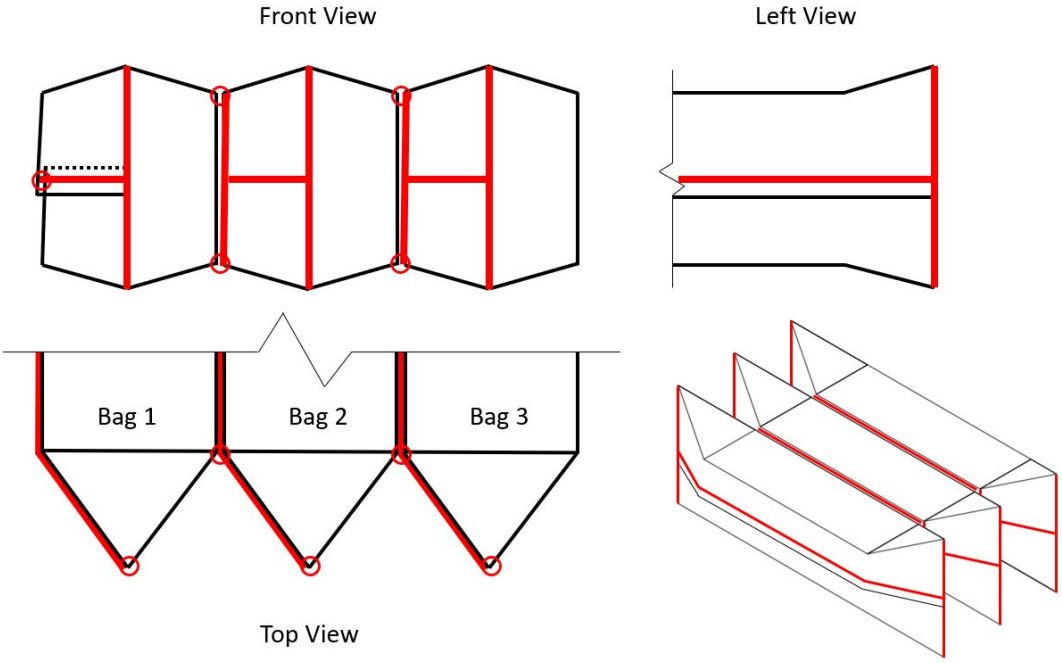

Figure 5.10: An example of the polyethylene sheet cut out for the deflated profile of a three cavity inflatable physical model

As discussed in Section 5.3, the physical model was designed to maintain a constant pressure throughout the model. This entailed applying the air into a single cavity which would inflate the other cavities, by allowing the air to flow through small holes created in the spars. The number of holes created were kept to a minimum to not affect the tensile stiffness of the spar.

A pressure transducer was connected to an inflation cavity on the opposite end of the chord length to the initially inflated cavity. This was done to account for the pressure drop across the cavities due to potential leaks. From the geometry of the uninflated pressure matched numerical models of the three, eight and fifteen cavity wings, physical models were constructed and inflated to their target pressure. The inflated physical model of the fifteen cavity aerofoil can be seen in Figure 5.11 and the Figures E.1 and E.2 for the three and eight cavity aerofoils.

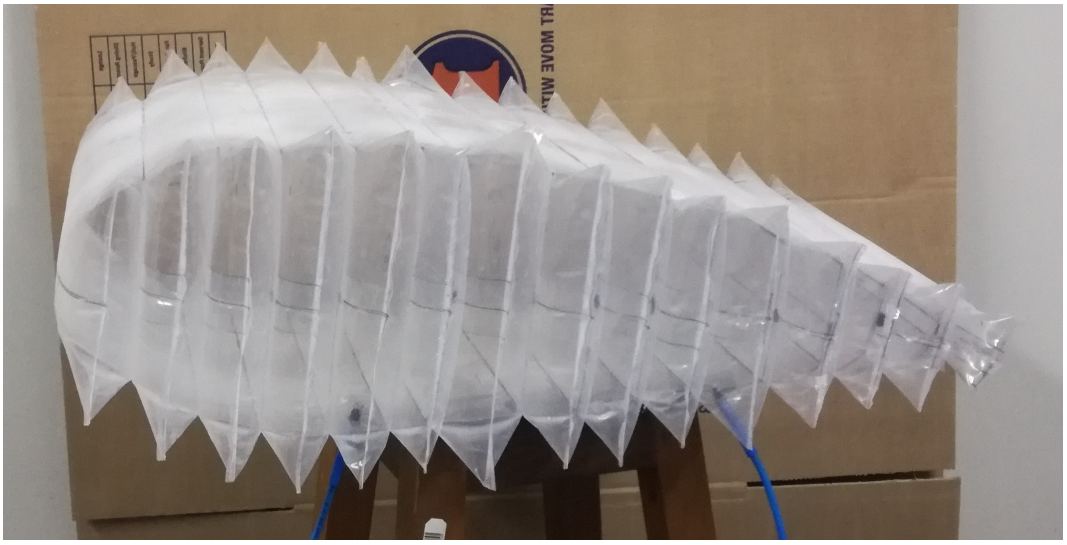

Figure 5.11: The inflated physical model of the fifteen cavity aerofoil

Once the physical models were constructed, the inflated profiles for each of the aerofoils were compared to the inflated numerical models' profiles. This was once again done by 3D scanning the objects. As the 3D scanned objects were positioned in an arbitrary position, the optimisation method discussed in Section 4.2 was applied to the aerofoil point clouds to achieve the fit.

The plots comparing the numerical and physical aerofoils can be seen in Figures 5.12 to 5.14 with the R^2 value displayed representing the fit between the two. Since the numerical model consisted of substantially less points than the physical model, The R^2 value was calculated by linearly-interpolating the numerical model's nodes to match the number of points of the physical model.

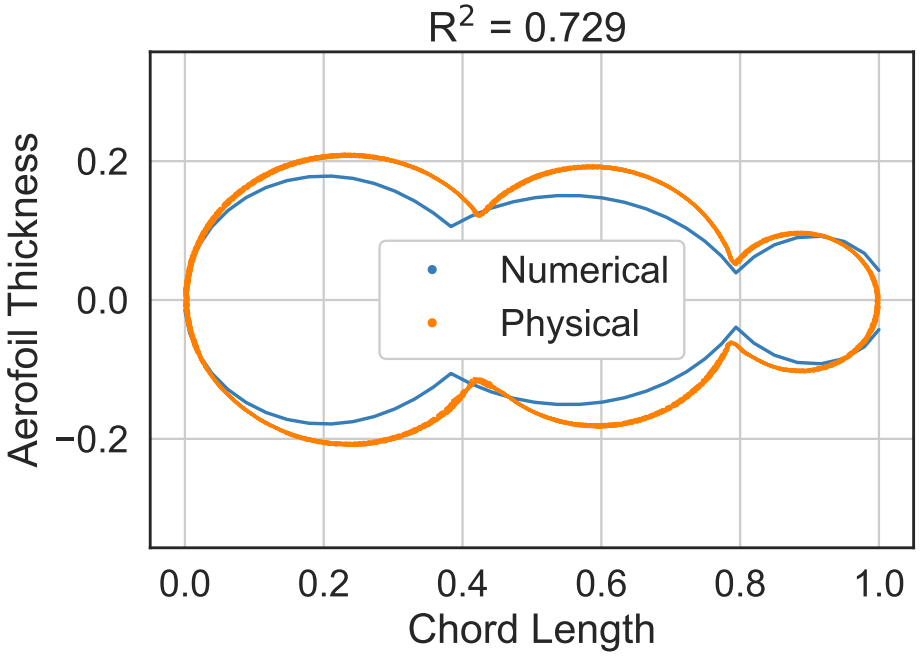

Figure 5.12: Comparison of the inflated profiles of the three cavity numerical and physical models

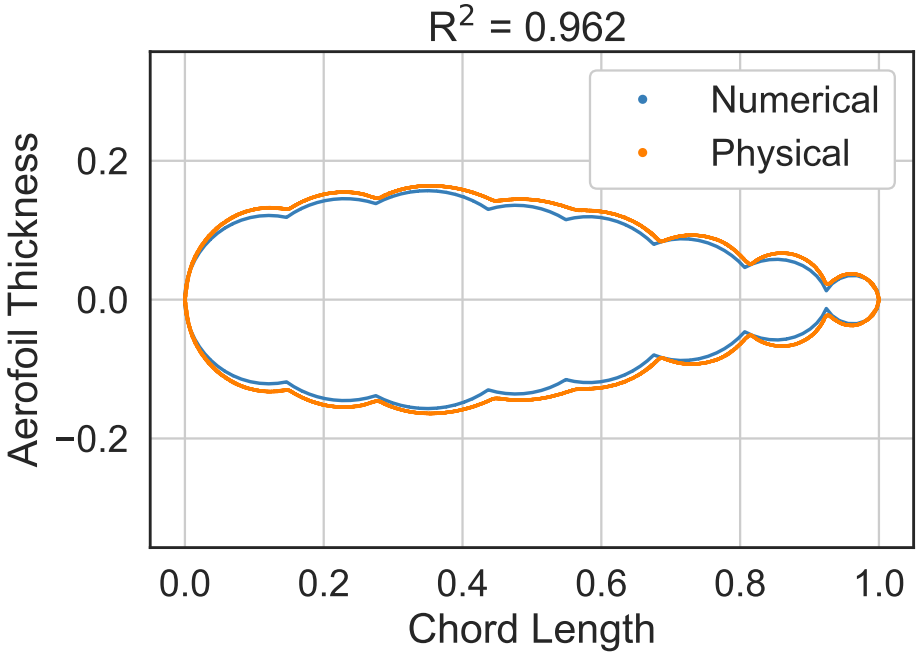

Figure 5.13: Comparison of the inflated profiles of the eight cavity numerical and physical models

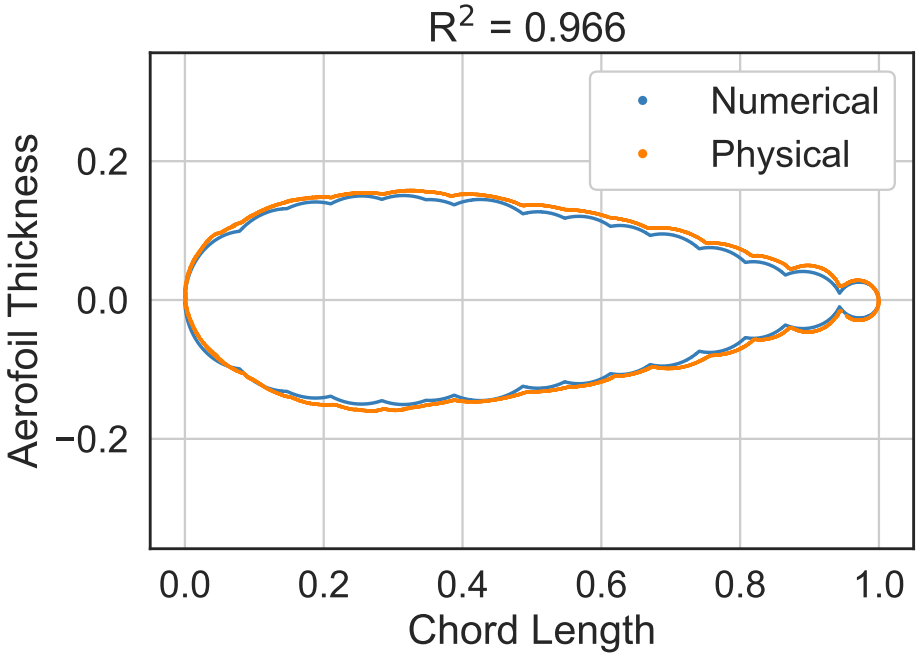

Figure 5.14: Comparison of the inflated profiles of the fifteen cavity numerical and physical models

Upon increasing the number of cavities, the goodness of fit between the numerical and physical profiles improved, with only a slight increase in fit quality between the eight and fifteen cavity models. In Figures 5.12 to 5.14, the inflated profiles of the physical models were found to be more inflated than the numerical models. This was also seen in the validation on the single cavity models and was thought to be because due to the numerical model being stiffer than the physical model.

In order to test this hypothesis, a different construction method was proposed to see whether it was the numerical model causing the discrepancies between the fits or the construction type. The new construction type entailed using a single sheet to represent the outer membrane of the model and the individual baffles heat welded to the outer membrane. The new construction method for the model in Figure 5.2 is shown in Figure 5.15. An eight cavity model using the new construction method was built and can be seen in Figure 5.16.

This new method was simpler than the previous one in terms of the seals at the tips of the wing and the number of welds required. Sealing the wing tips using only the one seal along the chord also created a more practical wing shape. Instead of holes in the baffles, the air is passed through to the other cavities at the wing tips where no baffles are separating the cavities.

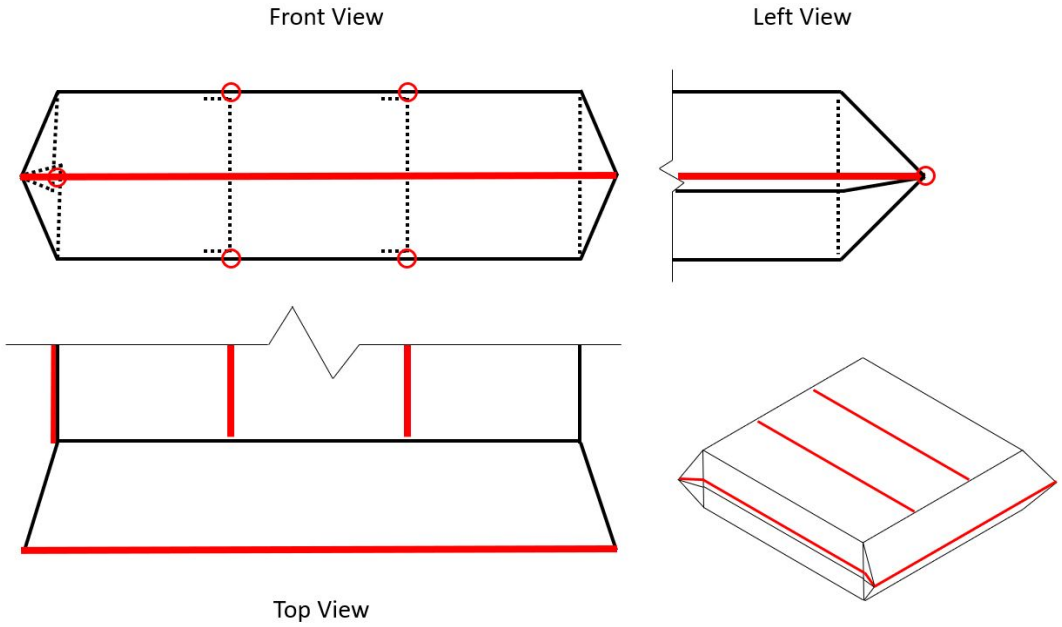

Figure 5.15: An example of the new membrane film cut out for the deflated profile of a three cavity inflatable physical model

Figure 5.16: The inflated physical model of the eight cavity wing using the new construction method

This construction method was initially considered, however, it was not used as it was thought that the heat welds on the surface of the profile would harden the material and affect the inflated profile. The new eight bag model was 3D scanned and upon comparing the inflated profiles, it was found that the seals did not negatively affect the physical model. On the contrary, the fit to the numerical model improved, as seen in Figure 5.17.

The increase in the R^2 value from 0.962 to 0.988 also indicates the improvement of fit when using the new construction method. Referring back to the former method, a possible reason for the over-inflation of the model could have been

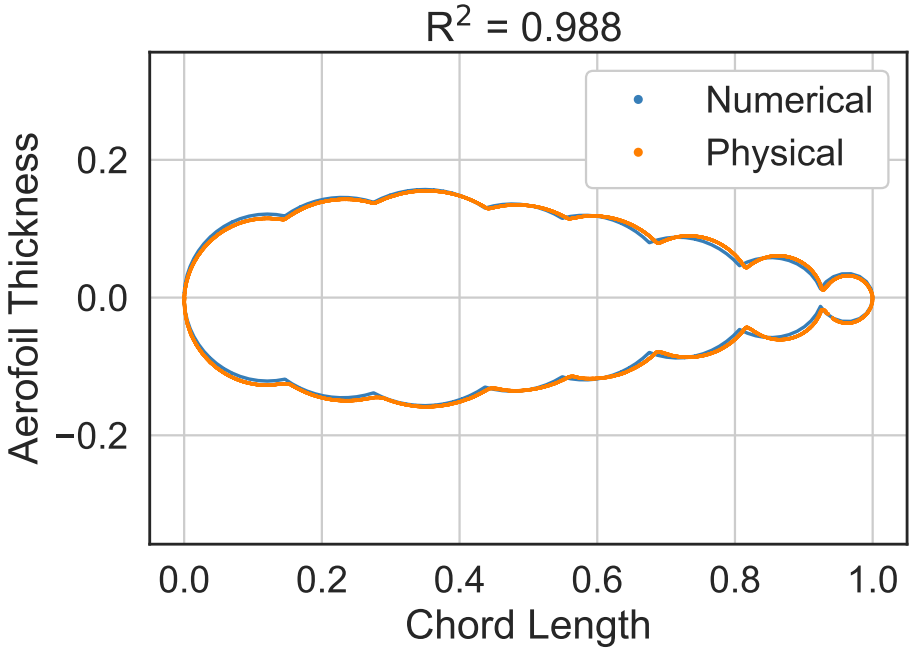

Figure 5.17: Comparison of the inflated profiles of the eight cavity numerical model and the new physical model

attributed to the holes in the baffles decreasing their stiffness. This would thus cause them to elongate more than predicted. The new construction method was simpler as well as more accurate; therefore, it was established as the recommended methodology.

5.6 Robustness of the Design Methodology

Using the NACA 0030 aerofoil profile, the shape optimisation methodology was able to achieve an accurate fit of the inflated numerical model's profile to the target profile. This was the case for the eight and fifteen cavity models, with the three cavity model's fit being significantly lower.

As mentioned in Section 2.3, the NACA 0030 aerofoil provides a good balance between induced drag on the wing and the fit at the trailing edge. However, if the designer wishes to use a thicker or thinner profile, the methodology should be able to fit the numerical model to that profile. To test this, two different aerofoil profiles were used; one thicker and one thinner than the NACA 0030 profile (the NACA 0040 and NACA 0015 respectively). The profiles were limited to symmetric profiles to maintain the relatively low computational cost of the optimisation by keeping the number of variables to a minimum.

The same optimisation formulation used in Section 5.1 was used to fit the

numerical model to the new profiles. Even though using this formulation caused problems in terms of a large deviation between the profile of the pressure matched model compared to the pre-pressure matched model, it was only substantial for the three cavity model. Therefore, using a model with eight or more cavities would not experience this problem. The shape optimisation prior to the pressure matching was therefore performed on an eight bag model where the shape optimised profiles for the two new cases can be seen in Figures 5.18 and 5.19.

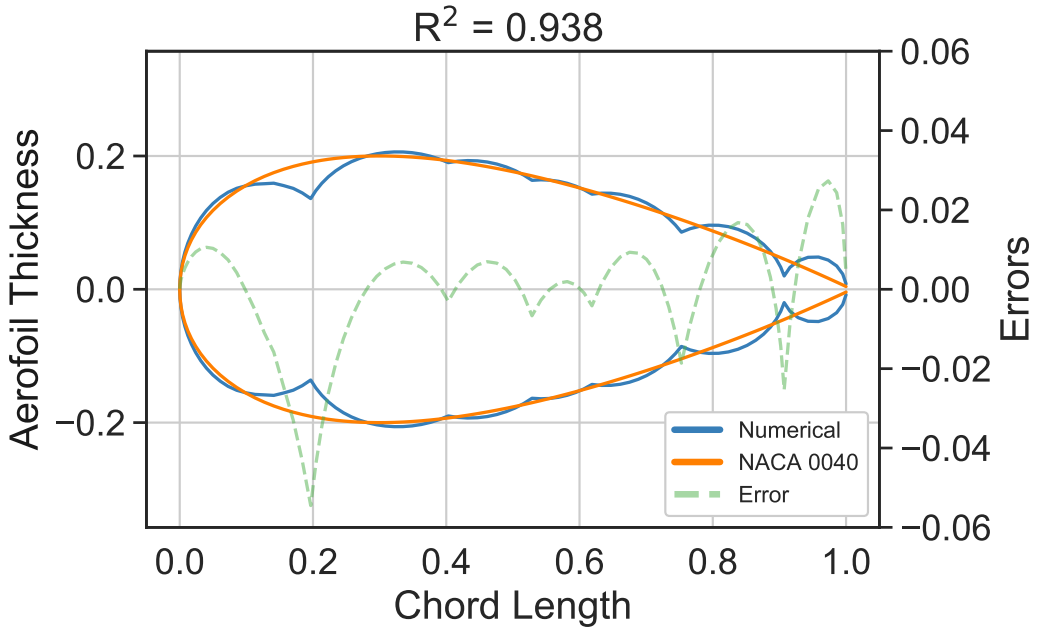

Figure 5.18: Comparison of the eight cavity numerical model's inflated profile vs. NACA 0040 aerofoil profile

Initially, it seemed the optimiser had successfully fitted the numerical model to the two profiles, however, the shape of the NACA 0015 aerofoil's trailing edge suggested that this was not the case. The trailing edge had been elongated to best fit the target aerofoil. This significant elongation of the cavity increased the total volume which decreased the pressure inside the cavity. The gauge pressure inside the trailing edge cavity was less than 100 Pa and therefore would not be sufficiently inflated to support any load.

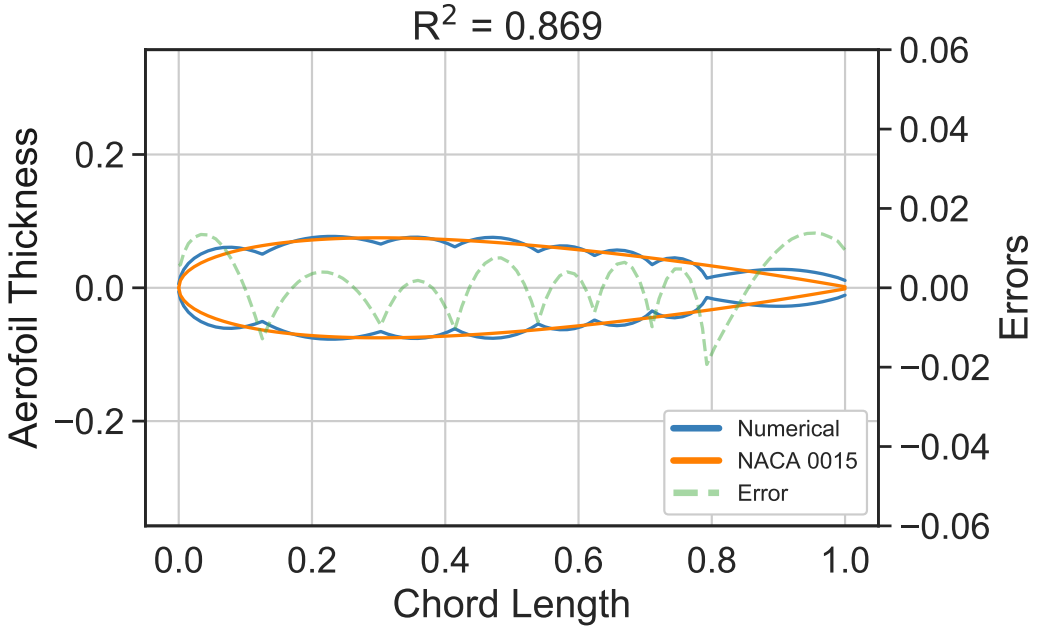

Figure 5.19: Comparison of the eight cavity numerical model's inflated profile vs. NACA 0015 aerofoil profile

A minimum pressure was not required in the cavities previously, thus the optimiser was able to take advantage of the airbag inflation model to achieve the best fit. A potential amendment to this problem was to apply a pressure load to the model for inflation instead of the airbag model. This would ensure that the minimum internal pressure is always met. However, in order to make use of the pressure load, one needed to be ensured that the inflated shape due to the pressure load is the same as when using the airbag model.

To test whether the two inflation models created the same inflated profiles, the geometry of the uninflated shape optimised three cavity model was used. The pre-pressure matched internal pressures were used to test the inflated shapes at multiple pressures. For the airbag model, the air masses used in the model's shape optimisation were applied and their internal pressures recorded. The recorded pressures inside each of the cavities were then applied to the model in the form of a pressure load instead of as an air mass. The inflated profiles of the three bag model using both the airbag model and a pressure load were plotted together to compare their profiles. These profiles can be seen in Figure 5.20.

The inflated profiles of the three cavity model using the two different inflation models compared very well, with an R^2 fit of 0.997. The three cavity model was used over the eight or fifteen cavity models to illustrate the effect of using the two different inflation models due to it being more sensitive to pressure changes

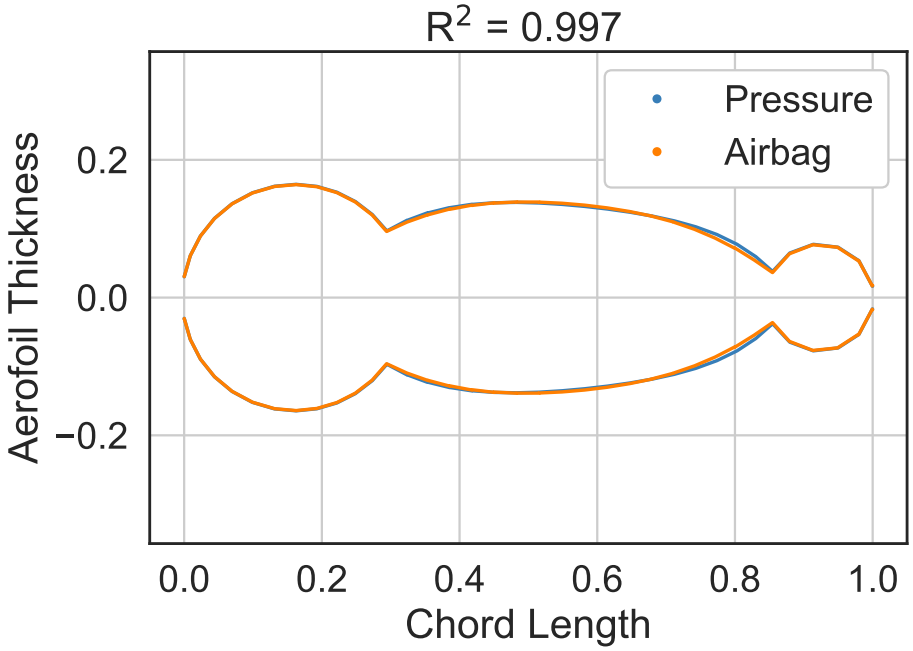

Figure 5.20: Comparison of the three cavity model's inflated profile using an airbag inflation model vs. using a pressure load model

than the others. This was indicated with the large increase in RMSE post-pressure matching compared to the other models. Therefore, if the fit between the two profiles for the worst case (three cavity model) met the criteria, then the less sensitive cases should produce better fits. This was tested with the fifteen cavity model as it produced an R^2 fit between the two profiles of 0.999, thus validating the initial assumption.

As the inflated profile using the pressure load was barely distinguishable to the profile using the airbag model, the pressure load was used for the shape optimisation of the eight cavity NACA 0015 aerofoil. The new, shape optimised, eight cavity model for the NACA 0015 aerofoil using the pressure load can be seen in Figure 5.21.

The new inflated profile of the eight cavity numerical model produced a fit with an R^2 value less than that produced by the previous iteration using the airbag model. Even though the goodness of fit decreased when using the pressure inflation, it ensured that the internal pressure remained constant at its desired value. For this reason, it was decided that for future shape optimisations the pressure load model would be used instead of the airbag model for the cavity inflation. Once the uninflated, shape optimised geometry was found, pressure matching could then be performed with the airbag model. This would allow the designer to make use of the model's stiffness prediction capabilities when under load.

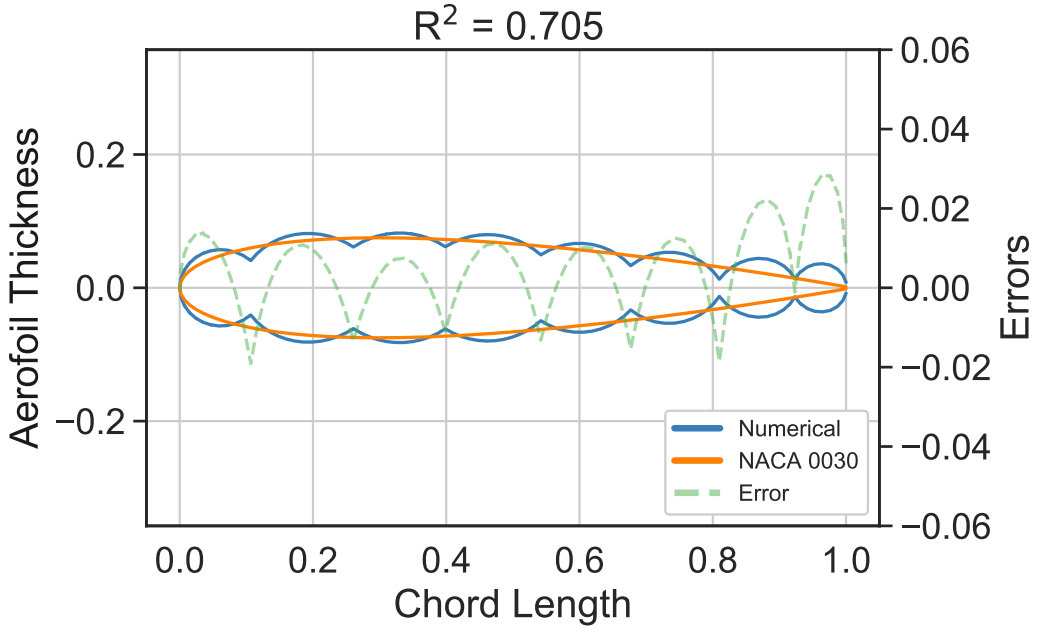

Figure 5.21: Comparison of the eight cavity numerical model's inflated profile vs. NACA 0015 aerofoil profile, using a pressure load as an inflation model

5.7 Asymmetric Aerofoil

The proposed numerical shape optimisation methodology showed its robustness in its ability to fit the inflated numerical model's profile to that of a target aerofoil profile for two different cases. The first case testing the fit when the number of inflation cavities differed and the second testing the fit when using symmetric aerofoils with varying thicknesses. However, in order to further test the robustness of the methodology, the target aerofoil profile was extended to an asymmetric profile, more specifically a cambered four-digit NACA aerofoil. The aerofoil profile used was the NACA 3430, which was the target profile for an eight cavity numerical model.

Due to the asymmetry, the number of design parameters used in the optimisation increased. The parametrised lines at the bottom of the aerofoil (see Figure 5.2) were therefore not a mirror of the top lines about the chord line. Instead, the z coordinates of both the top and bottom lines were parametrised independently of each other, while the x coordinates of the corresponding lines at the top and bottom used the same parameter. For the shape optimisation of an eight cavity model, the number of parameters increased from 18 to 27. Since the pressure load model worked well in the shape optimisation of the NACA 0015 aerofoil, it was used for the NACA 3430 as well.

Another adaptation to the methodology for the asymmetric aerofoil was the calculation of the function value. Instead of calculating the RMSE using only

the one surface, the RMSE was calculated taking into account the error on both the top and bottom surfaces. The formulation of the new RMSE can be found in Equation 5.4. Other than the stipulated changes, the shape optimisation configuration remained unchanged.

$$RMSE_{new} = \sqrt{\frac{\sum_{i=1}^{n}(z_i^* - \hat{z_i^*})^2 + \sum_{i=1}^{m}(z_i - \hat{z}_i)^2}{n+m}} \tag{5.4}$$

In the formulation in Equation 5.4, the z coordinates of the numerical model and the target aerofoil profile on the top surface are represented by $\mathbf{z}^*$ and $\hat{\mathbf{z}}^*$ respectively, where the $\mathbf{z}$ and $\hat{\mathbf{z}}$ without $(^*)$ represent the coordinates on the bottom surface. The number of coordinates compared for the top and bottom surfaces are represented by n and m respectively.

Due to the increased number of design parameters, it was assumed that the optimisation would require more time to converge to a satisfactory function value. The termination criteria was once again set to terminate the optimisation if the change of the function value between two successive iterations was less than 10^{-3}. The optimisation using the asymmetric aerofoil converged after sixteen iterations (compared to eleven for the symmetric aerofoil) where the plot of the converged numerical model's inflated profile vs. target profile from the optimisation can be seen in Figure 5.22.

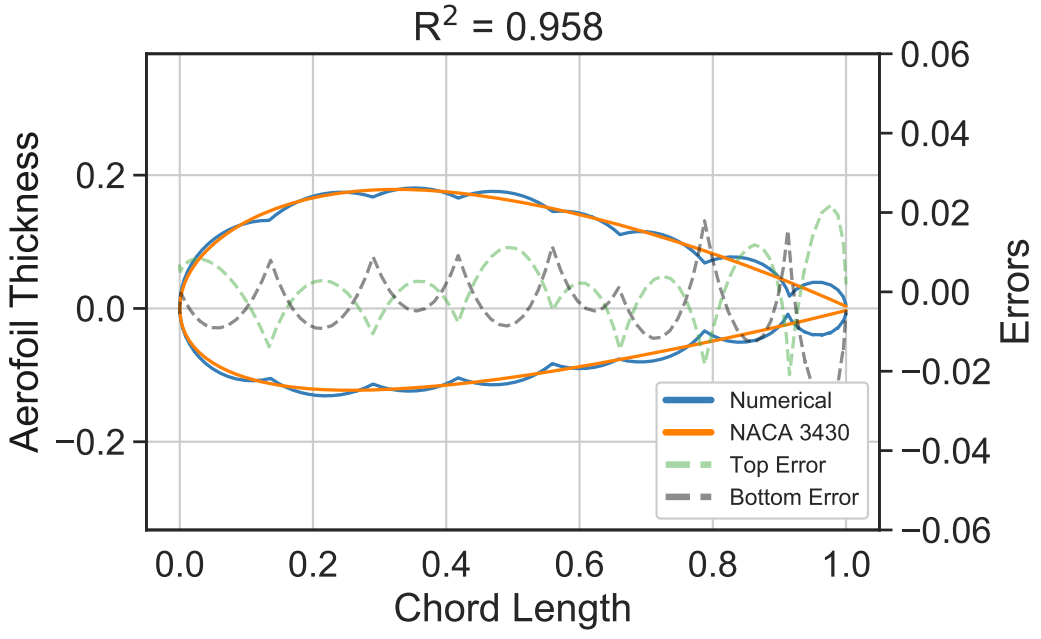

Figure 5.22: Comparison of the eight cavity numerical model's inflated profile vs. NACA 3430 aerofoil profile

Due to the asymmetry of the profile, two different error plots, for the top and bottom, were presented in Figure 5.22. The green and black dashed lines represented the error on the top and bottom surfaces respectively. The plot showed that the errors on the top and bottom surfaces were similar in magnitude and therefore no bias was imposed on either side in the optimisation. The R^2 value for the fit of the asymmetric aerofoil was found to be very close to that of the symmetric aerofoil with the same thickness, 0.958 and 0.961 respectively. This therefore shows that the optimiser was able to produce a fit for the asymmetric aerofoil of near-equal quality of a symmetric aerofoil. This is when the increase in optimisation time is accounted for with respect to the number of parameters.

5.8 Summary

To conclude with the results obtained in this chapter, the formulation of the numerical shape optimisation using the airbag inflation model was able to produce numerical models with an inflated shape fitting that of a NACA 0030 aerofoil. The fit of the numerical model to the target profile increased as the number of inflation cavities the model consisted of increased. The fits of the three, eight and fifteen cavity models to the target aerofoil represented by R^2 values of 0.557, 0.961 and 0.990 respectively.

Once the pressure inside all the cavities in the model were equalised, the inflated shapes of the numerical models were compared to physical models at the same pressure. It was found that as the number of cavities in the models increased, the fit of the numerical model to the physical model improved. Two different construction methods were compared when building the physical models where it was found that the two models produced different fits to the numerical model. For an eight cavity model, the first method produced an R^2 value of 0.962 and the second produced a value of 0.988.

Upon using different aerofoil profiles to test the robustness of the shape optimisation formulation, it was found that the airbag inflation model had a drawback as it does not ensure that the cavities were always sufficiently pressurised. However, when using the pressure load to simulate the internal pressure, it produced an inflated profile indistinguishable from that created using the airbag model. The problem of the cavities not being sufficiently inflated was thus amended.

The shape optimisation could therefore be performed using the pressure inflation model to achieve the correct inflated shape and volume. Once the uninflated shape optimised geometry was obtained, the pressure matching optimisation could then be performed using the airbag model. In order to further test the methodology's robustness, the target aerofoil profile was changed to

an asymmetric profile. This increased the number of parameters and subsequently the run time. Bearing in mind the increase in number of iterations required to achieve the same change in successive function value tolerance, the optimiser was able to produce a fit for the asymmetric profile very similar to that of a symmetric profile with the same thickness.

Chapter 6

Stiffness Validation

6.1 Finite Element Model Adaptation

As previously mentioned, the airbag model was chosen to represent the inflation of the membrane as it was found to more accurately model the inflated stiffness of the numerical model under load when compared to using a standard pressure load. Therefore, in order to confirm that the airbag model can indeed accurately model the inflated stiffness, stiffness validation tests were performed on the numerical model. These tests were in the form of four-point bending tests performed on single cavity bags instead of the inflated aerofoils, as the variable thickness of the aerofoils would make the tests more complex. However, before the tests could be performed, the numerical model had to be adapted. This section contains the adaptations made to the model.

6.1.1 Four-Point Bending Supports

In order to simulate the four-point bending tests, four cylindrical parts were created to represent the supports used in the test with the parts modelled as shell elements. The dimensions and the spacing of these supports were the same as the physical model, as shown in Section 3.2 and Appendix A.

The four-point bending test rig was constructed from mild steel and therefore the supports were modelled as such. The material properties of the mild steel used was not determined through testing, instead, they were taken from an online source, EngineeringToolbox (2001). The reason for this is because it was assumed that due to the large difference in stiffness between the steel and the polyethylene film, the steel supports will have a negligible deflection during the tests. Therefore, a slight deviation in the material properties will not affect the results. This assumption was confirmed after the supports deformed by less than 0.1 mm after the four-point bending tests. The material properties used for mild steel can be found in Table 6.1.

Table 6.1: Material properties of the mild steel used in the FE model

	Mild steel supports
Material model	Linear elastic
Thickness	2 mm
Elastic modulus	200 GPa
Poisson's ratio	0.3
Density*	2 $\times 10^6$ kg/m^3

*The reason for the steel having a smaller density than the LDPE film was due to the support's mesh being coarser than that of the bag. Since the mesh size also contributes to the simulation times, even though the steel had the lower density, the mesh size of the LDPE bag caused a bottleneck in the simulation times. This is because the supports were declared as the master surface in the contact algorithm used and therefore the penetration was searched for through its surface. Subsequently, the mesh density was not very important. However, the mesh did have to be dense enough to form the general cylindrical shape. This element size was found to be 5 mm.

6.1.2 Boundary Conditions

Two different types of boundary conditions were applied in the four-point bending test simulations, the first set of conditions were symmetry constraints which kept the inflatable bag symmetric about all the axes during inflation. Once the bag was fully inflated, the boundary conditions were removed and the supports displaced for the four-point bending test. The second type was a boundary condition applied to each of the supports, which used a displacement vs. time curve input that controlled the displacement of the supports from their original position in the z direction.

The boundary conditions applied to the models for the four-point bending tests can be seen on the model of the 75 mm bag in Figure 6.1. The constrained degrees of freedom for boundary conditions of the bag symmetry can be found in Table 6.2. The translation constraint is represented by T and the rotation constraints are represented by R.

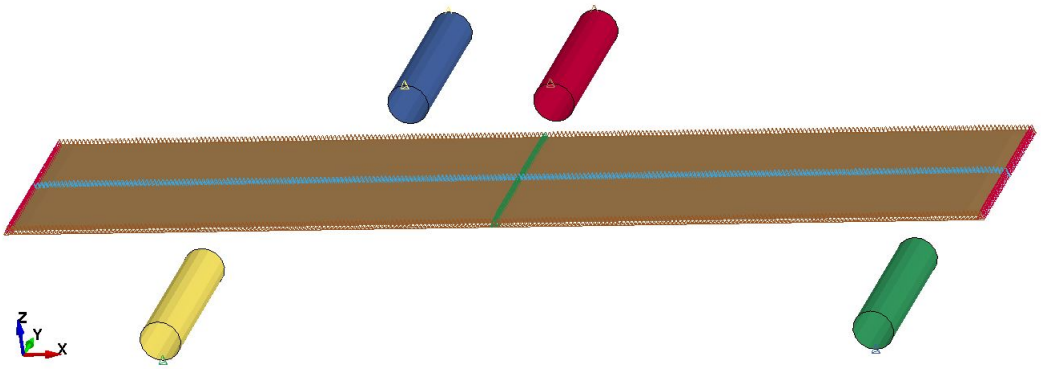

Figure 6.1: Boundary conditions applied to the model in its state prior to inflation

Table 6.2: Constrained degrees of freedom for each node set for the simulation of the four-point bending tests

Node set description	Constrained degrees of freedom
Along x-axis down the center	T_y,R_x,R_z
Along y-axis down the center	T_x,R_y,R_z
Along x-axis on the edge	T_z
Along y-axis on the edge	T_z

6.1.3 Contact

Two different types of contact were used in the simulation of the four-point bending tests. The first of the types was a surface to surface option. This contact algorithm was responsible for the contact between the supports and the inflatable bag. As previously mentioned, the slave nodes were represented by the bags' nodes and the master surface was the surface of the mild steel supports. This type of contact is a two-way contact algorithm and therefore, instead of it searching only for penetration of the slave nodes through the master surface, penetration of the master nodes through the slave surface was also searched for.

Using two-way contact did increase the computation time due to the extra searching, however, it was necessary as the master nodes penetrated through the slave surface when one-way contact was used. This was found to be the case whether the slave nodes were those on the bag or the supports.

The SOFT contact option was enabled for the surface to surface contact as it is used when a soft material is in contact with a stiff material or when the mesh densities of the two contact surfaces are dissimilar (Hallquist, 1986). This was the case, as the steel is much stiffer than the polyethylene film. The SOFT = 1 option in LS-DYNA is not very different from the penalty-based constraint except for the way the contact stiffness is determined. When using the SOFT = 1 constraint, the maximum of the stiffnesses between the SOFT = 1 and penalty-based constraint is used.

The second type of contact used was the single surface contact which was applied to the inflatable bag. This contact type was responsible for the self-contact of the inflatable bag when wrinkling occurred. An alternative contact option was considered for the self-contact of the bag, this type of contact is generally used for airbag inflation, however, it involves performing more frequent searches for penetration. Since the inflatable bags are not being inflated rapidly, it was decided that this specific contact type was not necessary.

6.2 Four-Point Bending Tests

Using the adapted FE model, four-point bending tests were simulated and compared to that of physical tests to validate the stiffness of the numerical model. These tests were performed on each of the different sized bags with each of the bags being tested at three different pressures. For the physical tests, three physical models of each bag size were built and tested, with each model tested three times. This was done to establish confidence in the test results.

6.2.1 Physical Tests

The inflation pressures of the bags were dependant on the maximum allowable inflation pressure of each bag. Once the maximum pressure was found, the highest working pressure was chosen to be a few kPa less than the maximum allowable pressure to allow for a safety factor. The remaining two pressures were chosen by selecting pressures in between the highest working pressure and 0 kPa. At least one of the pressures of a bag overlapped with another bag to compare the effect of a change in diameter, with a constant pressure. The pressures for each of the bags can be seen in Table 6.3.

Table 6.3: Pressures in kPa corresponding to the different bag sizes

	50 mm	75 mm	100 mm
Maximum allowable pressure	17	11.3	8.5
Pressure 1	5.75	5.75	4.75
Pressure 2	9.00	6.75	5.75
Pressure 3	15.00	9.00	6.75

The setup for the inflation of the bag consisted of a pressure input tube connected to the one end of the bag and another tube leading into a pressure transducer on the other end. Once the target pressure was reached, a valve controlling the airflow into the bag was turned off, stopping airflow to and from the bag, and the four-point bending tests commenced. During the tests, the top supports were displaced 45 mm downwards from the point where it initially made contact with the bag while the force vs. displacement data was recorded.

The results from the four-point bending tests for the three different sized models can be found in Figure G.1. This is in the form of force vs. displacement curves, with a 99 % confidence interval of all nine tests performed for each bag size plotted as a shaded area surrounding a solid line representing the average. For each of the different sized models, all three pressures were plotted on the same graph. This was done to visualise the effect of pressure on the bags at a constant bag size.

In Figure G.1, the 99 % confidence bands showed that there was a slight variability in the physical results of the 50 mm bag. However, this slight variation diminished as the bag sizes increased, producing force vs. displacement curves for the 75 and 100 mm bags where there was almost no confidence bands. As expected from literature discussed in Section 2.1, it was also found that with an increase in pressure the stiffness of the bag also increased.

Another set of plots was created in Figure G.2 where the force vs. displacement data of the different sized bags were plotted on the same figure at overlapping pressures. At 40 mm for the tests of the bags at 5.75 kPa, the 50 mm bag exhibited a corresponding force value of 8.36 N whereas the 100 mm bag had a value of 39.78 N. Therefore, by doubling the bag diameter, the force at 40 mm increased by 375 %.

When comparing the results at 40 mm for the tests at a constant bag size of 50 mm, the corresponding force values only increased from 8.36 N to 12.20 N when increasing the pressure from 5.75 kPa to 15.00 kPa. That is a 46 %

increase in force from a 160 % increase in gauge pressure. From these results, it was found that the bag size, and thus air mass inside the closed volume, has a larger effect on the stiffness of the inflated model compared to the internally applied pressure.

6.2.2 Numerical Tests

Using the new, adapted FE model, four-point bending test simulations were performed on all three different sized models at each of their three pressures. In order to acquire the force acting on the supports, data from the `rcforce` output file was extracted which contains the contact force at each of the nodes. The forces for each of the nodes at a support were summed together to determine the reaction forces.

Due to the added inertia from the mass scaling, the dynamic aspect of the simulation was non-real and therefore the simulation was run until the kinetic energy of the system was zero. For each test, the supports were displaced to 5, 10, 20, 30 and 40 mm, the kinetic energy allowed to dissipate and then the contact forces recorded at each displacement. The recorded values were then plotted on the force vs. displacement curves of their respective physical tests. An image of the 75 mm numerical model with the supports displaced to 40 mm during the four-point bending test can be found in Figure 6.2.

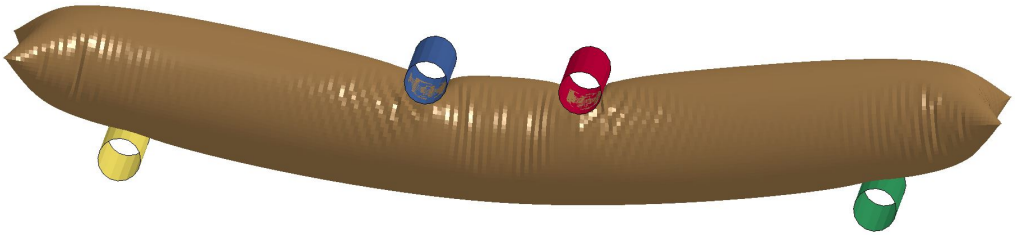

Figure 6.2: A 75 mm bag during a four-point bending test simulation

The force vs. displacement curves for the four-point bending tests performed on the 75 mm bag at its three pressures can be seen in Figure 6.3, whereas the plots for the 50 and 100 mm models can be seen in Figures G.3 and G.4.

Figure 6.3 represents the force vs. displacement results of the 75 mm bag under four-point bending and at low displacements, the numerical model can predict the physical model's corresponding force value with a low error. However, as the displacement of the supports increase, so deviates the corresponding force values.

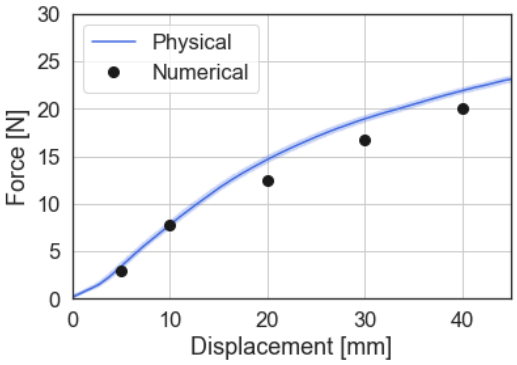

(a) Inflatable bag at 5.75 kPa.

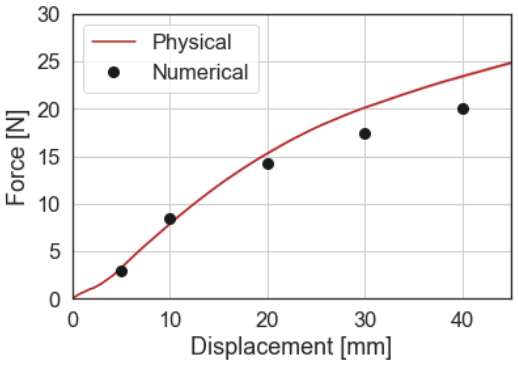

(b) Inflatable bag at 6.75 kPa.

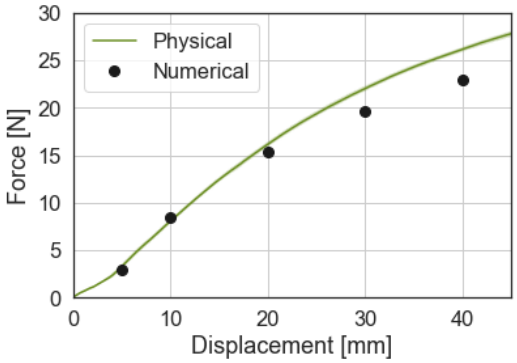

(c) Inflatable bag at 9.00 kPa.

Figure 6.3: The numerical force vs. displacement values for the 75 mm bags plotted with the data from the physical tests

A similar trend was also found for the 50 and 100 mm bags as the results correlated well at some points, however, they still deviated at other points. For example, the 50 mm model correlated well for most of the points but deviated at a displacement of approximately 20 to 30 mm. The results from the 100 mm model initially deviated, however at the larger displacements it showed a better correlation.

In order to statistically represent the deviation between the physical and numerical force vs. displacement data, the RMSE value between the force value at their corresponding displacement values were determined. These RMSE values for each bag size at all their pressures can be found in Table 6.4.

Table 6.4: A statistical measure of the deviations in resulting force between the numerical and physical model for all three bags under a four-point bending load

Bag	Pressure [kPa]	RMSE [N]
50	5.75	0.48
	9.00	0.38
	15.00	0.79
75	5.75	1.63
	6.75	2.04
	9.00	1.75
100	4.75	3.14
	5.75	2.22
	6.75	3.42

From the data in Table 6.4, the RMSE between the numerical and physical data was found to increase as the bag size, and subsequently, the stiffness increased. However, it was found that with an increase in pressure, there was not necessarily an increase in RMSE. Even though the airbag model was not able to perfectly model the inflated stiffness of the structure, as seen in the slight difference in the shapes of the plots created by the data, it was able to model it with a low error. The size of the error is considered low bearing in mind the scales of the forces.

6.3 Shape Validation Under Load

In order to build further confidence in the numerical model, the geometries of the single cavity bags under a four-point bending load were captured whilst the supports were displaced to 40 mm and compared to that of the numerical model. This was done in the same way as the bags under no load in Section 4.2. The geometry of all three of the bags were compared with all of them pressurised to 5.75 kPa.

6.3.1 Point Cloud Comparison

Unlike the bag under no load, the entire bag could not be scanned whilst under a four-point bending load due to the pillars of the tensile testing rig getting in between the line of sight of the bag and the 3D scanner. Therefore, only a quarter of the bag was scanned, which was acceptable due to the symmetry of the bag. Instead of the bags being scanned in their original position in the tensile testing machine, as seen in Figure 6.4a, rotation parts were manufac-

tured which rotated the four-point bending rig to enable a better field of view for the scanning. The drawings for these parts can be found in Appendix F and the rotated four-point bending rig can be seen in Figure 6.4b.

(a) The original orientation of the four-point bending test rig in the tensile testing machine machine

(b) The rotated orientation of the four-point bending test rig in the tensile testing machine

Figure 6.4: The four-point bending test rig positioned in different orientations in the tensile testing machine

Instead of all three symmetry planes for the bags being plotted, only two were plotted for the bags under load. This is because the points lying near the xy plane produced noisy plots due to the deformation of the model. The symmetry plane plots on the xz and yz planes for the 75 mm bag can be seen in Figure 6.5 and the plots for the 50 and 100 mm bags can be found in Figures B.3 and B.4.

As previously mentioned, the test rig was rotated to achieve a better line of sight between the bag and the 3D scanner. Even though it did improve the line of sight, the position of the bag in the rig made it difficult to scan. This can be seen as the missing data in the point clouds in the plots. Visually, there seemed to be a good correlation between the point clouds of the numerical model and that of the physical model. However, in order to gain a better understanding, the Hausdorff distances between the data sets were referred to. Table 6.5 contains the Hausdorff distances for each of the different sized bags on both of the planes.

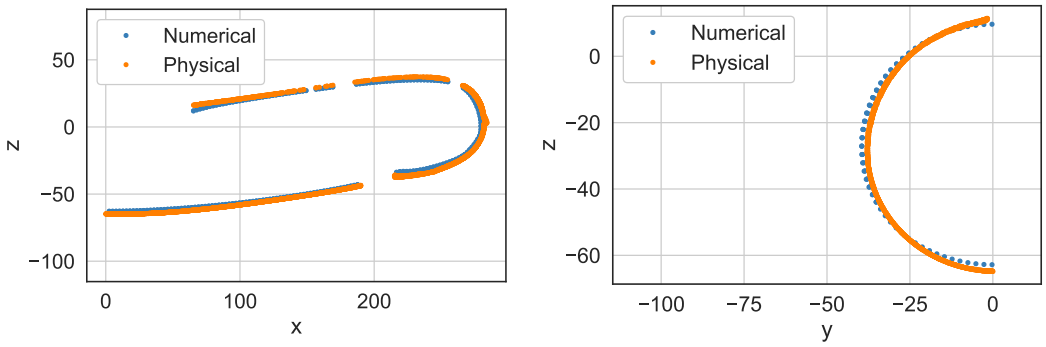

(a) On the xz plane.

(b) On the yz plane.

Figure 6.5: Symmetry plane plots comparing the shape of the numerical and physical model of a 75 mm inflated bag under four-point bending

Table 6.5: Hausdorff distances for the different sized bags under a four-point bending load on the respective symmetry planes

Bag	Plane	Hausdorff [mm]
⌀50	xz	4.23
	yz	2.24
⌀75	xz	5.3
	yz	2.74
⌀100	xz	5.43
	yz	2.78

When looking at the Hausdorff distances in Table 6.5 it can be seen that as the bag sizes increase, the Hausdorff distances also increase; however, the increase in Hausdorff distance is much smaller than the corresponding increase in diameter. This is positive as it shows that the numerical model is still able to maintain a small error even when scaling up the model. The Hausdorff distances also show that there is a larger deviation between the shapes of the physical and numerical model on the xz plane compared to the yz plane. This is also evident when looking at the plots in Figure 6.5.

The largest deviation between the plots on the xz plane appears to be at the top left and the bottom left of the bag. These are the areas where the supports come into contact with the bag. The membrane of the numerical model shows a more gradual gradient on the lead up to the indentation caused by the support, compared to the physical model. The plots on the yz plane

show a very good correlation between the two models which is confirmed when referring to the Hausdorff distances.

6.4 Summary

The four-point bending tests performed on the physical models provided an understanding of the influence of the bag size and the internal pressure on the inflated stiffness of the model. The results showed that the volume of the bag contributed more to the inflated stiffness compared to the pressure of the bag. This conclusion was drawn after observing a 375 % increase in corresponding force when increasing the bag's volume by 100 % and observing only a 46 % increase in force with a 160 % increase in pressure.

Upon comparing the inflated stiffnesses of the numerical models, determined through four-point bending tests, to that of their corresponding physical models, a strong correlation between the values were found. This was through observing the close fits of the numerical and physical force vs. displacement data in Figures 6.3, G.3 and G.4. The RMSE values between the two data sets were also found to be small, however, they increased the larger the bag size and subsequently, the inflated stiffness increased. Due to the errors being low relative to the models' stiffnesses, the numerical model's ability to predict the inflated stiffness was deemed to be acceptable.

Further confidence in the model's ability to predict its corresponding physical models' stiffness was built upon referring to the shape comparison of the numerical and physical inflatable bags under four-point bending load. The geometry of the models on the symmetry planes were compared and a strong correlation between the geometries were found. This strong correlation was confirmed by the small Hausdorff distances between the two data sets.

Chapter 7

Concluding Remarks

7.1 Conclusion

The numerical shape optimisation methodology proposed in this thesis was able to determine the uninflated, shape optimised geometry of numerical models with inflated shapes fitting that of a target aerofoil profile. The influence of the differing number of inflation cavities on the numerical model's fit was tested and it was found that as the number of cavities increased, so improved the fit. However, the improvement in fit after each subsequent model diminished as the number of inflation cavities increased. This was determined upon comparing the R^2 fits between the inflated numerical and target profiles for the three, eight and fifteen cavity models which were 0.557, 0.961 and 0.990 respectively. This shows a larger difference between the R^2 values of the three and eight cavity models compared to that between the eight and fifteen cavity models.

Initially, the NACA 0030 aerofoil profile was used as the target profile as it provided a good balance between thickness and fit potential of the numerical model. However, in order to determine the robustness of the methodology, optimisations were performed using a profile thinner and thicker than the NACA 0030 as the target aerofoil profile (NACA 0015 and NACA 0040 respectively). The inflated profiles of the numerical models with eight cavities produced R^2 fits of 0.869 and 0.938 respectively. However, the former profile showed a drawback to using the airbag inflation model, as it was able to produce a good fit at the trailing edge at the cost of barely being inflated.

In order to amend the problem of the cavity not being inflated properly, a pressure load inflation model was used instead. This made sure that the cavity was fully inflated. In order to determine whether the pressure load produced an inflated shape identical to when the airbag model is used, the three and fifteen cavity models were inflated to the same pressures using both inflation

models and the profiles compared. Upon comparing the profiles, it was found that they were indistinguishable and therefore the pressure inflation model was used to rerun the shape optimisation of the NACA 0015 aerofoil.

The problem of the low pressures in the inflation cavities was amended by using the pressure load inflation model. Therefore, it was decided that the pressure load inflation model was the better option for the initial shape optimisation. Once the shape optimised geometry had been determined, a pressure matching optimisation could be performed to acquire the correct pressures using the airbag model.

The shape optimisation was proven to work well when the target aerofoil profile was symmetric. However, to further test the capabilities of the methodology, an asymmetric aerofoil profile was used as the target profile (the NACA 3430). Due to the increase in design parameters, the optimiser required more iterations, when compared to the symmetric profile, to reach a converged solution. The fit of the inflated numerical model profile to the target profile was very similar to that of a symmetric profile with an R^2 value of 0.952. This large R^2 value thus showed that the shape optimisation could be accurately extended to instances where the target aerofoil profile is asymmetric.

Since the aim of the methodology was to acquire an uninflated geometry which could be used to construct a physical model, the numerical model had to accurately predict the inflated shape of its corresponding physical model. The shape of the inflated numerical model was validated in two separate instances. Firstly, by comparing the inflated profiles of single cavity numerical and physical bags, it was found that the error between the numerical and physical point clouds was low. Secondly, the inflated profiles of an eight cavity physical and numerical model were compared where the R^2 fit between the profiles was 0.988. These results showed that the numerical model was able to accurately predict the inflated shape of its corresponding physical model.

Airbag inflation was used to inflate the final shape optimised model due to it being able to accurately predict the inflated stiffness of the model. To test whether this was the case, four-point bending tests were performed on single cavity bags and the force vs. displacement data of physical tests were compared to that from numerical simulations.

The shape of the force vs. displacement curves produced from the physical and numerical tests were similar, as well as the RMSE values between the corresponding forces being small. An increase in the internal pressure of the model also yielded an increase in inflated stiffness. These results show that even though using the airbag model does require additional work compared to the pressure load model, it can accurately predict the inflated stiffness of the

physical model.

The design methodology had proven to meet the stipulated aim and objectives as well as incorporate additional elements that add value, such as the methodology's ability to accurately predict the stiffness of its corresponding physical model when under load. This will allow the numerical model's use to be extended to applications that require predicting its deflection under load. The methodology also demonstrated that physical models, accurately fitting that of a target aerofoil profile, could be constructed. This, along with the supporting results, strongly suggests that this is a viable approach to solve the problem of accurately predicting the inflated profile of an inflatable aerofoil.

7.2 Recommendations and Future Work

The research presented in this thesis aimed to create a design methodology that would determine the uninflated geometry for an inflatable aerofoil profile, accurately fitting that of a target aerofoil profile. This was to be accomplished using a numerical model that can accurately predict the inflated shape of its corresponding physical model. This aim was met, in addition to it being able to accurately predict the inflated stiffness of its corresponding numerical model. The basic construct of the design methodology can be adapted to extend to different design scenarios.

As mentioned in Section 4.1, the unsupported film was selected for construction of the physical models due to its ease of use during the design process. However, a drawback of this is that the configuration does not allow for large inflation pressures. Future work could entail amending this problem by converting the material model from an unsupported film to a bladder and restraint configuration. Even though this will make the model more complex and could increase simulation times, the load-bearing capacity of the structure would increase due to the larger inflation pressure and possibly stiffer material.

Additional future work could entail performing aerodynamic simulations on the profiles produced by the current design methodology to gain a better understanding of the aerodynamic effects of the bumps on the different profiles. Physical models can also be subjected to wind tunnel tests to determine the response of the model under an aerodynamic load. The ability of the model to accurately predict the stiffness of its physical model would also allow for static load tests to be numerically simulated. This would benefit the designer, in terms of the reduced time spent on construction and performing the physical tests.

Appendices

Appendix A

Four-Point Bending Test Rig

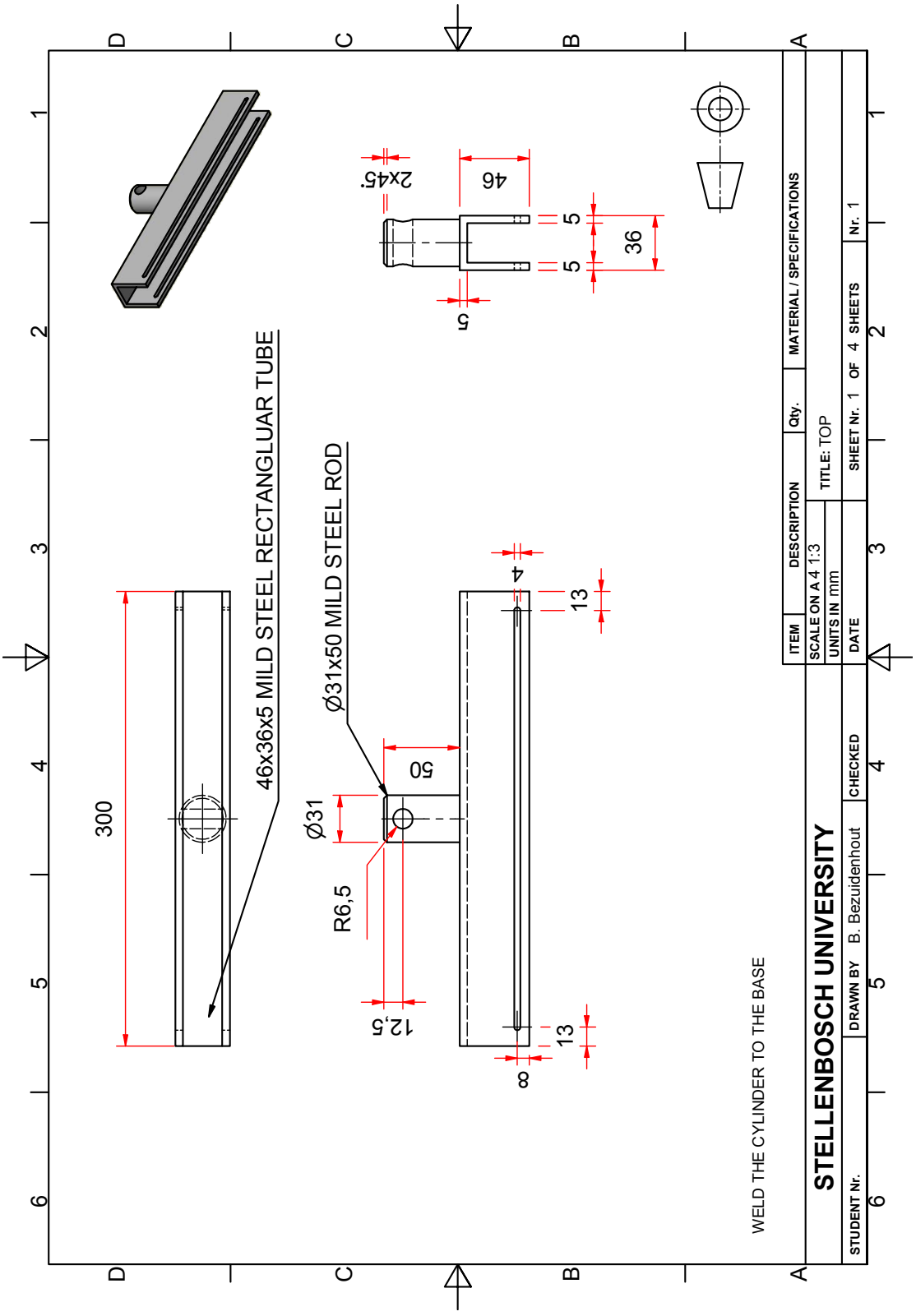

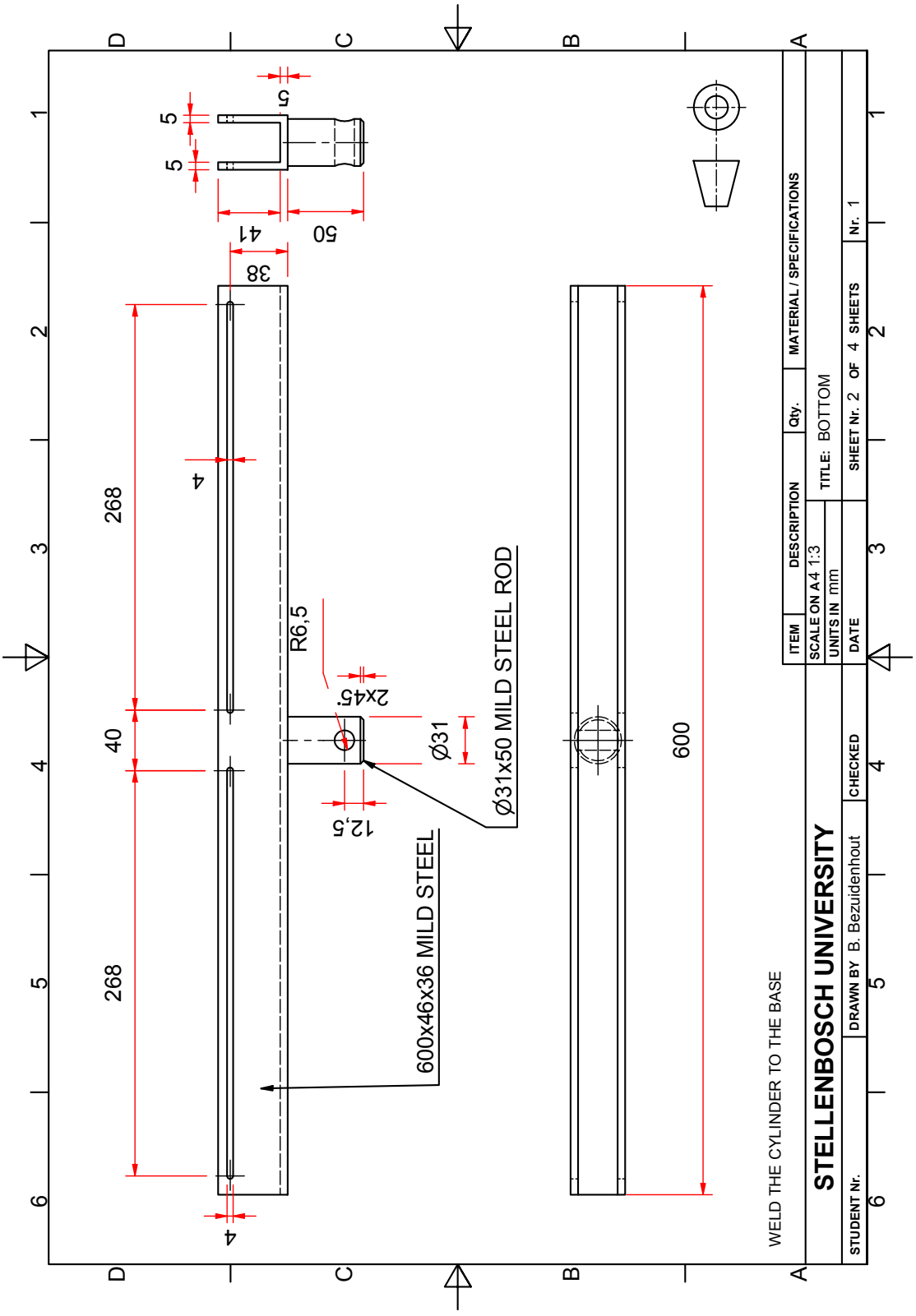

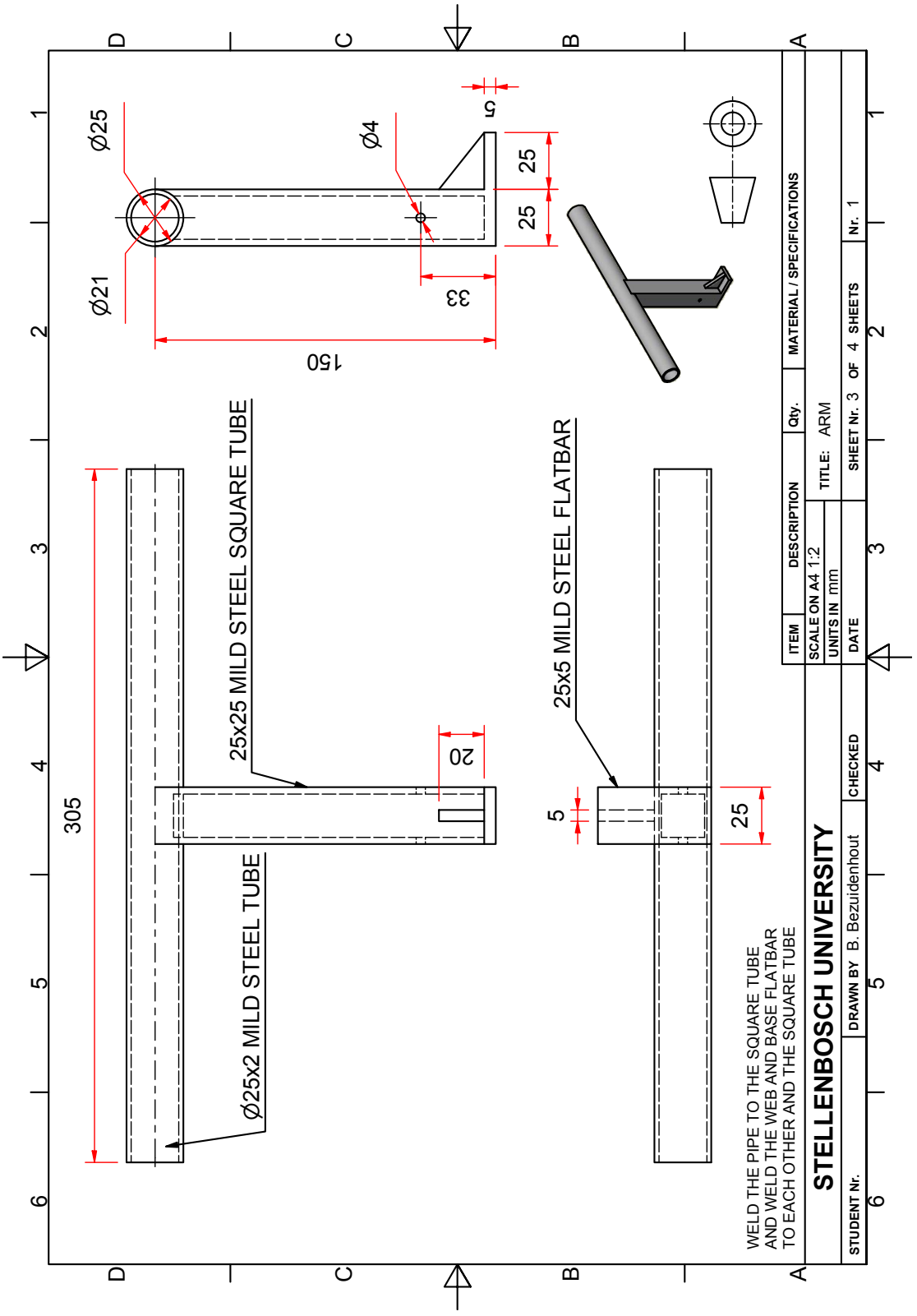

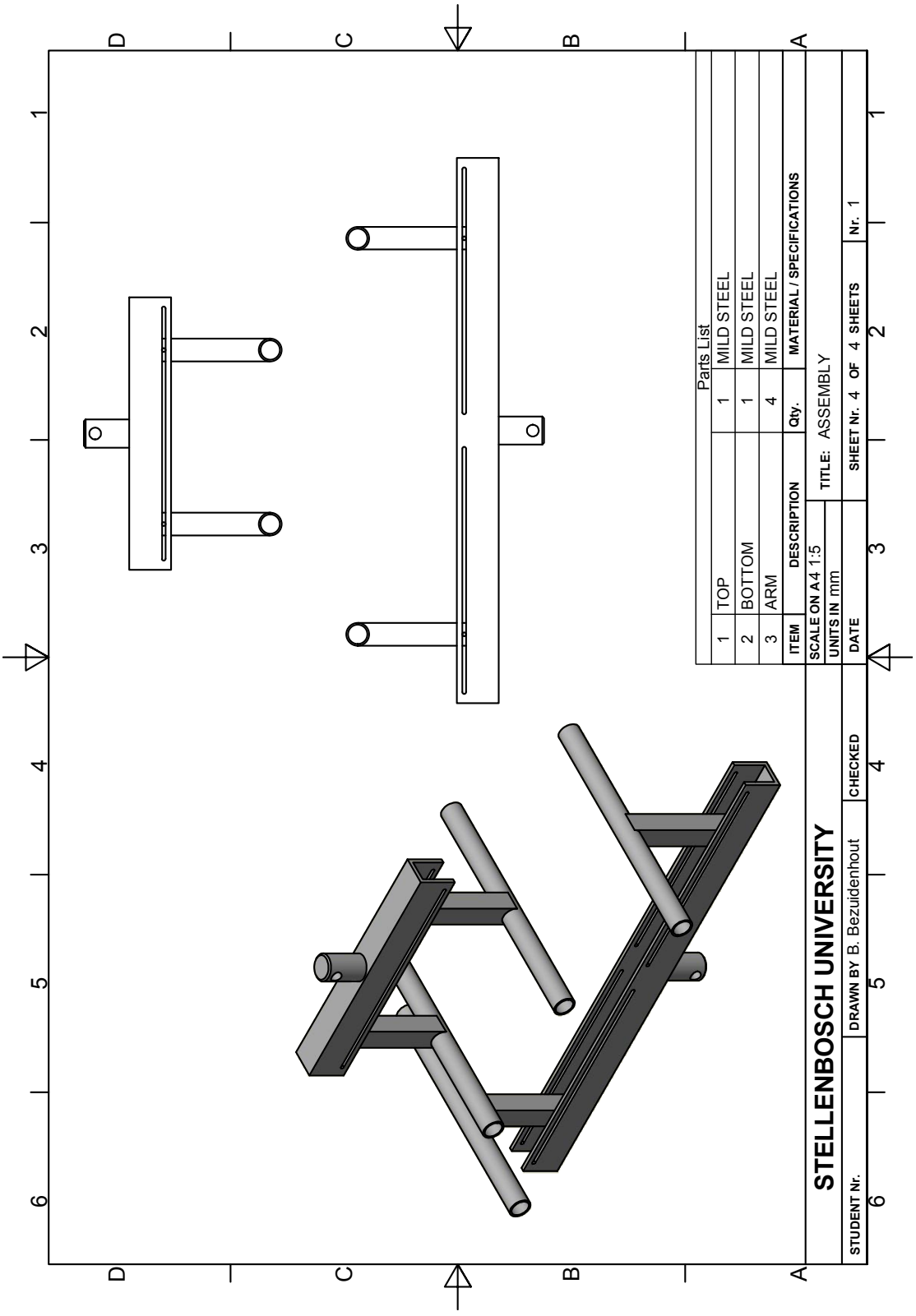

Appendix B

Symmetry Plane Plots

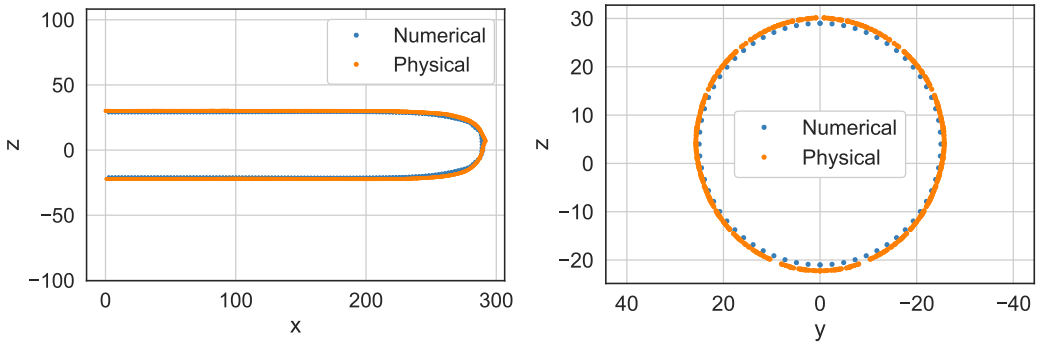

(a) On the xz plane.

(b) On the yz plane.

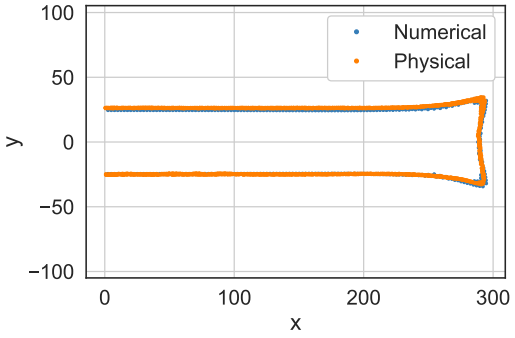

(c) On the xy plane.

Figure B.1: Symmetry plane plots comparing the shape of the numerical and physical model of a 50 mm inflated bag under no load

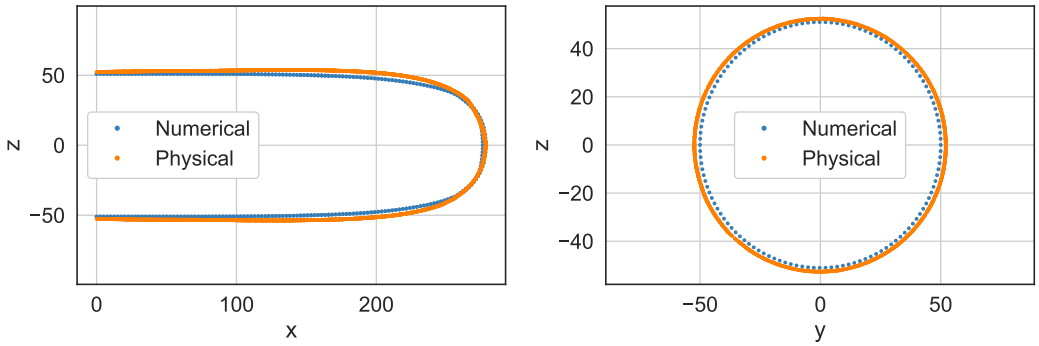

(a) On the xz plane.

(b) On the yz plane.

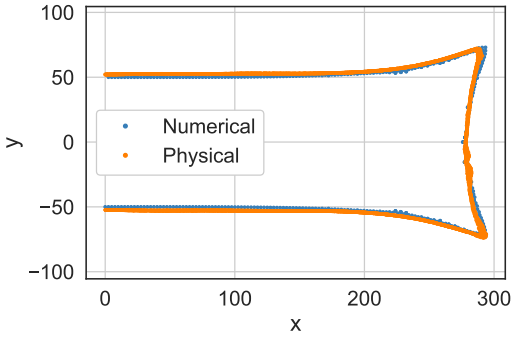

(c) On the xy plane.

Figure B.2: Symmetry plane plots comparing the shape of the numerical and physical model of a 100 mm inflated bag under no load

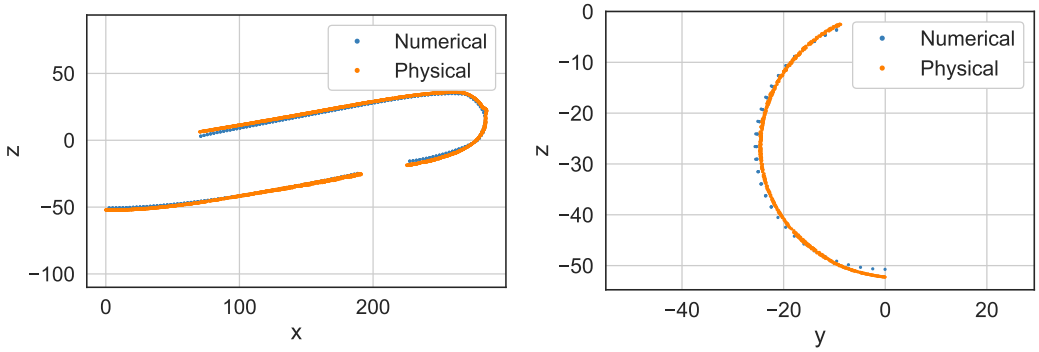

(a) On the xz plane.

(b) On the yz plane.

Figure B.3: Symmetry plane plots comparing the shape of the numerical and physical model of a 50 mm inflated bag under a four-point bending

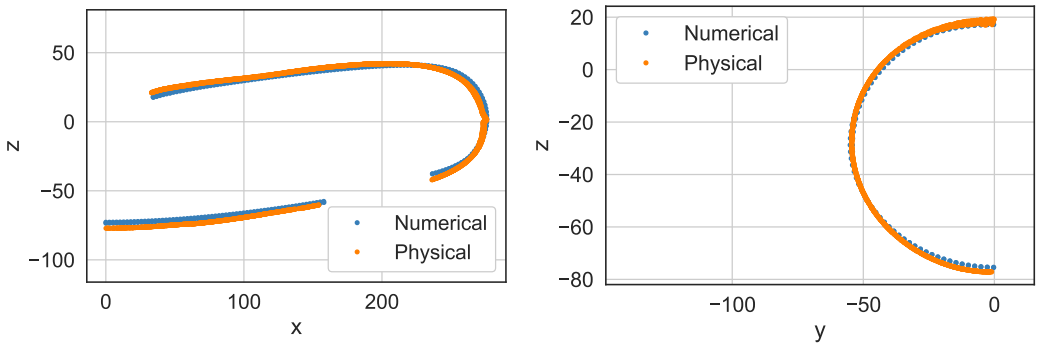

(a) On the xz plane.

(b) On the yz plane.

Figure B.4: Symmetry plane plots comparing the shape of the numerical and physical model of a 100 mm inflated bag under a four-point bending

Appendix C

Main Keyword File for Three Bag Model

```
$# LS-DYNA Keyword file created by LS-PrePost(R) V4.6.4 -
20Mar2019
$# Created on May-27-2019 (16:50:25)
*KEYWORD
*TITLE
$#
title
LS-DYNA keyword deck by LS-PrePost
*CONTROL_ENERGY
$#    hgen      rwen    slnten     rylen
         2         2         2         2
*CONTROL_TERMINATION
$#  endtim    endcyc     dtmin    endeng    endmas      nosol
       2.0         0       0.0       0.0       0.0          0
*DAMPING_GLOBAL
$#    lcid    valdmp       stx       sty       stz       srx
sry       srz
         0      20.0       0.0       0.0       0.0       0.0
0.0       0.0
*CONTROL_TIMESTEP
$#  dtinit    tssfac      isdo    tslimt     dt2ms      lctm
erode     ms1st
       0.0       0.9         0       0.0       0.0          0
0         0
$#  dt2msf   dt2mslc     imscl    unused    unused     rmscl
       0.0         0         0                             0.0
*DEFINE_CURVE_TITLE
Mass_In_1
$#    lcid      sidr       sfa       sfo      offa      offo
dattyp     lcint
         1         0       5.0       0.6       0.0       0.0
0         0
$#                a1                  o1
                0.0                 0.0
               0.02               0.001
               0.04               0.001
               0.06                 0.0
                0.1                 0.0
*DEFINE_CURVE_TITLE
Mass_In_2
$#    lcid      sidr       sfa       sfo      offa      offo
dattyp     lcint
         2         0       5.0       0.6       0.0       0.0
0         0
$#                a1                  o1
                0.0                 0.0
               0.02               0.001
               0.04               0.001
               0.06                 0.0
                0.1                 0.0
*DEFINE_CURVE_TITLE
Mass_In_3
$#    lcid      sidr       sfa       sfo      offa      offo
dattyp     lcint
         3         0       5.0        0.6      0.0       0.0
0         0
$#                a1                  o1
```

```
                0.0                 0.0
               0.02               0.001
               0.04               0.001
               0.06                 0.0
                0.1                 0.0
*INCLUDE
$#
filename
Temp.k
*DATABASE_NODOUT
$#      dt    binary      lcur     ioopt   option1   option2
         2         2         0         1       0.0         0
*DATABASE_ABSTAT
$#      dt    binary      lcur     ioopt
         2         2         0         1
*DATABASE_BINARY_D3PLOT
$#      dt      lcdt      beam     npltc    psetid
         1         0         0         0         0
$#   ioopt
         0
*DATABASE_HISTORY_NODE_SET
$#     id1       id2       id3       id4       id5       id6
id7       id8
         1         0         0         0         0         0
0         0
*AIRBAG_SIMPLE_AIRBAG_MODEL_ID
$#      id
title
         1Tube_1
$#     sid    sidtyp      rbid      vsca      psca      vini
mwd      spsf
         1         1         0       1.0       1.0       0.0
0.0       0.0
$#      cv        cp         t      lcid        mu      area
pe        ro
     717.0    1004.0     300.0         1       0.7       0.0
101300.0     1.204
$#     lou      text         a         b        mw      gasc
         0       0.0       0.0       0.0       0.0       0.0
*AIRBAG_SIMPLE_AIRBAG_MODEL_ID
$#      id
title
         2Tube_2
$#     sid    sidtyp      rbid      vsca      psca      vini
mwd      spsf
         2         1         0       1.0       1.0       0.0
0.0       0.0
$#      cv        cp         t      lcid        mu      area
pe        ro
     717.0    1004.0     300.0         2       0.7       0.0
101300.0     1.204
$#     lou      text         a         b        mw      gasc
         0       0.0       0.0       0.0       0.0       0.0
*AIRBAG_SIMPLE_AIRBAG_MODEL_ID
$#      id
title
         3Tube_3
```

```
$#     sid    sidtyp       rbid       vsca       psca       vini
mwd      spsf
         3         1          0        1.0        1.0        0.0
0.0        0.0
$#      cv         cp         t      lcid         mu       area
pe         ro
     717.0    1004.0     300.0         3        0.7        0.0
101300.0     1.204
$#     lou       text          a          b         mw       gasc
         0        0.0        0.0        0.0        0.0        0.0
*SECTION_SHELL_TITLE
Outer
$#   secid    elform      shrf       nip     propt   qr/irid
icomp     setyp
         1         9     0.833         2       1.0          0
0          1
$#      t1         t2         t3         t4      nloc     marea
idof    edgset
8.50000E-58.50000E-58.50000E-58.50000E-5       0.0        0.0
0.0          0
*SECTION_SHELL_TITLE
Inner
$#   secid    elform      shrf       nip     propt   qr/irid
icomp     setyp
         2         9     0.833         2       1.0          0
0          1
$#      t1         t2         t3         t4      nloc     marea
idof    edgset
4.25000E-54.25000E-54.25000E-54.25000E-5       0.0        0.0
0.0          0
*MAT_ELASTIC_TITLE
Polyethylene
$#     mid        ro         e         pr         da         db
not used
         11.800000E72.400000E8       0.4        0.0        0.0
0.0
*END
```

Appendix D

Metamodel Optimisation Results

The results for the different configurations tested on the three bag model are in Table D.1. The optimisations for the different configurations were each run for seven iterations with each iteration consisting of 80 design points. The maximin space filling algorithm was used to populate the design space. The metamodels tested were the RBF and linear metamodel. The quadratic model was considered, however, it required a minimum of 118 design points in order to formulate the model. It was thus omitted as it required a significant increase in design points compared to the other models.

The RBF metamodel had the option to include the design points from the previous iterations into the current iteration's metamodel. The configurations with the RBF metamodels were therefore tested with the previous points both included and excluded.

Table D.1: Results of the different optimisation configurations for the shape optimisation of the three bag numerical models

	Test 1	Test 2	Test 3	Test 4	Test 5
Metamodel	RBF	RBF	RBF	RBF	Linear
Optimiser	GA	GA	LFOP	LFOP	LFOP
Old points	Excluded	Included	Excluded	Included	
Last R^2	0.911	0.959	0.794	0.950	0.851
Mean R^2	0.867	0.914	0.848	0.913	0.745
Best R^2	0.976	0.959	0.924	0.954	0.851
Min $f(x)$	0.0260	0.0379	0.0298	0.0360	0.0334

Appendix E

Physical Models

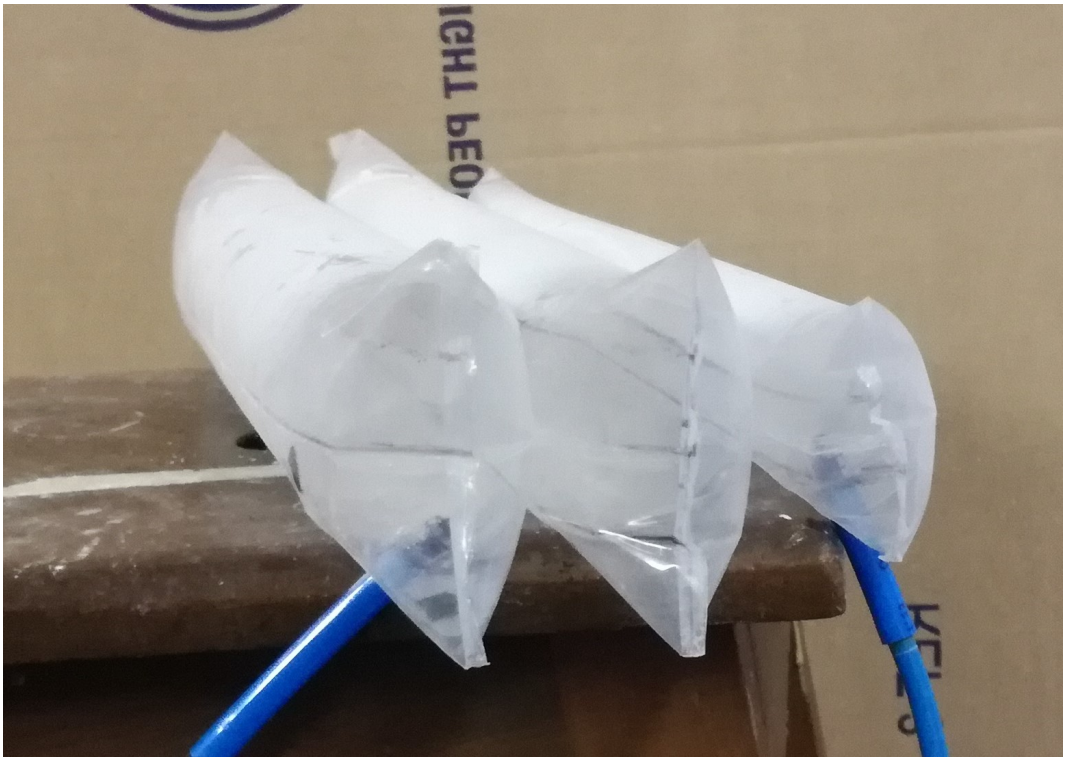

Figure E.1: The inflated physical model of the three cavity aerofoil

Figure E.2: The inflated physical model of the eight cavity aerofoil

Appendix F

Rotation Pieces for Four-Point Bending Test Rigs

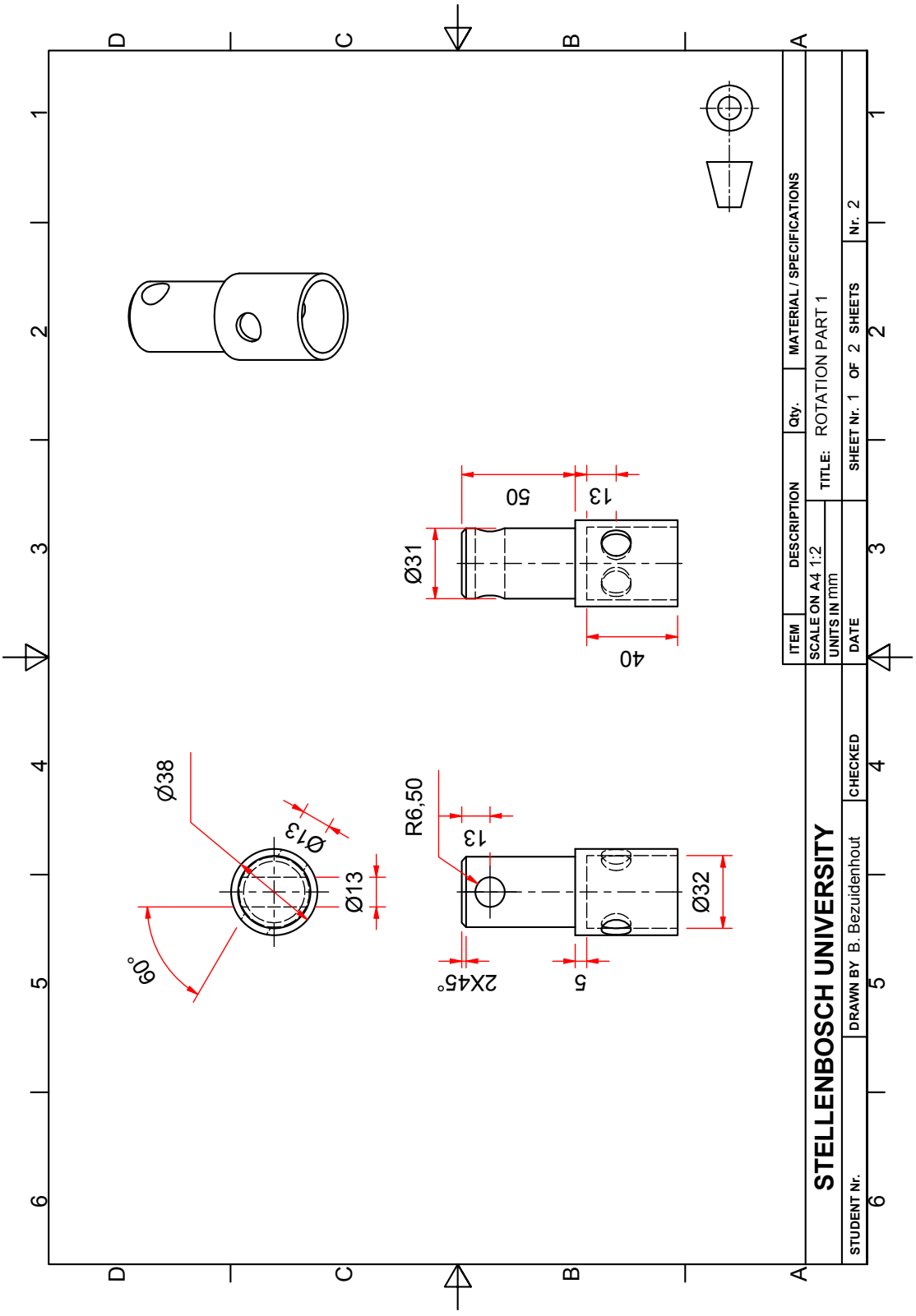

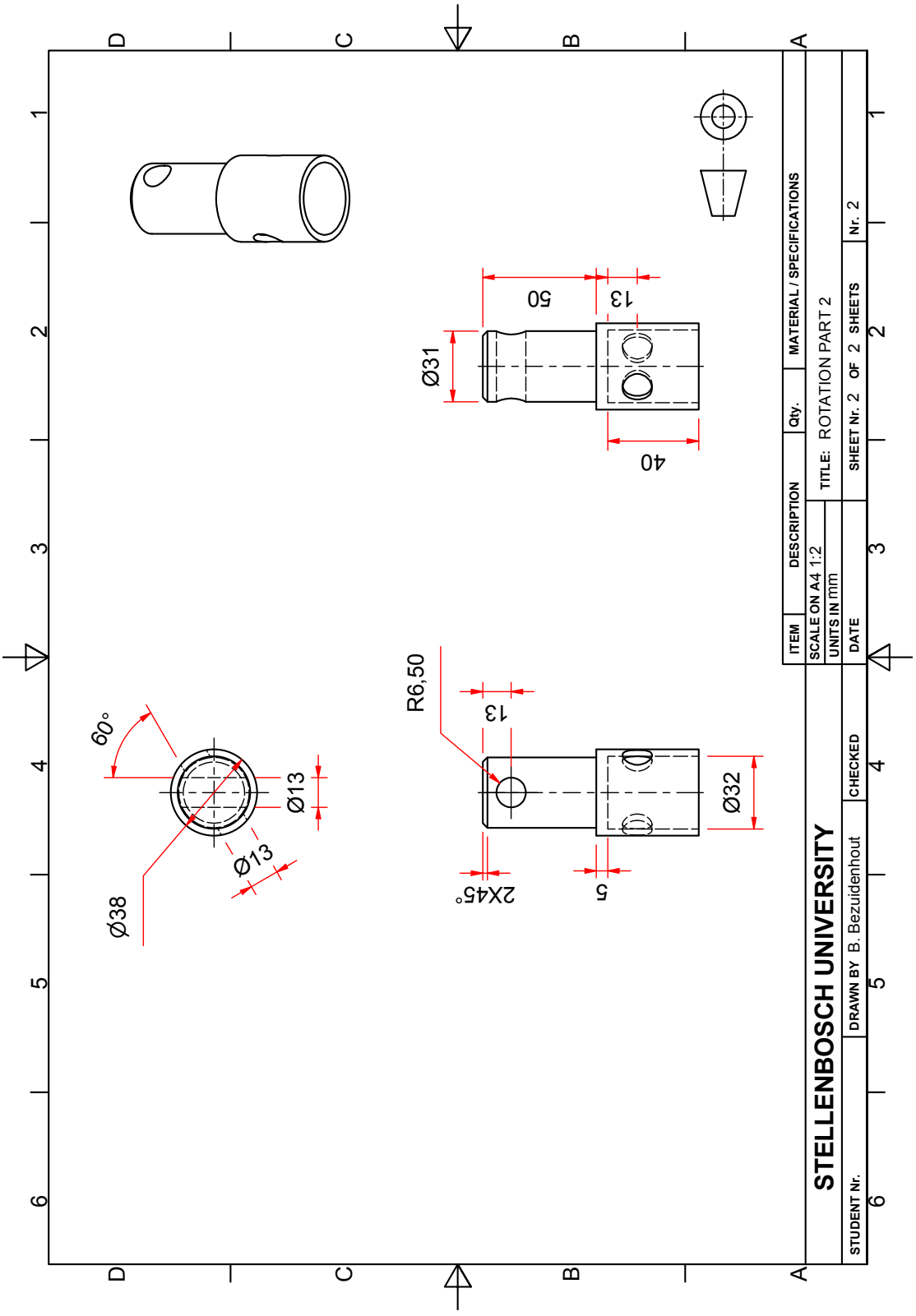

Appendix G

Four-Point Bending Tests Results

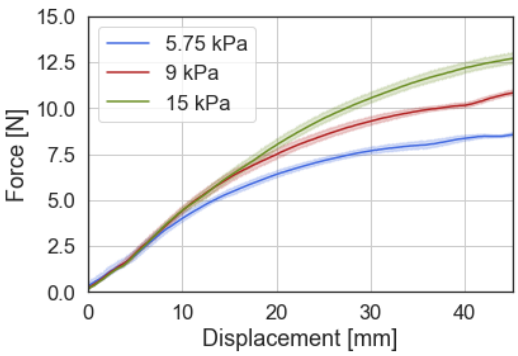

(a) Inflatable bags with 50 mm diameter

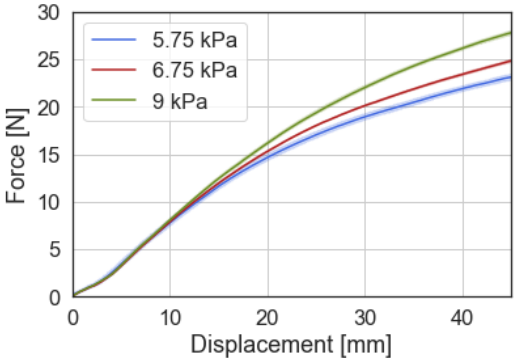

(b) Inflatable bags with 75 mm diameter

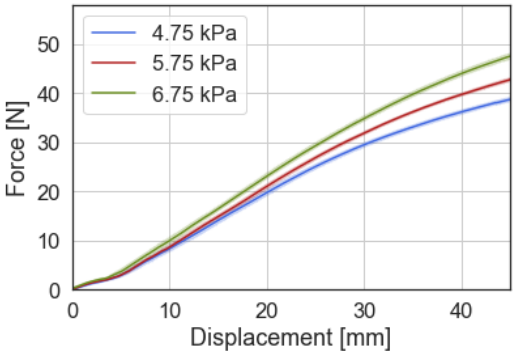

(c) Inflatable bags with 100 mm diameter

Figure G.1: The force vs. displacement curves from the four-point bending tests displaying the influence of pressure at constant bag size where the different pressures for each the same bag size are plotted on the same graphs

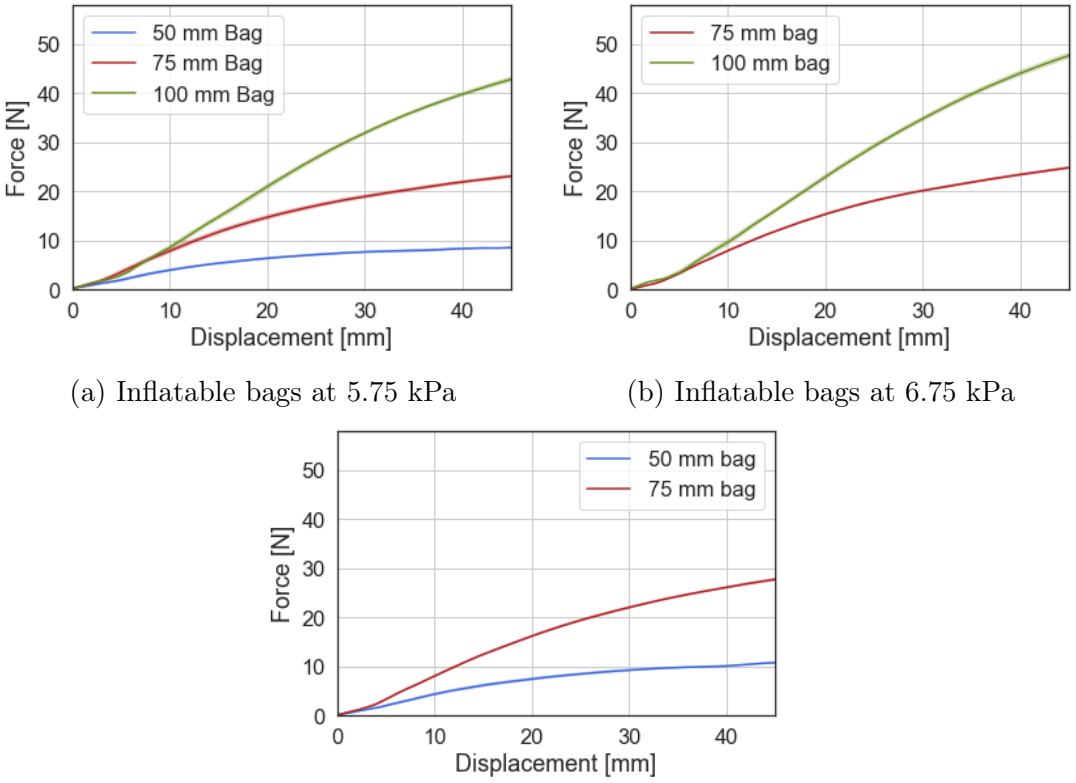

(a) Inflatable bags at 5.75 kPa

(b) Inflatable bags at 6.75 kPa

(c) Inflatable bags at 9.00 kPa

Figure G.2: The force vs. displacement curves from the four-point bending tests displaying the influence of bag size for a constant pressure where different bag sizes at the same pressure are plotted on the same graph

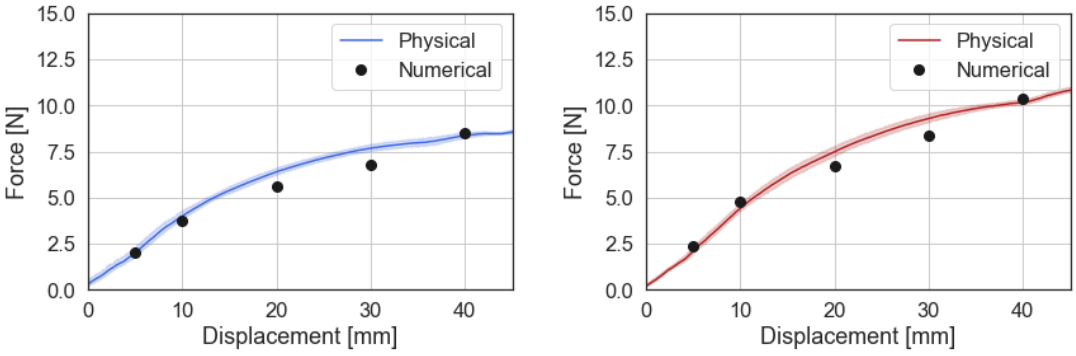

(a) Inflatable bag at 5.75 kPa

(b) Inflatable bag at 9.00 kPa

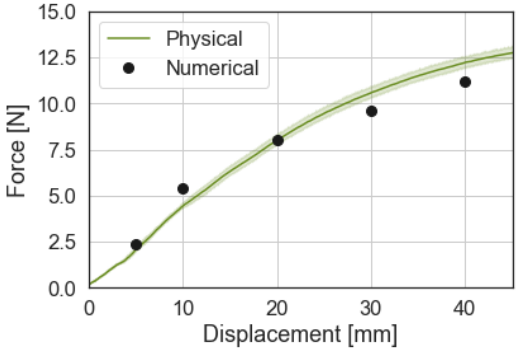

(c) Inflatable bag at 15.00 kPa

Figure G.3: The numerical force vs. displacement values for the 50 mm bags plotted with the data from the physical tests

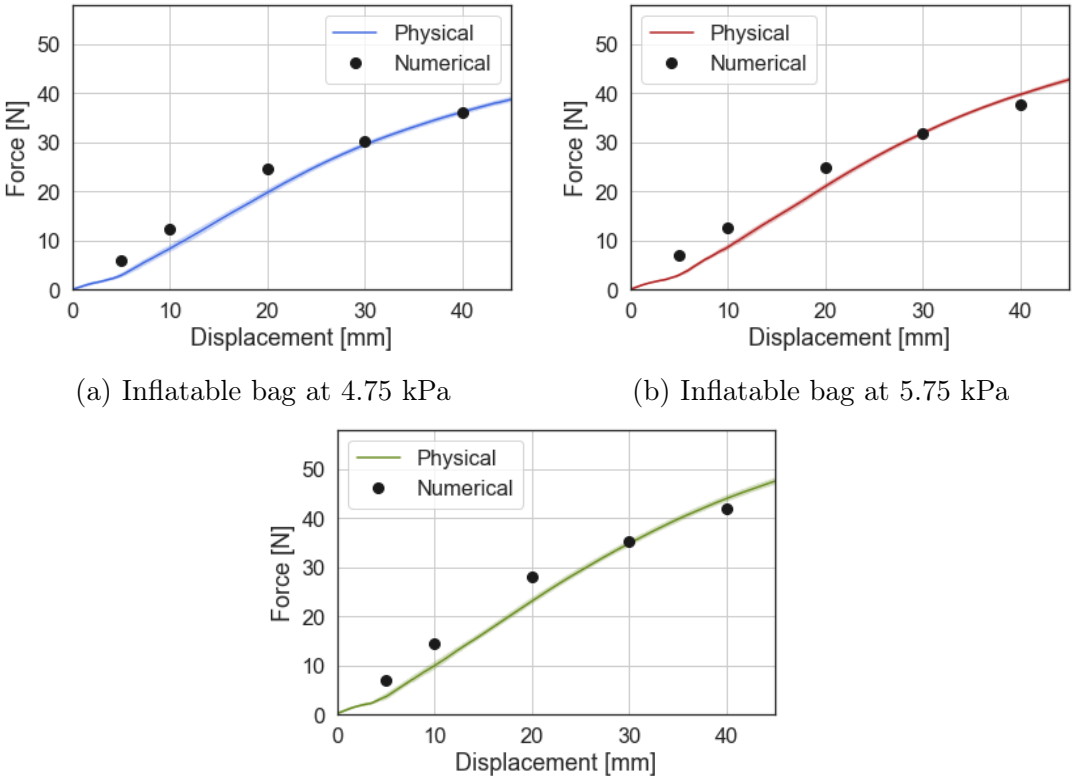

(a) Inflatable bag at 4.75 kPa

(b) Inflatable bag at 5.75 kPa

(c) Inflatable bag at 6.75 kPa

Figure G.4: The numerical force vs. displacement values for the 100 mm bags plotted with the data from the physical tests

List of References

Agarwal, L.P.K. (2007). Hausdorff and Frechet distance. *Geometric Optimization Lecture*, pp. 1–6.

Barsotti, R. and Ligaro, S. (2011). Pressurized Membranes for Structural Use: Interaction Between Local Effects and Global Response. In: *International Conference on Textile Composites and Inflatable Structures*, pp. 67–76. Barcelona.

Bletzinger, K. (2008). A wrinkling model based on material modification for isotropic and orthotropic membranes. *Computer methods in applied mechanics and engineering*, vol. 197, pp. 773–788.

Brown, G., Haggard, R. and Norton, B. (2001). Inflatable structures for deployable wings. In: *AIAA Aerodynamic Decelerator Systems Technology Conference and Seminaar*.

Cadogan, D., Scarborough, S. and Jacob, J.D. (2006). Recent Development and Test of Inflatable Wings. In: *47th AIAA/ASME/ASCE/AHS/ASC Structures, Structural Dynamics, and Materials*. Newport, Rhode Island.

Cadogan, D., Smith, T., Uhelsky, F. and Mackusick, M. (2004). Morphing Inflatable Wing Development for Compact Package Unmanned Aerial Vehicles. *American Institute of Aeronautics and Astronautics*, pp. 1–13.

Cavallaro, P.V., Sadegh, A.M. and Quigley, C.J. (2007). Contributions of Strain Energy and PV-work on the Bending Behavior of Uncoated Plain-woven Fabric Air Beams. *Journal of Engineered Fibers and Fabrics*, vol. 2, no. 1, pp. 16–30.

Cengel, Y.A. and Cimbala, J.M. (2014). *Fluid Mechanics: Fundamentals and Applications*. 3rd edn. Mc Graw Hill Education.

ClevelandMagazine (2015). The Goodyear Model GA-468 Inflatoplane.
Available at: `http://bit.ly/2NCkpu2`

Cleynen, O. (2011). Airfoil Nomenclature.
Available at: `https://commons.wikimedia.org/w/index.php?curid=16100403`

EngineeringToolbox (2001). Youngs Modulus and Poisson's Ratio.
Available at: `https://www.engineeringtoolbox.com`

Haight, A.E.H., Allred, R.E., Harrah, L.A., Mcelroy, P.M., Scarborough, S.E. and Smith, T. (2006). Design and Fabrication of Light Rigidizable Inflatable Wings. In: *47th AIAA/ASME/ASCE/AHS/ASC Structures, Structural Dynamics, and Materials*, pp. 1–9. Newport, Rhode Island.

Hallquist, J.O. (1986). *LS-DYNA Theory Manual*. 2006. ISBN 9254492507.

Hartman, E., Keeler, J. and Kowalski, J. (1990). Layered neural networks with Gaussian hidden units as universal approximations. *Neural Computation*, vol. 2, pp. 210–215.

Hewlett-Packard (2016). HP 3D Structured Light Scanner.
Available at: `https://www8.hp.com/us/en/campaign/3Dscanner/overview.html`

Holland, J.H. (1976). Adaptation in Natural and Artificial Systems. *Society for Industrial and Applied Mathematics*, vol. 18, no. 3.

Jetteur, P. and Bruyneel, M. (2008). Advanced Capabilities for the Simulation of Membrane and Inflatable Space Structures Using SAMCEF. In: *Textile Composites and Inflatable Structures*, vol. 2, pp. 211–231. Netherlands. ISBN 9781402068560.

Johansen, T.A. (2011). *Optimization of a low Reynold's number 2-D inflatable airfoil section*. Ph.D. thesis, Utah State University.

Li, Y. (2017). Dynamics analysis of a designed inflatable wing. In: *International Conference on Information Science and Control Engineering*, pp. 979–983. ISBN 9781538630136.

Lissaman, P. (1983). Low-Reynolds-Number Airfoils. *Annual Rev. of Fluid Mech*, vol. 15, no. 223-239.

Livermore Software Technology Corporation (2019). What are the differences between implicit and explicit?
Available at: `http://bit.ly/2N51BEC`

Louis, F. (2001). The Basics of Neural Networks Demystified. *Contingencies*, vol. 11, no. 12, pp. 56–61.

Ma, L., Xin, K. and Liu, S. (2008). Using Radial Basis Function Neural Networks to Calibrate Water Quality Model. *World Academy of Science, Engineering and Technology International Journal of Environmental and Ecological Engineering*, vol. 2, no. 2, pp. 9–17.

Murray, J., Pahle, J., Thornton, S., Frackowiak, T., Mello, J. and Norton, B. (2002). Ground and flight evaluation of a small-scale inflatable-winged aircraft. In: *40th AIAA Aerospace Sciences Meeting & Exhibition*.

Nitta, K.-h. and Yam, M. (2012). Poisson's Ratio and Mechanical Nonlinearity Under Tensile Deformation in Crystalline Polymers. *Rheology*. ISSN 1744-683X. 0803973233.

Olovsson, L., Simonsson, K. and Unosson, M. (2005). Selective mass scaling for explicit finite element analyses. *International Journal for Numerical Methods in Engineering*, vol. 63, no. 10, pp. 1436–1445. ISSN 00295981.

Park, J. and Sandberg, I. (1993). Approximation and radial basis function networks. *Neural Computation*, vol. 5, pp. 305–316.

Pronzato, L. and Müller, W. (2012). Design of computer experiments : space filling and beyond. *Statistics and Computing*, vol. 3, no. 22, pp. 681–701.

Rodriguez, J. (2011). *Numerical study of dynamic relaxation methods and contribution to the modelling of inflatable lifejackets*. Ph.D. thesis, Université de Bretagne Sud.

Rowe, J. (2007). *Finite Element Modeling of an Inflatable Wing*. Ph.D. thesis, University of Kentucky.

Ryberg, A.-b. (2017). *Metamodel-Based Multidisciplinary Design Optimization of Automotive Structures*. Ph.D. thesis, Linköping University.

Ryberg, B. (2013). *Metamodel Based Design Optimization - A Multidisciplinary Approach for Automotive Structures*. Ph.D. thesis, Linkoping University.

Santhanakrishnan, A. and Jacob, J. (2005). Effect of Regular Surface Perturbations on Flow Over an Airfoil. In: *36th AIAA Fluid Dynamics Conference and Exhibit*.

Santner, T.J., Williams, B.J. and Notz, W.I. (2003). Space-Filling Designs for Computer Experiments. In: *The Design and Analysis of Computer Experiments*, chap. 5. Springer, New York, NY.

Schweizerhof, K. (2005). Efficient Finite Element Modelling and Simulation of Gas and Fluid Supported Membrane and Shell Structures. *Textile Composites and Inflatable Structures*, vol. 3, pp. 153–172.

Simpson, A.D. (2008). *Design and Evaluation of Inflatable Wings for UAVs*. Ph.D. thesis, University of Kentucky.

Snyman, J. (1982). A new and dynamic method for unconstrained minimization. *Appl. Math. Modelling*, vol. 6, pp. 449–462.

Snyman, J. (1983). An improved version of the original leap-frog dynamic method for unconstrained minimization: LFOP1(b). *Applied Mathematical Modelling*, vol. 7, no. 3, pp. 216–218. ISSN 0307-904X.

Snyman, J. (2000). The LFOPC Leap-Frog Algorithm for Constrained Optimization. *Computers & Mathematics with Applications*, vol. 40, pp. 1085–1096.

Stander, N., Roux, W., Goel, T., Eggleston, T. and Craig, K. (2010). *LS-OPT User's Manual v4.1*. December. Livermore Software Technology Corporation. ISBN 9254492507.

Terrence, L.F. (1999). *Feedforward Neural Networks Methodolgy*. Springer Science & Business Media. ISBN 9780387987453.

Thomas, J.-C., Wielgosz, C. and Van, A.L. (2016). Mechanics of inflatable fabric beams. In: *4th International Conference on Thin Walled Structures*.

Veldman, S.L. (2005). *Design and analysis methodologies for inflated beams*. Ph.D. thesis, Delft University.

Venter, G. (2010). Review of Optimization Techniques. *Encyclopedia of Aerospace Engineering*, pp. 1–12.

Venter, M.P. (2011). *Development and Validation of a Numerical Model for an Infatable Paper Dunnage Bag Using Finite Element Methods*. Ph.D. thesis, Stellenbosch Univeristy.

Wang, G.G. and Shan, S. (2006). Review of Metamodeling Techniques in Support of Engineering Design Optimization. *ASME Transactions, Journal of Mechanical design*, pp. 1–42.

Wang, H. and Li, Y. (2017). The Aerodynamic Performance of an Inflatable Wing in Aircraft. In: *7th International Conference on Education, Management, Information and Mechanical Engineering*, vol. 76, pp. 12–17.

Zhu, Z.H., Seth, R.K. and Quine, B.M. (2008). Experimental Investigation of Inflatable Cylindrical Cantilevered Beams. *JP Journal of Solids and Structures*, vol. 2, no. 2, pp. 95–110.
Available at: `http://www.pphmj.com`